Doctoral theses at NTNU, 2022:260

Are Bergin

Ceramic Foam Filters (CFFs) for Aluminium Melt Filtration - Stability, Compression, and Performance

Doctoral thesis

NTNU
Norwegian University of Science and Technology
Thesis for the Degree of
Philosophiae Doctor
Faculty of Natural Sciences
Department of Materials Science and Engineering

NTNU
Norwegian University of
Science and Technology

Are Bergin

Ceramic Foam Filters (CFFs) for Aluminium Melt Filtration - Stability, Compression, and Performance

Thesis for the Degree of Philosophiae Doctor

Trondheim, September 2022

Norwegian University of Science and Technology
Faculty of Natural Sciences
Department of Materials Science and Engineering

NTNU
Norwegian University of
Science and Technology

NTNU
Norwegian University of Science and Technology

Thesis for the Degree of Philosophiae Doctor

Faculty of Natural Sciences
Department of Materials Science and Engineering

ISBN 978-82-326-5934-0 (printed ver.)
ISBN 978-82-326-6022-3 (electronic ver.)
ISSN 1503-8181 (printed ver.)
ISSN 2703-8084 (online ver.)

Doctoral theses at NTNU, 2022:260

Printed by NTNU Grafisk senter

Preface

The present work, initiated in January 2018, has been a collaboration between the Norwegian University of Science and Technology, Department of Materials Science and Engineering (NTNU-IMA) (Trondheim, Norway), Hydro Aluminium AS (Norsk Hydro ASA) (Sunndalsøra, Norway), and the Technische Universität Bergakademie Freiberg, Professorship of Ceramics, Refractories and metal-ceramic Composites (IKFVW) (Freiberg, Germany), with Hydro as the project owner. The project was funded by Norsk Hydro ASA with support from the Industrial PhD scheme of The Research Council of Norway (RCN) (Project number: 284090), having the author work 25 % of his time with tasks related to his employment at Norsk Hydro ASA (Research and Technology Development, Sunndalsøra, Norway) and 75 % on the present project at NTNU.

The majority of the experimental part of the work has been performed at the lab facilities at NTNU-IMA, with additional experiments carried out at the R&D facilities of SELEE (Hendersonville, NC, USA) and at Norsk Hydro ASA's Reference Centre (Sunndalsøra, Norway). The work performed has resulted in 8 publications, 2 conference presentations, and 2 posters (see list below). One of the posters was the winner of the 2019 Technical Division Student Poster Competition at the Light Metal Division.

Due to the COVID-19 pandemic, some part of the work was put on hold in 2020 and 2021, resulting in two of the publications being delayed. Both publications are, however, now submitted for publication and are awaiting review at the time of the thesis submission.

An additional publication is added to the list below as the author participated as a Norsk Hydro ASA employee and the publication topic is relevant to the present work.

Overall thesis structure

The thesis is structured around the first five publications listed below, which also are attached to the thesis for evaluation by the opponents. An introduction to the relevant background and theory is given in the thesis, together with the applied experimental and analytical procedures, as well as a summary of each of the relevant publications. The thesis ends with an overall conclusion and future work.

Supplements to the thesis

1. **A. Bergin**, C. Voigt, R. Fritzsch, S. Akhtar, L. Arnberg, C.G. Aneziris and R.E. Aune, *Experimental Study on the Chemical Stability of Phosphate Bonded Al_2O_3-based Ceramic Foam Filters (CFFs)*, Metallurgical and Materials Transactions B, 52, 2021, pp. 2008 – 2025.
2. **A. Bergin**, R. Fritzsch, S. Akhtar, L. Arnberg and R.E. Aune, *Silicon Depletion from Ceramic Foam Filters (CFFs) during Aluminium Melt Filtration in a Pilot-Scale Setup*, Brief communication submitted for publication to the Journal of Metallurgical and Materials Transactions B, July 2022.
3. **A. Bergin**, R. Fritzsch, S. Akhtar, L. Arnberg, and R.E. Aune, *Compression Testing of Ceramic Foam Filters (CFFs) Submerged in Aluminium at Operating Temperature*, Light Metals, 2021, pp. 794 – 802.

4. **A. Bergin**, C. Voigt, R. Fritzsch, S. Akhtar, L. Arnberg, C.G. Aneziris and R.E. Aune, *Investigation of Mechanical and Thermo-Mechanical Strength of Ceramic Foam Filters (CFFs)*, Manuscript submitted for publication to the Journal of Ceramics International, August 2022).
5. **A. Bergin**, C. Voigt, R. Fritzsch, S. Akhtar, L. Arnberg, C.G. Aneziris and R.E. Aune, *Performance of Regular and Modified Ceramic Foam Filters (CFFs) during Aluminium Melt Filtration in a Pilot-Scale Setup*, Light Metals, 2022, pp. 640 – 648.

Connected publications

6. Voigt, J. Hubálková, **A. Bergin**, R. Fritzsch, R.E. Aune, and C.G. Aneziris, *Overview of the Possibilities and Limitations of the Characterization of Ceramic Foam Filters for Metal Melt Filtration*, Light Metals, 2021, pp. 785 – 793.
7. R. Fritzsch, T.L. Schanche, H. Zedel, **A. Bergin**, S. Akhtar, L. Arnberg, and R.E. Aune, *Aluminum Melt Cleanliness Analysis based on Direct Comparison of Computationally Segmented PoDFA Samples and LiMCA Results*, Light Metals, 2022, pp. 633 – 639.
8. Voigt, J. Hubálková, **A. Bergin**, R. Fritzsch, S. Akhtar, R.E. Aune, and C.G. Aneziris, *Short- and Long-Term Aluminum Filtration Trials with Carbon-Bonded Alumina Filters*, Light Metals, 2022, pp. 626 – 632.

Presentations at conferences

9. **A. Bergin**, R. Fritzsch, S. Akhtar, L. Arnberg, and R.E. Aune, *Compression Testing of CFFs in Aluminium*, TMS 2021, Virtual conference, 15 – 18th of March 2021.
10. **A. Bergin**, C. Voigt, R. Fritzsch, S. Akhtar, L. Arnberg, C.G. Aneziris and R.E. Aune, Performance of Regular and Modified Ceramic Foam Filters (CFFs) during Aluminium Melt Filtration in a Pilot-Scale Setup", TMS 2022, Anaheim, USA, 27th of February – 3rd of March 2022.

Posters at conferences

11. **A. Bergin**, R. E. Aune, L. Arnberg, S. Akhtar, U. H. Tundal, and G. Tranell, *Mechanistic Study of the Ceramic Foam Filter (CFF) Technology on the Metal Cleanliness of Aluminium and Its Alloys*, INCAL 2019, Bhubaneswar, India, 31st of January – 3rd of February 2019.
12. **A. Bergin**, R. E. Aune, L. Arnberg, U. H. Tundal, and S. Akhtar, *Conventional Ceramic Foam Filters (CFFs) – Priming and Chemical Stability*, TMS 2019, San Antonio, USA, 10 – 14th of March 2019. **Winner of 2019 Technical Division Student Poster Competition – Light Metal Division.**

Other relevant publications

- M. Syvertsen, I. Johansen, A. Kvithyld, S. Bao, U. Eriksen, B.E. Gihleengen, S. Akhtar, **A. Bergin**, A. Johansson, *Evaluation of CFF and BPF in Pilot Scale Filtration Tests*, Light Metals, 2020, pp. 963 – 971.

Acknowledgements

The number of contributions and contributors to a project like this are many, anything from very small contributions such as discussions and tips to more extensive forming of the project. Thus, mentioning everyone is an impossible task, but credit must be given.

Firstly, I would like to thank my main supervisor Ragnhild E. Aune. Her guidance has been vital for the project, she has introduced me to and taught me numerous things, and her devotion where office hours only were guiding have been greatly appreciated. I would also like to extend my gratitude to co-supervisors Lars Arnberg and Shahid Akhtar for their invaluable input and discussions. I will miss the weekly meetings between the four of us.

Great appreciation is sent to Robert K. Fritzsch for being of excellent help during the project. His experimental knowledge, creativeness, positive attitude, and cheerful mood have all had a great positive impact on the work.

I have further appreciated all the support given by Hydro Aluminium AS and the R&D Centre at Sunndalsøra, personified by the head of Commercial Technology, Stig Tjøtta and the current head of department, Stig Brusethaug. Thank you for giving me the chance to pursue a PhD and deep dive into an exciting but narrow topic. The same goes for my different team leaders during the project period, *i.e.* Ulf H. Tundal, Steinar Benum and Snorre Rist, who all organised company tasks in an excellent way, not obstructing the PhD work. I am also grateful for all the good discussions and help received from researchers and technical personnel at the R&D Centre and the rest of the company.

I would further like to thank Claudia Voigt and Christos G. Aneziris at TU Bergakademie Freiberg for producing input material for many of the trials and for good discussions and feedback during the writing of articles.

I am also very grateful for everyone that has crossed my path through my roaming at NTNU, SINTEF, and connected arrangements, both social and work-related. None are mentioned, none are forgotten. It has been a pleasure, and I hope we meet again.

Last but not least, of course, my family, for always being very supportive and in some cases a vent of any frustration.

Are Bergin

Are Bergin
Sunndalsøra, July 2022

Abstract

During aluminium production, the molten aluminium will necessarily include a certain amount of impurities, including non-metallic inclusions, *i.e.,* solid objects immersed in the melt. These inclusions are known to be detrimental both for further processing, such as rolling and extrusion, as well as for the final product's mechanical properties. Therefore, reducing them to a minimum is essential. A commonly applied method for inclusion removal is filtration, *e.g.*, with the use of ceramic foam filters (CFFs), where improvements in filtration efficiency are desired.

The main focus of the present project has been to test the suitability and performance of new and innovative CFFs, *i.e.,* CFFs not commercially available, with the overall aim of improving filtration efficiency. The project was started by testing the chemical and thermal stability of the filters when they were subjected to conditions comparable to those in a casthouse. Thereafter the filtration performance of promising filter candidates was tested in a pilot-scale filtration campaign replicating casthouse conditions.

The chemical stability of filters was analysed by performing immersion trials, where the filters were immersed in melts of pure aluminium (~ 99.5 wt.-% Al) and an aluminium-magnesium alloy (~ 2.2 wt.-% Mg) at 730 °C, whereby the melt compositions were analysed by spectroscopy and the filters examined by imaging and x-ray techniques. In addition, any formation of phosphine gas (PH_3) was measured using Dräger-Tubes®. Filters produced with a phosphate binder were observed to react with magnesium in the melt, with increasing severity for increasing magnesium concentrations. Reactions between the melt and the filter foam were even observed with magnesium in trace element concentrations (0.00035 wt.-% Mg). This observed filter degradation was accompanied by diffusion between the filter and the melt, where magnesium was observed to diffuse into the filter and phosphorus into the melt. Upon filter cooling in air after testing, the degraded filter reacted with the humidity in the air, emitting phosphine gas at amounts exceeding recommended exposure limits. The new and innovative filters, produced without a phosphate binder, showed no indications of being reactive in molten aluminium with the present immersion tests.

The thermal stability of the filters was investigated through compression strength testing, where compression strength at room temperature served as a reference. Compression was further performed at elevated temperatures by heating filters at 800 °C and performing compression tests in air at a filter temperature of ~ 730 °C. A method was designed to perform compression of filter samples submerged in molten aluminium, where the filters were tested in melts with the same compositions as in the chemical stability tests. Through analysis of load-displacement curves it was observed that the strengths, with a few exceptions, decreased for testing at elevated temperature compared to room temperature testing. The testing of filter samples submerged in molten aluminium led to a further decrease in the compression strength. There was a significant difference in compression strength between the commercial filters and the new and innovative sintered alumina filter, which showed a higher strength. No difference in strength was seen between the two melt compositions at the present filter submersion time of 5 minutes.

The filtration performance of a series of CFFs was also tested in a pilot-scale loop filtration setup, using 8 tons of a 6082 aluminium alloy (with extra additions of magnesium) per trial. Some trials were run with additions of grain refiner to investigate its effect on filtration efficiency, while others were not. The filtration performance was evaluated by continuously measuring the melt quality before and after the filter with two Liquid Metal Cleanliness Analyzers (LiMCAs) and the pressure drop over the filter using lasers. Furthermore, three PoDFA-sampling sequences were performed per trial, and after each trial, the spent filters were analysed by light optical microscopy (LOM) and scanning electron microscopy (SEM). It was concluded that the filtration performance of the different filters was similar to each other, with filtration efficiencies in the upper range of what was expected. Additionally, in relation to the previously performed chemical stability immersion tests, a commercial filter of sintered alumina and silica showed indications of silicon depletion upon spent filter analysis.

Keywords: Aluminium, Ceramic Foam Filters (CFFs), Filtration Performance, Chemical Stability, Thermal Stability, Compression Strength.

List of Abbreviations and Symbols

ABBREVIATION	DESCRIPTION
AMCA	Automated Metal Cleanliness Analyzer
BN	Boron Nitride
BPF	Bonded Particle Filter
CFF	Ceramic Foam Filter
DBF	Deep Bed Filter
DFF	Drain Free Filtration
EBSD	Electron Backscatter Diffraction
EDS	Energy Dispersive x-ray Spectrometry
EPMA	Electron Probe Microanalysis
FIB	Focused Ion Beam
LiMCA	Liquid Metal Cleanliness Analyzer
LOM	Light Optical Microscopy
OES	Optical Emission Spectroscopy
PE	Polyethylene
PoDFA	Porous Disc Filtration Apparatus
PPI	Pores Per Inch
PUR	Polyurethane
RMF	Rigid Metal Filter
SEM	Scanning Electron Microscopy
SLPM	Standard Litres Per Minute
STEL	Short-Term Exposure Limit
TEM	Transmission Electron Microscopy
TWA	Time-Weighted Average

SYMBOL	DESCRIPTION
A	Loaded area
A_f	Filter surface area
b	Base of strut cavity
C	Constant
D	Outside strut diameter
F	Metal flow rate

F_{max}	Maximum load
g	Gravitational acceleration
h	Height of strut cavity
h_p	Priming height
K_0	Kinetic parameter
L	Filter thickness or length of filter strut
l	Length of filter struts/walls
P	Pressure or applied load at fracture
t	Thickness of filter struts/walls
U_m	Superficial velocity
V_f	Interstitial velocity
Z	Filter depth
ε	Filter void fraction
θ	Wetting angle
λ	Kinetic parameter divided by superficial velocity
ρ	Density
ρ_{foam}	Density of foam
ρ_{rel}	Relative density
ρ_{solid}	Density of solid
σ_{fc}	Compression strength of foam
σ_{sc}	Compression strength of bulk material
σ_{sc}	Strut fracture strength
Y_{LS}	Surface energy solid/liquid
φ	Functional pore window size

Contents

1. Introduction

Aluminium is a relatively new metal [1] compared to other metals such as copper, iron and steel, which have their first mentions in pre-historic times [2,3]. The first reports of aluminium date back to the Roman Emperor Tiberius, who was presented with a cup bright as silver but too light to be silver, thus likely to be aluminium or aluminium-based material [1]. However, the industrial extraction and production of aluminium are considered to have started as late as 1888, using the Hall-Héroult process [4]. With this process, aluminium is produced by an energy-intensive electrolytic reduction of alumina (Al_2O_3), where alumina is dissociated into aluminium and oxygen. The latter reacts with carbon anodes to form carbon dioxide, which exits the process as gas. Once aluminium has been produced and used for a specific application, it can be recycled and reused repeatedly. With its low melting point (660 °C for pure aluminium [5]) and consistent properties before and after remelting, aluminium is highly beneficial to recycle, and recycling has therefore gained more and more traction in recent decades. The overall annual aluminium production (excluding Russia and China) was 17.1 million tonnes in 1980, of which 4.4 million tonnes were recycled, while in 1995 the aluminium production and recycling had increased to 23.9 and 6.5 million tonnes, respectively [4]. The total primary production of aluminium, *i.e.,* without recycled aluminium, was in 2020 reported being 23.8 million tonnes excluding Russia and China, and 65.3 million tonnes for the whole world [6], where the ratio of recycled aluminium to primary production is estimated to increase in the coming years [7].

The produced aluminium, independent of having a primary and/or secondary (recycled) origin, will contain a certain amount of impurities. Both the amount and types of impurities can vary for secondary aluminium as compared to aluminium from primary sources, where the metal from different secondary sources has been reported to vary in the range of high to a low degree of cleanliness [8]. The main impurities in aluminium are usually divided into dissolved elements, dissolved gas (H_2) and non-metallic inclusions [4], which all have different negative impacts on the final product. Non-metallic inclusions are micro-sized solid particles and oxide films suspended in the molten aluminium, which do not dissolve in the melt. Common inclusions typically have compositions Al_2O_3, SiO_2, MgO, $MgAl_2O_4$ and Al_4C_3 [9,10].

There are many detrimental effects of inclusions, and even very low inclusion amounts and sizes can be the source of defects such as pinholes in rolled aluminium foils [9] and pores due to entrapped oxide films [11]. Inclusions can be removed from the melt by various methods, but perhaps the most common approach is filtration, which has been designed explicitly for inclusion removal. Different filtration methods commonly applied are deep bed filters (DBFs), rigid metal filters (RMFs) and ceramic foam filters (CFFs) [12], where each has its strengths and weaknesses. For instance, a high removal efficiency but large space requirements and low flexibility in the case of DBFs [13].

Ceramic foam filters (CFFs) have been reported to be the most used filter type in the aluminium industry [13] and are often preferred due to their relatively low cost and high operational flexibility. They are made by a ceramic slurry applied on a foam of polyurethane (PUR), coating all the foam surfaces with a thin and uniform layer. The coated PUR foam is then heated at high temperatures causing the PUR to burn off, leaving a ceramic structure that is either sintered or fused together. The remaining ceramic structure, *i.e.,* the CFF, is highly porous both on the micro- and macro-scale, where the molten aluminium flows through a network of the larger pores. The density of these large pores determines the grade of the filters in pores per inch (PPI), where a higher number indicates smaller but more numerous pores. The incoming inclusions suspended in the molten aluminium may then be captured by the filter, either at the filter inlet, which eventually will lead to cake filtration mode, or within these large pores through the whole thickness of the filter, defined as deep bed filtration mode [9,10,14].

The topic of filtration performance of CFFs has been extensively researched, and the filtration efficiency has been described to be affected by numerous parameters. It was early proposed by Apelian *et al.* [15], and supported by many more recent authors, that the filtration efficiency is dependent on the melt velocity in particular, but also on other properties such as the filter thickness, inclusion sizes *etc.* It has further been reported that an increase in filtration efficiency would be the effect of an increase in PPI [16–19]. However, by looking at data from several experimental studies with different PPI filters, it can be seen that the filtration efficiency varies within a range per PPI, where the range decreases with increasing PPI. Thus, a more accurate description of the relation between PPI and filtration efficiency is that the filter reliability increases with increasing PPI [20]. Even though the mentioned parameters are known to affect filtration efficiency, improving the efficiency by changing the parameters is not necessarily straightforward. In a casthouse or a foundry the conditions are often set, meaning, *e.g.*, that it is not possible to change the flow rate or control the size of incoming inclusions.

Furthermore, the filter thickness may not be easily varied, and increasing PPI could be difficult due to problems with metal penetration through the filters, possibly with too low flow rates as a result. Thus, improvements to the filtration performance should ideally find alternative routes, *e.g.*, by altering the CFF surface. Other reported limitations for the CFFs are that their chemical stability in aluminium is insufficient, *i.e.,* they react with the molten aluminium or elements within the melt [21]. In addition, they are highly brittle materials that are known to fracture or fail from time to time, while at the same time, there is nearly no data available on the strength of the filters in operating conditions.

There are, however, recent studies on new and innovative CFFs. These new filters consist of sintered ceramics with different surface chemistries (other than the commonly used alumina) [22–24], as well as alumina filters with different surface roughness [24,25]. These studies have mainly investigated filtration performance, to a large degree showing promising results.

1.1. Project scope

The present project has assessed the limitations mentioned above for the CFF technology while simultaneously performing a possible stepwise qualification program for new and innovative CFFs. An overview of the complete project scope is presented in Figure 1.1. From the figure, it can be seen that the inputs are various CFFs, both commercial and new filters which are presently not commercially available, as well as molten aluminium of different compositions where magnesium is the main element varying. The work is divided into three main experimental parts, *i.e.,* chemical stability tests, thermal stability tests, and pilot-scale filtration trials. The experimental procedures and results of the chemical stability tests (Part I) are presented in Chapter 3.3 and Chapter 4.1, respectively, where the filters were tested in two different immersion experimental setups. The chemical stability of the filters was assessed by varying the magnesium concentration of the melt and the duration of melt exposure, with subsequent filter investigation and melt analysis, as well as measurements of phosphine (PH_3) gas formation. The experimental procedures and results of the thermal stability tests (Part II) are presented in Chapter 3.4 and Chapter 4.2, respectively. The thermal stability of the filters was assessed through compression testing, where compression at room temperature served as a reference. Thermal stability was then defined as the effect of temperature and submersion in molten aluminium on the compression strength. The thermal stability was assessed both with different heating times in air and with exposure to melts of different compositions.

The results from both the chemical- and thermal stability tests were reviewed, in addition to a review of previously reported results. The most promising filter candidates were tested together with reference filters in the subsequent pilot-scale filtration trials (Part III). The accompanying experimental procedures and results are presented in Chapter 3.5 and Chapter 4.3, respectively, where continuous filtration trials were performed in a pilot-scale experimental setup using 8 tons of molten aluminium. Grain refiner additions were performed on some of the filtration trials, and for all trials the melt cleanliness was analysed using liquid metal cleanliness analysers (LiMCA II) [26] and porous disc filtration apparatuses (PoDFA) [27]. The spent filters were analysed by using different microscopy techniques.

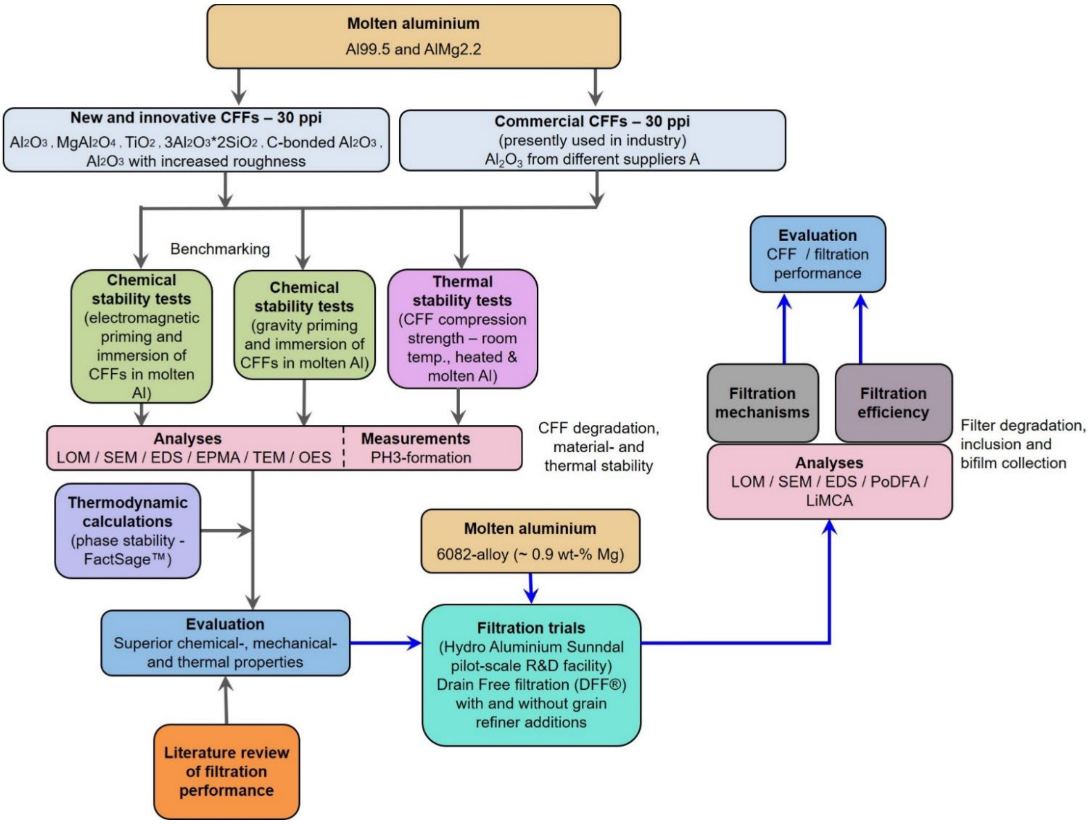

Figure 1.1: Flow sheet showing the present project scope and the chronological order of the different activities.

2. Background

2.1. Aluminium and aluminium production

Aluminium (Al) is the third most abundant element and the most abundant metal in the earth's crust at 8.3 wt.-%, where only the elements oxygen (O) and silicon (Si) occur at a higher frequency, while iron (Fe) is the metal following aluminium as the second most frequent metal in the earth crust [28]. Compared to other metals, aluminium is relatively new and a frequently used metal due to its many favourable properties, such as lightweight (1/3 the density of steel), corrosion resistance (especially to water and weather where, *e.g.*, steel and zinc (Zn) easily corrode), inert towards food, good formability, high conductivity, high strength (with the addition of alloying elements), high elasticity and high reflectivity [4].

The history of industrial aluminium production started in 1888 at the same time in Europe and in the United States, with Héroult's process (in Switzerland) and Hall's process (in Pennsylvania) [4]. Fused together, these two processes are now known as the Hall-Héroult process, which today is used all over the globe for the primary production of aluminium. As aluminium is not present in its metallic form in nature, but as hydrated oxides or silicates, there is a chain of processes applied before the actual aluminium production. The preferred raw material is mined rocks referred to as bauxite, often containing 35 – 55 wt.-% of alumina (Al_2O_3), where the Al_2O_3 is retrieved into a fine white powder at an alumina plant (most commonly through the Bayer process) [4]. This pure Al_2O_3 powder is one of the input materials in the Hall-Héroult process, where aluminium is produced through electrolysis. The other components in the electrolysis cell are the molten cryolite (Na_3AlF_6) acting as an electrolyte, additions of different salts (such as AlF_3 and CaF_2), a carbon cathode floor, carbon anode blocks produced from coke, and massive amounts of electrical energy. The production of 1 kg of aluminium typically consumes 1.95 kg of Al_2O_3 and 0.5 kg of anode coke, while the electrical consumption has decreased through technological developments in the last 35 years from around 21 to 13 kWh/kg aluminium [4]. Recent improvements have reduced the electrical consumption even further down to 12.3 kWh/kg aluminium [29].

Secondary aluminium production describes all forms of aluminium recycling, whether the aluminium raw material originates from used aluminium products (post-consumed scrap), from the production or manufacturing of products (process scrap), or from the treatment of industry by-products (*e.g.,* treatment of dross). Each of these raw material sources has different challenges. For post-consumer scrap it is often necessary with pre-treatment, as the used products could be lacquered or glued together with a polymer, which could degrade metal quality [30]. In addition, scrap sourcing and alloy identification are essential to achieve good and consistent scrap quality, leading to a more straightforward and better recycling process with cast metal of higher quality [31]. A pre-treatment is also necessary for biproducts, where an example is the melting of dross in the presence of salts to recover aluminium. A common challenge for all raw material sources is the potential of different types and increased amounts of impurities and inclusions, compared to aluminium from primary sources, where the cleanliness level of the cold metal scrap can be everything from quite clean to very dirty [8]. However, despite these challenges, recycling of aluminium is highly beneficial. Aluminium can be infinitely recycled without loss of material properties, where the only loss is minor amounts of mass due to the highly oxidising nature of aluminium ($Al(l) \rightarrow Al_2O_3(s)$). This is why about 75 %

of all the aluminium ever produced (since the start in 1888) is still in use today, where some have been through numerous lifecycle loops, *e.g.,* beverage cans [32].

Furthermore, the energy needed to recycle aluminium is only 5 % of the energy needed for primary production, and thus a significant decrease in corresponding emissions, including greenhouse gases, can be avoided [32]. Due to this, the increase in recycled aluminium from post-consumed scrap has increased by 69 % from 2009 to 2019 [33]. The International Aluminium Institute (IAI) estimates that an 80 % global increase in aluminium demand by 2050 can be covered by a 50/50 balance of primary and secondary aluminium production, see Figure 2.1, which is based on collection rates from 2019 [7].

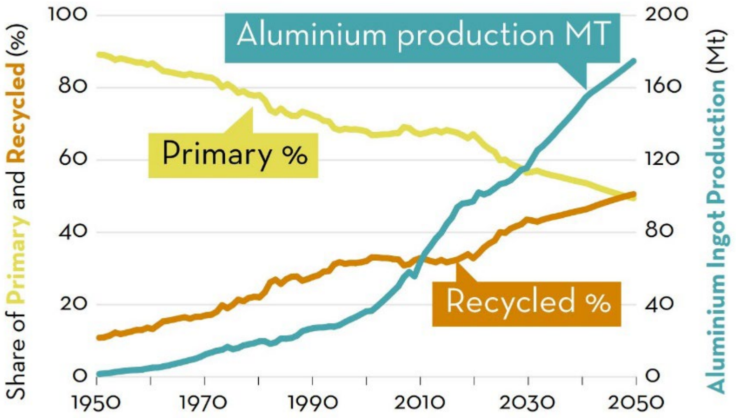

Figure 2.1: Estimate of the global aluminium production with the share of primary produced aluminium and recycled aluminium as raw material sources, up to 2050 [7]. Figure retrieved from the International Aluminium Institute (IAI).

2.2. Casthouse operations

Regardless of whether the aluminium is sourced from primary- and/or secondary production, it will go through a casthouse and be subjected to more or less the same casthouse operations before ending up as a semi-product. The following subchapter will present the activities in a casthouse.

2.2.1. Casting

Casting is one of the last process steps in a casthouse, where the molten aluminium melt solidifies into an aluminium billet, slab, or ingot with a face-centred cubic structure [4]. The solidification starts with nucleation and growth to form dendrites which touch each other and finally form grains [4]. In a pure and clean aluminium melt, the dendrite growth usually occurs from the cooling interfaces and inwards, the opposite direction of the heat sink, leading to relatively large columnar grains. Thus, a grain refiner is normally added to obtain evenly distributed nuclei and grain growth in the whole melt, so-called equiaxed growth, leading to small grains of similar size. If other elements are present in the melt, such as alloying or trace elements, the solidified crystal structure is either homogenous or heterogeneous. The former is the case when elements are present in amounts below their limit of solubility. Reversely, the heterogeneous atomic structure occurs when the specific elements are present in an amount exceeding the solubility limit, normally leading to the formation of intermetallic phases consisting of aluminium and one or more other elements [4].

After casting, the solid aluminium is run through other processes depending on the final application. Billets are often homogenised before being manufactured in an extrusion press, while slabs are often run through a rolling mill. In both cases, the casting process, the grain size and grain size distribution, as well as the intermetallic phases are crucial for the final product. In the case of ingots intended for foundry applications, however, these properties are of lesser importance due to the ingots normally being remelted before casting. One thing that is of high significance for all applications, independent of the casting process, is the presence of impurities that are detrimental to the final product.

2.2.2. Impurities detrimental to the final product

The detrimental impurities that are present in aluminium are usually distinguished into three categories, *i.e.,* dissolved elements (mainly the alkali metal sodium (Na)), dissolved gas (hydrogen (H_2) as it is the only gas soluble in molten aluminium), and non-metallic inclusions [4].

Dissolved elements

The dissolved elements category is wide as it covers all the elements that may dissolve in aluminium, but depending on the application, not all elements are necessary regarded as impurities. Examples of this are the elements manganese (Mn), iron (Fe) and titanium (Ti), which are harmful to electrical applications due to a substantial increase in the resistivity when in solid solution [9]. Still, these elements are added as alloying elements for many other applications. Thus, the main dissolved element impurities considered are often alkali and alkaline earth metals such as sodium (Na), calcium (Ca), and potentially lithium (Li). In aluminium produced from a Hall-Héroult electrolysis cell, the amount of sodium is usually in the range of 20 – 100 ppm [4,9], and its presence may lead to the formation of edge cracks during the rolling process [9,34], as well as hot cracking [34]. Calcium can usually be found in amounts of 3 – 10 ppm [9], and it reduces the electrical conductivity, strength, and fluidity of aluminium depending on the amounts present, as well as increases the porosity and may lead to edge cracking during rolling (similar to sodium) [35]. If raw materials such as cryolite contain lithium, the aluminium can have concentrations of lithium in the range of 2 – 10 ppm [4], which reduces the fluidity of the melt [35], increases the corrosion rate, and causes hot cracking [34]. With more considerable additions of lithium, as in the case of an Al-Li alloy, the metal will have decreased ductility, formability, fracture toughness, and anisotropic mechanical properties [36].

Dissolved gas

Hydrogen is absorbed by aluminium through a reaction between water and the liquid aluminium, see Equation (2.1), where the water most commonly is present as moisture in the atmosphere, but can possibly also originate from remelting of oily, wet, and/or corroded scrap [4].

$$2\mathrm{Al(l)} + 3\mathrm{H_2O(g)} \rightarrow \mathrm{Al_2O_3(s)} + \underline{6\mathrm{H}} \tag{2.1}$$

From Equation 2.1, it can be seen that hydrogen is dissolved in the aluminium melt in its atomic form and that $Al_2O_3(s)$ is formed. The formation of hydrogen gas occurs during solidification, as the solubility of hydrogen in aluminium decreases dramatically from liquid to solid at the same temperature. At the melting point and 1 bar pressure, the equilibrium content of hydrogen in aluminium decreases from 0.64 ppm in the liquid state to 0.03 ppm in the solid state [9], leading to the precipitation of supersaturated hydrogen into $H_2(g)$, which causes porosity. This negatively affects end products by lowering fracture toughness and fatigue strength [4], as well as reducing the tensile properties. It can also cause blistering during hot rolling and annealing [9].

Non-metallic inclusions

Non-metallic inclusion is a collective term usually describing all solid particles and films suspended in the molten aluminium, which do not react or dissolve in the aluminium once they are formed. Inclusions are often divided between exogenous and endogenous, where the former describes inclusions that enter the melt from an external source, *e.g.,* from the refractory material. In contrast, endogenous inclusions result from reactions with aluminium, *e.g.,* the formation of Al_2O_3-films. Entrainment of Al_2O_3-films is a known phenomenon where slight movements or turbulence causes the surface Al_2O_3-films on molten aluminium to fold "dry-on-dry" into bifilms, which sink into the bulk melt perfectly wetted with the surrounding aluminium [37]. The typical size distribution, concentrations, and densities of such bifilms and other common inclusions can be seen in Table 2.1. It should be noted that the density of bifilms may vary due to trapped pores with corresponding buoyancy forces [37]. This is also the case for particles as they commonly agglomerate to each other and to bifilms.

Table 2.1: Common inclusions and their typical densities, size distributions and concentrations [9,10]. The density of "refractories" may vary as it is not a specific inclusion and is thus marked "n/a".

Inclusion	Inclusion Type	Density [g/cm³]	Size Distribution [µm]	Typical Concentrations [ppm]
Al_2O_3	Bifilms	3.97	10 - 5000	0.01 - 2
	Particles		0.2 - 30	
MgO	Bifilms	3.58	10 - 5000	
	Particles		0.1 - 5	
$MgAl_2O_4$ (spinel)	Bifilms	3.6	10 - 5000	
	Particles		0.1 - 5	
SiO_2	Particles	2.66	0.5 - 5	0.01
Al_4C_3 (carbide)	Particles	2.36	0.5 - 25	5
TiB_2	Particles	4.5	1 - 30	10 - 50
Refractories	Particles	n/a	100 - 500	0.01

If inclusions are not removed from the molten aluminium, they may cause problems during further manufacturing of the solidified metal or reduce the properties of the end product. In the worst scenario, it may also be the source of component failure during operation. Even a very low number and size of inclusions can have a detrimental effect on the properties of the solidified metal, and pinholes in rolled thin foils, as well as fractures of wires during drawing, are not uncommon [9]. Oxide inclusions and films have further been reported to decrease the fluidity and castability of aluminium melts [38]. The mentioned entrainment of bifilms may therefore also lead to several other defects in the solidified aluminium, *e.g.,* the formation of pores due to trapped air and cracks, which have been described as the most common source of porosity in castings [11]. Other reported effects of bifilms are that they are initiators of fatigue cracks and decrease the tensile properties of the aluminium [39,40].

2.2.3. Melt treatment

The undisputed negative effect of impurities on the quality and properties of the final aluminium product, with different effects for different impurities, highlights the necessity for melt treatment and refining. The melt treatment of aluminium is an extensive operation where several purification steps are often necessary to achieve sufficient melt quality, both because different steps remove different impurities and because low concentrations of certain impurities are so crucial that different methods are applied sequentially to remove the same type of impurities.

The most commonly applied melt treatment methods can be divided into floatation, sedimentation, and filtration [10]. An overview of the different methods, what they remove and the mechanisms involved, can be seen in Table 2.2. Floatation can be further specified into gas purging and vacuum treatment, as well as any removal of inclusions floating due to a lower density than molten aluminium. Gas purging is often separated between being reactive (chloride gas (Cl_2), nitrogen gas (N_2)) or inert (argon (Ar)), where both can serve a similar purpose but with different mechanisms. Both will rely on absorbing the impurities from the melt to the gas phase through differences in partial pressure (*e.g.,* hydrogen gas (H_2)), and by carrying the inclusions to the melt surface due to bubble surface tension. It is, however, only the reactive gas that will react with the impurities in the solution forming solids/inclusions, which later can be removed with other methods [13,34]. Reactive treatments such as additions of salts and fluorides are equivalent to reactive gas purging, where the intention is to remove impurities through additions of salt forming reaction products that either burn off or can be removed by other methods as solid materials.

The other sedimentation method, settling, is the removal of inclusions (and the mentioned solids) and larger agglomerates of inclusions based on the difference in density. As seen in Table 2.1, most inclusions have a higher density than molten aluminium (2.375 g/cm^3 for pure aluminium at 660 °C [41]), and thus, by holding a melt still, many inclusions will settle at the bottom of a furnace.

Filtration is a method of physically removing inclusions from the aluminium melt and will be described more in detail below.

Table 2.2: An overview of the different melt treatment methods, showing what impurities are removed and how [4,10,13,34]. For methods where no external reactant is added, it is indicated by "n/a".

Melt Treatment	Purification Method	Reactant	Impurity Removed
Floatation	Gas purging	Cl_2, N_2, Ar	H_2, alkali and alkalines, inclusions
	Vacuum treatment	n/a	Mg, Zn, Pb, H_2
Sedimentation	Reactive treatments (salts, fluorides etc.)	NaCl, KCl, AlF_3, $MgCl_2$, CaF_2 etc.	Alkali and alkalines, inclusions (oxide films)
	Settling	n/a	Inclusions, biproducts of reactive treatments
Filtration	Filtration	Different filter types	Inclusions

An overview of a common chain of process steps can be seen in Figure 2.2, retrieved from Friedrich *et al.* [13], covering the complete process route from electrolysis/scrap melting to casting. The common purification methods applied during ladle treatments are usually gas purging and reactive treatments. The casting furnace is often the main step for settling, a process step applied after other treatments have been performed. These other treatments in the casting furnace are often reactive treatments and/or gas purging if porous plugs for gas flow are installed. Gas purging is also applied in the degassing step.

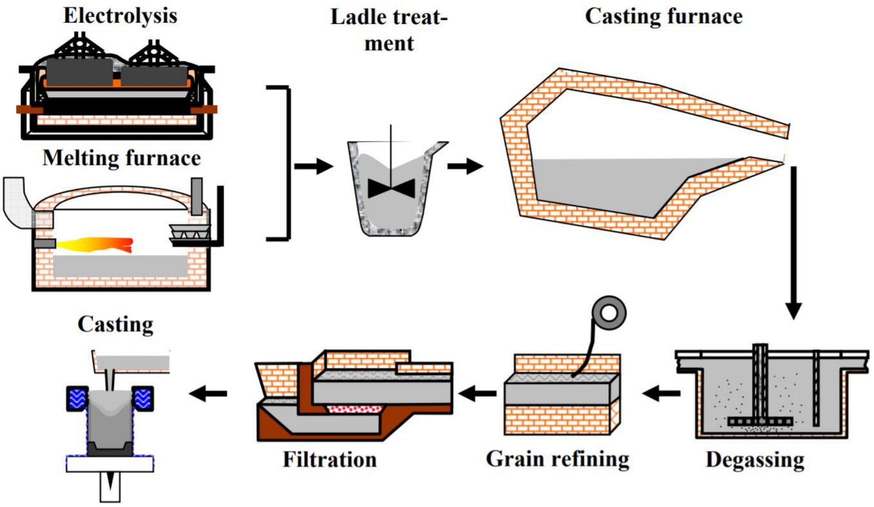

Figure 2.2: The chain of process steps during aluminium production from electrolysis/scrap melting to casting, including standard purification methods. Retrieved from Friedrich et al. [13] and reprinted with the permission of DGM.

<u>Filtration methods</u>

Filtration of aluminium melts serves the same purpose as any commonly known filtration method of a medium, *e.g.,* water, to purify the medium. For aluminium melts, the primary goal of filtration has been the removal of solid inclusions and bifilms (although other impurities have also been targeted, such as liquid salts [42]). The mechanisms of removal are debatable and have been the topic of extensive research by many scientists, and will be covered in detail in a later Chapter (2.4.1.). However, in general, the main removal mechanism for conventional filtration is physical separation, either by mechanically blocking or by particle adhesion to surfaces.

Filtration as a process for refining light metals was introduced in 1935 and was soon applied in the aluminium industry [13]. Since then, it has matured into being a very common process, and several different filtration processes have since been developed. In the early days, the available filtration processes could be classified into the following five generic types: ceramic monoliths, unbonded ceramic particulate, ceramic foams, bonded ceramic particulate, and woven ceramic fiber [43]. Noticeable is the recurrence of the word “ceramic”, as the filtration medium often is based on a ceramic refractory such as Al_2O_3. In more recent studies, the filter type classifications are narrowed down into the following types [12,13,44], where examples of each can be seen in Figure 2.3 retrieved from Conti and Netter [12]:

- Unbonded ceramic particulate is granular filters where the filter medium consists of loose ceramic tabs and/or balls in a container. Often referred to as deep bed filters (DBF).
- Bonded ceramic particulate is granular filters where the filter medium consists of ceramic grains bonded together, either as a filter plate or as porous ceramic tubes. Often referred to as bonded particle filters (BPF) in the former case or rigid metal filters (RMF) for the latter.
- Ceramic foams are open pore structure filters with high porosity, nearly equivalent to the inverse replica of a granular structure. Often referred to as ceramic foam filters (CFFs) (the main topic of the present project).

There are also additional differences between the presented filter types. DBFs are large in-line units that require much space, they are suitable for filtration of large amounts of metal (~ 1000 tons) and for the removal of inclusions with a size < 20 µm [13]. They can further hold large amounts of melt which makes alloy changing difficult. CFFs and BPFs, on the other hand, are low-cost alternatives that are easy to change and usually used only once and then replaced. RMFs are something in between DBFs and BPFs, as it is a bundle of tubes made of bonded particles. They are, however, associated with high costs regarding investment and operation and are used mainly for special applications [13].

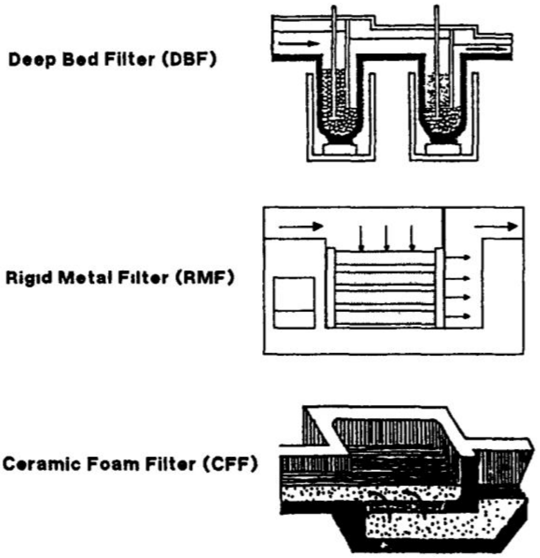

Figure 2.3: Examples of each filtration classification, from top to bottom: unbonded ceramic particulate, bonded ceramic particulate, ceramic foams. Retrieved from Conti and Netter [12] and reprinted with the permission of Elsevier.

All the filter types come in various grades, from coarse to fine, such as the different sizes of the grains/balls or pores. Thus, their properties and inclusion removal efficiencies vary accordingly. A mathematical model for determining the initial filtration efficiency of the mentioned filters, *i.e.,* DBF, RMF and CFF, was developed by Desmoulins *et al.* [45]. The output from the filtration of inclusions with a specific gravity of 4.5 over a velocity range defined by the suppliers can be seen in Figure 2.4.

It was further found that, in general, where the specific gravity differed from that of molten aluminium, the filtration efficiencies decreased in the following order for the different filters: DBF, RMF, and CFF [45].

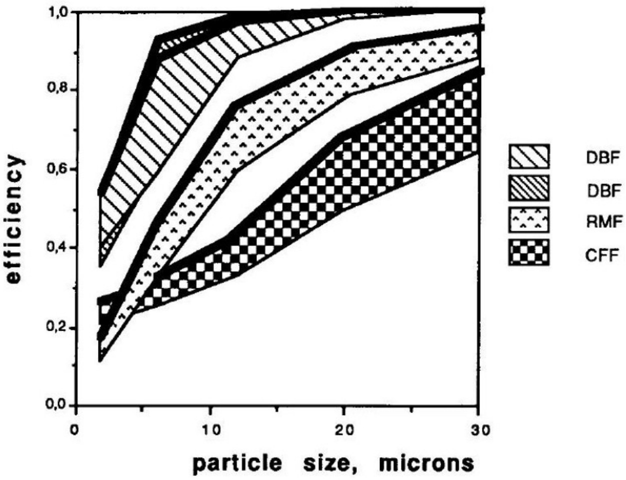

Figure 2.4: Filtration efficiency as a function of the particle (inclusion) size for inclusions with a specific gravity of 4.5. The efficiencies are calculated using a mathematical model, with filtration velocities recommended by suppliers for the different filter concepts. Retrieved from Desmoulins et al. [45]. Used with permission of The Minerals, Metals & Materials Society.

Even though these filter types have been known to the industry for several decades, developments within filtration are ongoing. An example of this is the developed XC filter, which combines a ceramic foam filter and a deep bed filter [19].

2.3. Ceramic foam filters (CFFs)

2.3.1. State of the art

The initial introduction of CFFs to the aluminium industry occurred at the beginning of the 1970s [13,46]. Since then, its popularity has increased significantly, and it has been described to be the most used filter type within the aluminium industry [13]. In 2009, it was reported that CFFs were applied in the production of > 50 % of the world's wrought aluminium [47]. The benefits of applying CFFs are that they are relatively cheap, easy to use, and usually replaced after a cast while offering good inclusion removal efficiencies. Figure 2.5 shows an example of a CFF.

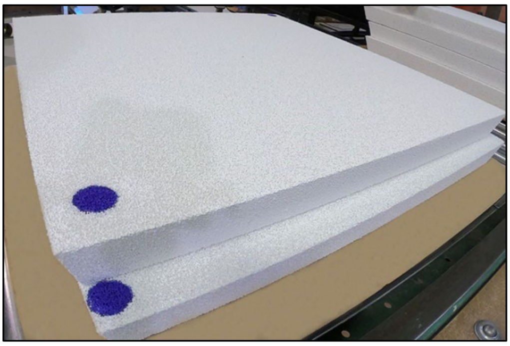

Figure 2.5: Picture showing the typical appearance of CFFs [48].

The production of CFFs is based on the replica method developed by Schwartzwalder *et al.* [49]. It is a production process consisting of several steps, starting with a foam or sponge usually made of polyurethane (PUR) that is coated with a ceramic slurry, *e.g.*, by immersing the foam in a bath of the slurry or by spraying. The excess slurry is then removed by either running the foam between two rollers or by centrifuging to squeeze/force out the excess slurry. The uniformly ceramic-coated PUR foam is then burned at high temperatures (typically 1000 – 1700 °C [50]), causing the foam to decompose and burn off/vaporise while the ceramic slurry sinters or fuses into a replication of the original foam.

Several patents exist describing the production of CFFs for filtration of aluminium [51–53]. The patent by Brockmeyer [53] has been the basis for most filter producers in recent decades. According to this patent, the main component is Al_2O_3, constituting ~ 50 – 80 % of the total composition. Al_2O_3 is preferred due to its high resistance toward chemical attacks in molten aluminium, as well as its structural and mechanical strength [53]. Still, other ceramics such as Al_2O_3-SiO_2, Al_2O_3-ZrO_2, SiC, and $ZrSiO_4$ are also applied (however, not necessarily specific for aluminium) [54]. The other constituents, according to the patent [53], are 1 – 5 % montmorillonite (to achieve correct rheology of the slurry), 1 – 10 % ceramic fibers (to increase strength and act as a crack growth inhibitor), and 5 – 25 % of a phosphate binder. The purpose of a binder is to reduce the temperature of the sintering step and thus reduce the energy consumption, which is essential as CFFs, like most refractories, are cost sensitive. Phosphate bonded ceramics are very well suited for fast sintering processes and a reduction of the sintering temperature compared to sintering of, *e.g.,* pure Al_2O_3 [55]:

$Al(H_2PO_4)_3$ (monoaluminium phosphate) → $Al(PO_3)_3$ (315 °C)

$Al(PO_3)_3$ → metaphosphate glass (between 1090 and 1300 °C)

metaphosphate glass → $AlPO_4$ (between 1300 and 1500 °C)

The formation of $AlPO_4$ from $Al(PO_3)_3$ occurs at significantly lower temperatures in the presence of Al_2O_3, *i.e.,* between 700 °C and 1000 °C [55], and it is the formed $AlPO_4$ that acts as the bonding phase and coats the Al_2O_3-particles [56].

The microstructure of an as-produced CFF can be seen in Figure 2.6. The functional pores and filter struts are the key features that are openly visible. The struts (and the functional pore walls) are the material of which the filters are made, *i.e.,* the ceramic slurry that has replicated the PUR foam. Thus, a CFF is basically a network of struts. The functional pores represent the main porosity in the filter and are the open spaces through which the molten aluminium flows. The size and density of the functional pores, which are strongly connected, are perhaps the most critical parameters for removing inclusions. They are usually specified by producers as PPI (pores per inch) or grades ranging from 10 – 80 [57,58], where, *e.g.*, a filter grade/PPI of 30 indicates a range in functional pore size of ~ 1640 – 2170 µm [58]. In Figure 2.6 (b), the cross-section of a filter strut is illustrated. It can be seen that the solid is not completely dense, as there are pores present, which usually are referred to as material pores/porosity. Also, all the filter struts are hollow, with these strut cavities appearing triangular when viewing the cross-section. Every strut cavity results from the decomposition of the PUR foam, leaving a void where the original structure once was.

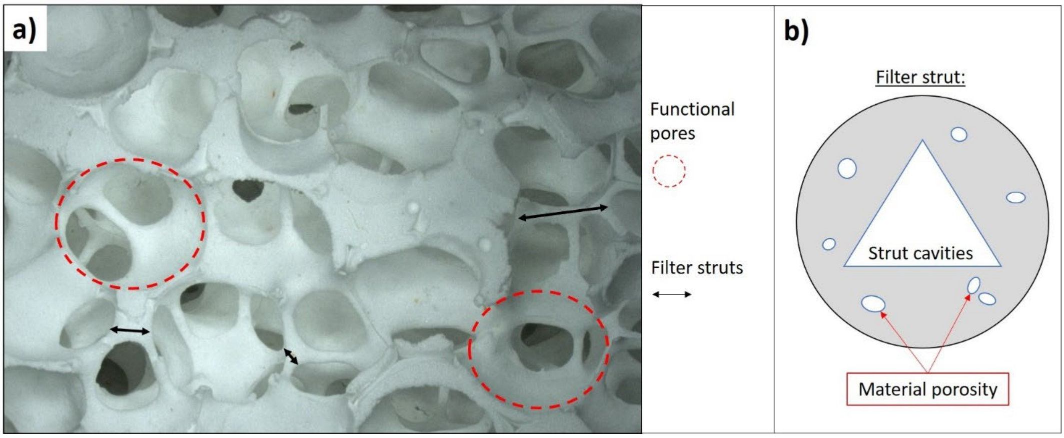

Figure 2.6: Overview of the microstructure of CFFs presented by: (a) photograph of a filter with the functional pores and filter struts marked and (b) sketch of a filter strut cross-section showing its strut cavity and material porosity. Retrieved from Bergin et al. [59], published under the Creative Commons Attribution 4.0 International License: https://creativecommons.org/licenses/by/4.0/.

2.3.2. Priming

The CFF plate is seated in a filter box during industrial application. A schematic representation of this is shown in Figure 2.7, adapted from Gauckler *et al.* [10]. The figure shows the filtration and metal launder levels during steady-state conditions, *i.e.,* when the process is stable, where Δh is the difference in metal height before and after the filter. This height difference is necessary to achieve sufficient and constant flow through the filter during filtration [10]. It is further often referred to as the pressure drop over the filter, and initially, it is only affected by the properties of the molten aluminium and the filter, however with time, it will also depend on the inclusions deposited on and within the filter [9].

The initial step of filtration when using CFFs is priming, which is a process step where the functional pores of the filter are filled with molten aluminium melt and a flow through the filter is achieved. Preferably, for an optimal filtration process, the filter should be fully primed, *i.e.,* all functional pores/possible flow paths should allow for melt flow. To achieve this, it is essential to preheat the filter and have a driving force high enough to overcome the surface tension of the Al_2O_3 film [60], as well as for removing the air entrapped in the functional pores. The traditional method to achieve this in an industrial setting has been to apply a gravity head, acting as a driving force through the metallostatic pressure. The simple definition of this metallostatic pressure, where h_p in Figure 2.7 is the necessary height to achieve priming for a given filter, is:

$$P = \rho \cdot g \cdot h_p \tag{2.2}$$

where P is the pressure, ρ the density of the molten aluminium, g the gravitational acceleration, and h_p the height of the gravity head, *i.e.,* priming height. Gauckler *et al.* [10] suggested a derived correlation where the functional pore window size, *i.e.,* the size of the entrance to the functional pores, surface energy, and wetting angle are included:

$$P = -\rho \cdot g \cdot h_p = \frac{4 \cdot \gamma_{LS}}{\varphi} \cdot \cos\theta \tag{2.3}$$

where γ_{LS} is the surface energy solid/liquid ($Al_2O_3/Al = 860$ dyn/cm), φ the window size of the filter's functional pores, and θ the wetting angle of aluminium on alumina.

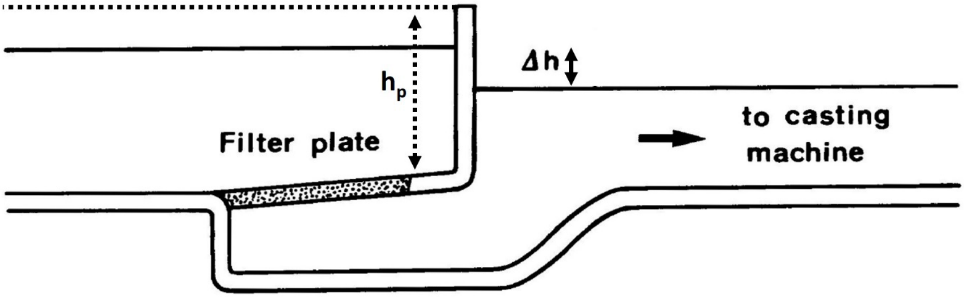

Figure 2.7: Illustration of (i) how the CFF plate often is situated in a filter box, (ii) how there is a pressure drop over the filter during a steady state of filtration (Δh), and (iii) how a gravity head is necessary to achieve filter priming (h_p, dotted line). Adapted from Gauckler et al. [10].

An overview of the necessary priming heights for filters with different PPI can be seen in Figure 2.8. The values are retrieved from the studies by Gauckler *et al.* [10], Dore [60], and Keegan *et al.* [20]. It is clear that an increase in PPI, which correlates with a decrease in functional pore size, leads to an increase in the priming height. Thus, with an increase in PPI, the external forces necessary to achieve priming are higher.

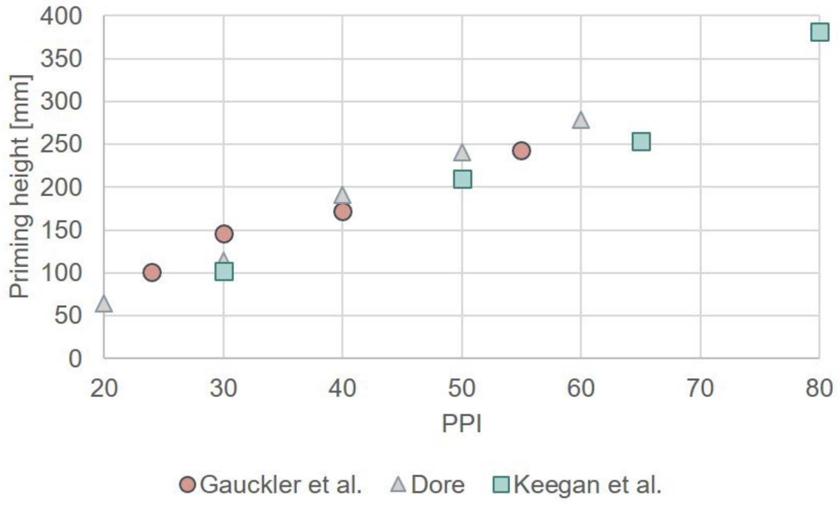

Figure 2.8: Overview of necessary priming heights for different filter PPIs. Based on values from Gauckler et al. [10], Dore [60] and Keegan et al. [20].

Although applying a metallostatic pressure through a metal priming height is still the most common method in the industry, there have been technological developments in recent years, offering alternatives to achieve filter priming. Some of the developments will be covered more in detail in the sections below as they have been applied in the current study, while others [61,62] will not.

Electromagnetic priming

Electromagnetic priming is a technology patented in the lab of the Department of Materials Science and Engineering at NTNU [63–65]. A brief introduction to the technology is given below.

A coil of copper tubes, circular with tubes in two layers for the current study, with a high alternating current induces a magnetic flux. The strength of the flux will be affected by the number of turns of the copper tube, the applied current, and the length of the coil, among other things [65]. The frequency of the alternating current is also of importance, where an increase in penetration depth of the electromagnetic forces into the molten aluminium is associated with a decrease in the frequency [65]. Furthermore, the frequency affects the change in the current direction, where a high frequency leads to a high rate of change. The Lorentz forces in the melt are described to follow the “right-hand rule” as a cross-product of the current- and magnetic flux density. Thus, the direction of the Lorentz forces is also affected by the frequency of the applied current. As the Lorentz forces generally would induce a velocity field within the molten metal, these frequent changes in the direction of the forces will create vibrations within the liquid melt [65]. These vibrations will, in turn, rupture the aluminium oxide layer at the melt-filter interface, thus achieving filter priming.

Drain free filtration (DFF®) priming

The drain free filtration (DFF®) technology is a newly developed and patented [66] technology by Norsk Hydro ASA. There are other advantages with the technology than priming, such as the economic savings as there is no metal that needs to be drained at the final stage of filtration. However, it is the priming process that is the development in the current context. The driving force for priming, in this case, can be described as the inverse of conventional priming, as the CFF is primed from below. This is achieved by having two chambers divided by a partition wall, where the filter is seated in one, and as the molten aluminium enters the bottom of both chambers, an ejector reduces the pressure of the system, causing the melt to rise. As the melt meets resistance in the filter chamber when the priming starts, the melt in the other chamber continues to rise, representing the priming height similar to conventional priming. When priming is complete and the filtration process starts, the flow is opposite of the priming direction, with melt passing over the partition wall. The reverse priming concept has been studied on a laboratory scale, where no influence of the reverse priming on the filtration behaviour was observed [67]. Furthermore, the DFF® technology has been successfully applied in pilot scale conditions, showing good filtration efficiencies, and has recently been installed in a casthouse [68].

2.4. Filtration performance

2.4.1. Fundamental filtration theory

The fundamental theory of filtration can roughly be divided into the three subchapters below, covering the modes and mechanisms of filtration, as well as approaches for the estimation of filtration efficiency.

Filtration modes

There are two filtration modes of CFFs, *i.e.,* cake filtration and deep bed filtration [9,10,14]. The two modes are differentiated by where the inclusions are captured, see Figure 2.9. Note that the figure shows the extreme points of each mode to better highlight the differences between the two. For cake filtration the inclusions deposit at, or in the area of, the filter entrance and thus forming a filter cake. A requirement for a cake is that the size or combination of size and concentration of incoming inclusions are relatively large compared to the pores at the filter entrance so that inclusion sieving can occur. For deep bed filtration, the inclusions are captured through the whole thickness of the filter. It is important to note that both modes are likely to coexist in many cases, depending on the concentration and size of incoming inclusions. However, unless there is a surge of inclusions, deep bed filtration would be expected to be the main mode in the early stages of filtration, while with time cake filtration would gradually become dominant. Cake filtration is associated with a more significant increase in filtration efficiencies and pressure drop over the filter with time compared to deep bed filtration [9].

Filtration mechanisms

The inclusion removal for cake filtration mode is a simple mechanism of sieving and interception due to the inclusions being larger and in higher concentrations than what simultaneously can pass through the pores. For deep bed filtration it is more complicated, where the capture of inclusions is considered to occur in two steps, *i.e.,* transport of inclusions to the filter surface with the subsequent attachment of the inclusions [14].

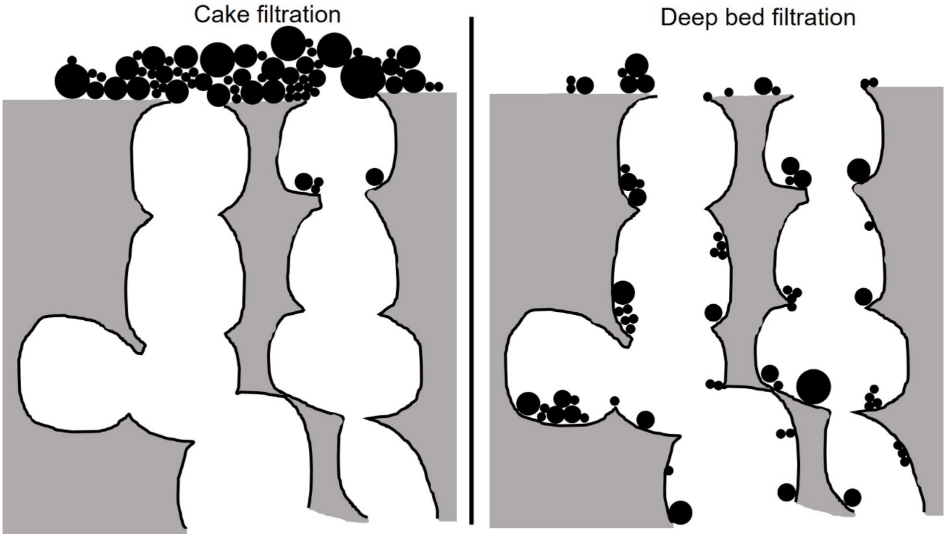

Figure 2.9: Illustration of the cake filtration mode and the deep bed filtration mode, where the former captures inclusions at the filter entrance while the latter captures inclusions through the whole filter thickness.

The mechanisms for transport of inclusions to the filter surface are commonly described as interception, inertia, gravity, Brownian motion, and hydrodynamic effects, shown schematically in Figure 2.10 [9,10,14].

- Interception occurs when an inclusion follows its flow line and is directly intercepted, *i.e.,* collides with the filter surface.
- Inertia is defined as when an inclusion, due to its apparent weight, is unable to follow its flow line when the line changes direction and thus hits the filter surface.
- The gravity transport mechanism occurs when the inclusion density is significantly higher than the surrounding molten aluminium, causing the inclusion to follow gravitational forces rather than the flow line.
- Brownian motion is an effect of molecular bombardment on the inclusion, causing the inclusion to randomly move (microscopic movement).
- Hydrodynamic effects apply for inclusions that are not spherical but rather elongated or irregularly shaped, *e.g.,* bifilms and plates, which due to the velocity distribution within the filter, will wobble and tumble and likely not follow the flow lines.

According to Eckert [14], the relative dominance of each transport mechanism is dependent on the size and type of inclusions, flow velocity of the molten aluminium, as well as temperature and properties of the filter surface. It was further believed that inertia is the dominant mechanism for aluminium filtration, which is supported by Gauckler *et al.* [10] with the addition of the mechanisms interception and hydrodynamic effects. Engh [9], however, describes inertia as a mechanism that, in general, is not important for filtration of metal melts, except for melt velocities higher than 0.1 m/s and inclusions sizes larger than 100 μm. It was further claimed by Engh [9] that Brownian motion as a removal mechanism plays a minor part for inclusions larger than 1 μm and suggests that gravity is the most dominant removal mechanism.

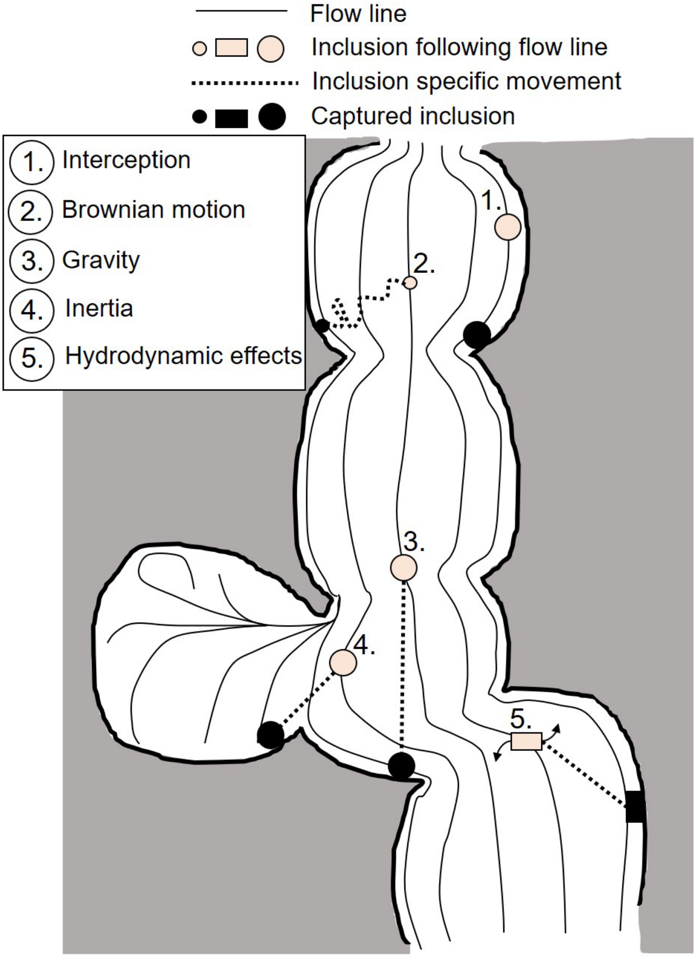

Figure 2.10: Illustration of the five filtration mechanisms of deep bed filtration: (1) interception, (2) Brownian motion, (3) gravity, (4) inertia and (5) hydrodynamic effects.

The attachment of inclusions to the filter surface once they have been transported there is also an issue of debate. Gauckler *et al.* and Eckert describe the attachment of inclusions as a result of Van der Waals forces [10,14] and/or pressure [14]. A different approach to inclusion attachment has also been described by Engh [9], suggesting that there is a net reduction of Gibbs energy for inclusions detained at the interface between the melt and the filter due to a high relative interfacial tension of the filter surface in contact with the melt. Both Engh [9] and Gauckler *et al.* [10] describe further that even though an inclusion has been attached to the filter surface, it can be re-entrained into the melt. Explanations for this phenomenon have been proposed to be due to the rough surfaces of both the inclusion and filter surface at a microscopic scale (low actual contact area) [9], the increase in shear stresses due to sudden increases in melt flow rate [9,10], and the effect of the filter interstitial velocity (the local melt velocity within the filter functional pores) exceeding a particular threshold limit [14].

It is further noted that this re-entrainment is not observed for steel filtration, which can likely be explained by inclusions sintering or chemically reacting with the filter due to the higher temperature (1600 °C) [9].

Filtration efficiency

The filtration efficiency, often also referred to as removal efficiency, is the fraction of inclusions removed by the filter, in %. When assessing the performance of a filter, its filtration efficiency is perhaps the most critical parameter, as inclusion removal is the main intention of applying a filter. It can, in all its simplicity, be described by Equation (2.4) below:

$$\text{Filtration efficiency} = \frac{C_{before} - C_{after}}{C_{before}} \cdot 100\ \% \tag{2.4}$$

where C_{before} and C_{after} equals the concentration or number of inclusions before and after the filter, respectively.

Several equations exist to further describe and estimate the deep bed filtration efficiency. Although this has not been the topic of the present project, a brief introduction is given as it increases the understanding of the filtration process and important parameters. Apelian *et al.* [15] derived a correlation between filtration efficiency and the superficial velocity, *i.e.,* the overall melt velocity over the filter, through process modelling with deep bed filtration of TiB_2 particles in an aluminium melt:

$$\text{Filtration efficiency} = 1 - e^{-\frac{K_0 \cdot L}{U_m}} \tag{2.5}$$

here L is the filter thickness [cm], and U_m the superficial velocity [cm/s]. K_0 is defined as a kinetic parameter [s^{-1}] which must be determined experimentally and is a function of the superficial velocity, the inclusions size, the filter grain size, and the melt system. Although the results by Apelian *et al.* [15] were achieved using deep bed filters and not CFFs, the general filtration process between deep bed filters and deep bed filtration mode in CFFs is believed to be comparable. Furthermore, the equation describes the initial filtration efficiency before inclusions are deposited, and if it is to be applied in more general terms, it must be assumed that the attachment of inclusions will not alter the filtration process. The experimental results of Apelian *et al.* [15], as well as Equation (2.5), show that increasing filtration efficiencies would result from decreasing melt velocities or increasing filter thickness. A simplified version of Equation (2.5) was also described by Apelian *et al.* [15], where $\lambda = K_0/U_m$, and this equation has been applied to describe filtration efficiency also in more recent publications by other scientists [10,14,45,69,70]. Even other equations with a basis in Equation (2.5) have also been described, *e.g.*, where the superficial velocity (U_m) has been replaced by the velocity of metal through the filter (V_f) [71,72], *i.e.,* the interstitial velocity [14]:

$$V_f = \frac{F}{\varepsilon \cdot \rho \cdot A_f} \tag{2.6}$$

where F is the metal flow rate [g/s], ε the void fraction of the filter, ρ the density of the molten aluminium [g/cm^3], and A_f the surface area of the filter [cm^2]. This addition indicates that increasing filter void fraction and surface area would increase filtration efficiency. Similar equations described by other authors [9,73–75] have highlighted the importance of the following properties, which have not been included in Equations (2.5) or Equation (2.6): inclusion diameter, collector diameter (such as strut diameter or pore diameter), wettability (between inclusion, melt and filter), and adhesion properties of the melt and inclusions.

2.4.2. Experimentally assessed filtration performance

Inclusion quantification methods

There are mainly two methods for inclusion quantification and identification that are commonly applied in the aluminium industry today, *i.e.,* LiMCA [26] and PoDFA [27] (described more in detail below). Although the mentioned methods are commonly applied and well suited for industrial applications and testing, this is not necessarily the case in laboratory experiments. Then other methods such as spent filter analysis using microscopes or cold-PoDFA can be applied (described in detail below).

The LiMCA, or its precursor, was developed in the early 1980s in a cooperation between McGill University and Alcan in Canada as a rapid method intended to measure the concentration and size distribution of inclusions larger than 15 to 20 μm [76]. The technique utilises the electrical sensing zone principle (or coulter counter principle), which counts particles suspended in a conductive liquid by the difference in conductivity between the particle and the liquid [77]. LiMCA consists of a glass tube with an orifice of a fixed size, 320 μm, which is submerged in the molten aluminium. With regular time intervals, ~ 7.5 ml of the molten melt is drawn through the orifice and into the glass tube. At the same time a constant electrical current is passed through the orifice, completing an electrical circuit between two electrodes, one within the tube on one on the outside [77]. When a non-conductive inclusion passes the orifice there is a rise in the electrical resistivity of the orifice, which is measured as a voltage pulse in the presence of a constant current, where the amplitude of that pulse is proportional to the volume of the particle [77]. Thus the number and size distribution of inclusions in the molten aluminium can be measured in situ several times (typically every 2 minutes [76]) during the duration of a cast. The LiMCA data can be reported in several ways, where k/kg indicates the number of inclusions (in thousands) per kg aluminium melt. This is accompanied by a N## which indicates the size of the inclusions included in the count, whereas N20 is often used, indicating that only inclusions larger than 20 μm are included.

PoDFA as a standardised method for concentrating inclusions with the use of filtration was developed by Alcan in the 1960s. Since then, the method has been a standard and well-known approach in melt cleanliness assessment [76]. The sampling is performed by pouring the molten aluminium to be analysed into a crucible fixed with a very fine filter at the bottom. The crucible is then positioned at a PoDFA station, where a chamber beneath the crucible is vented into vacuum, enabling the sampled melt (ideally ~ 1kg) to pass through the filter. As the filter is very fine, a cake of all the inclusions is concentrated at the filter inlet, which is cut and polished before being analysed in microscopy by a trained operator. The operator can then estimate the number of inclusions by looking at the fraction area covered by inclusions, giving the amount in mm^2/kg, and identifying what kind of inclusions are present. The PoDFA sampling is usually and ideally performed in situ from the molten melt, but in cases where that is not possible, a solution can be cold-PoDFA. The principle is the same, except the metal is allowed to solidify for later to be remelted carefully and then filtrated and analysed the same way as for standard PoDFA. It has been shown that the resulting inclusion amount and types differ significantly between standard and cold-PoDFA [78]. Thus, these two methods should not be compared, and the standard PoDFA should be applied if possible.

Recent developments within inclusion quantification have been performed at the Department of Materials Science and Engineering at NTNU, where the automated metal cleanliness analyser (AMCA) is a promising method not yet industrialised [79,80]. It is based on automatic image analysis of cast metal samples, identifying inclusion amounts and types. In the case of analysing PoDFA samples, it replaces the time-consuming and expensive step of sample analysis performed by operators, which has the risk of human bias. The AMCA method was applied as a tool in the present project.

Observed filtration modes and mechanisms

Through metallographic investigations of spent CFFs, Strom *et al.* [16] observed that the majority of the inclusions were captured in deep bed mode in the upper sections of the filter, with decreasing quantity from top to bottom, an observation that has also been made by several other scientists [18,70,81]. Laé *et al.* [70] observed that the number of inclusions as a function of the filter depth exhibited a decreasing exponential profile, something that previously has been derived mathematically by Eckert *et al.* [14]. Using the simplified version of Equation (2.5) at different filter depths, Laé *et al.* [70] further stated that the filtration efficiency could be described by plotting a straight line for ln(1 – Filtration efficiency(z)) as a function of the filter depth (z), where the "filtration efficiency" is described by the simplified version of Equation (2.5) [70].

There are few descriptions of experimentally observed filtration mechanisms in the literature, likely due to the challenge of achieving good observations. However, Laé *et al.* [70] proposed that the most dominant mechanisms in molten aluminium filtration are interception and gravity. Damoah *et al.* [81] further performed simulations of inclusion trajectory paths, velocity distributions and capturing locations, which were coupled with experimental observations, and reported differences that were linked to inclusion size. Larger inclusions were more likely to attach at intersections/windows between functional pores, while smaller inclusions were dispersed more evenly within each functional pore. This was explained by smaller inclusions being more affected by turbulent fluctuations than inertial effects, contrary to the case for larger inclusions [81].

An additional mechanism observed by other scientists [16,18–20,70,81] is the formation of oxide skins and/or inclusion "bridges" often occurring across windows to the functional pores (the narrow entrance to the pores). These oxide skins and bridges have covered or partly covered the windows of the functional pores, acting as barriers hindering the oncoming inclusions from passing by. The likely mechanism behind these formations is that the oxide skins have covered the functional pore windows and then captured new inclusions like a net or that the bridge has been built step by step over time by agglomerating inclusions. Keegan *et al.* [20] observed these bridges mainly in the finest filters, whereas for the 30 and 50 PPI filters, there were no or almost no observations of bridges.

It is important to note that the proposed and observed mechanisms are based on different observations, often on visual analysis of spent filters which is a 2D analysis of a 3D structure, and very coincidental since only a small part of the whole filter structure is analysed. Thus, observed mechanisms are qualitative results and, to a large degree, indications rather than absolute conclusions.

Effect of PPI

The filtration efficiency and performance as an effect of PPI have been studied in numerous publications, where a summary of many of them can be seen in Figure 2.11. From the figure, it can be seen that in general, an increase in PPI corresponds to an increase in filtration efficiency [16–19], although in some cases, the differences are small. An opposite observation was reported by Laé *et al.* [70], where an increase in PPI from 30 to 50 in pilot scale experiments led to a decrease in average removal efficiency from 80 % to 62 %. This was explained by a higher filtration speed (superficial velocity) for the 50 PPI filter and that the two CFFs were from different suppliers. It has previously been shown that it is the morphology of the filters that affect the filtration efficiency (*e.g.,* pore size), and the morphology can vary extensively between filters from different suppliers even at the same nominal PPI [70]. A sensitivity analysis performed by Laé *et al.* [70] showed that for filters from the same supplier, the filtration efficiency would increase with increasing PPI.

Although the general trend of an increased filtration efficiency with increasing PPI is undisputed, both CFFs with a low PPI (*e.g.,* 30) and a high PPI (*e.g.,* 60) can achieve excellent filtration efficiencies, see Figure 2.11. Thus, the effect of PPI on filtration efficiency can be viewed slightly differently, as described by Keegan *et al.* [20], where an increase in PPI increases the reliability of the filter, as the range in measured filtration efficiencies is reduced.

Effect of melt velocity and temperature

Through early laboratory experiments using aluminium with added titanium diboride particles (TiB_2) as inclusions for filtration assessment, both Apelian *et al.* [15] (as mentioned in relation to Equation (2.5)) and Conti *et al.* [12] reported decreasing filtration efficiencies with increasing superficial velocities. A later sensitivity study on the effect of superficial velocity on the filtration efficiency was performed by Laé *et al.* [70] for a 60 PPI filter with 50 μm inclusions of density 3200 kg/m^3, verified that the filtration efficiency decreases for increasing superficial velocities.

The effect of temperature on the filtration efficiency was investigated in a study by Conti *et al.* [12], where it was concluded that the filtration efficiency is not affected by the temperature of the aluminium melt.

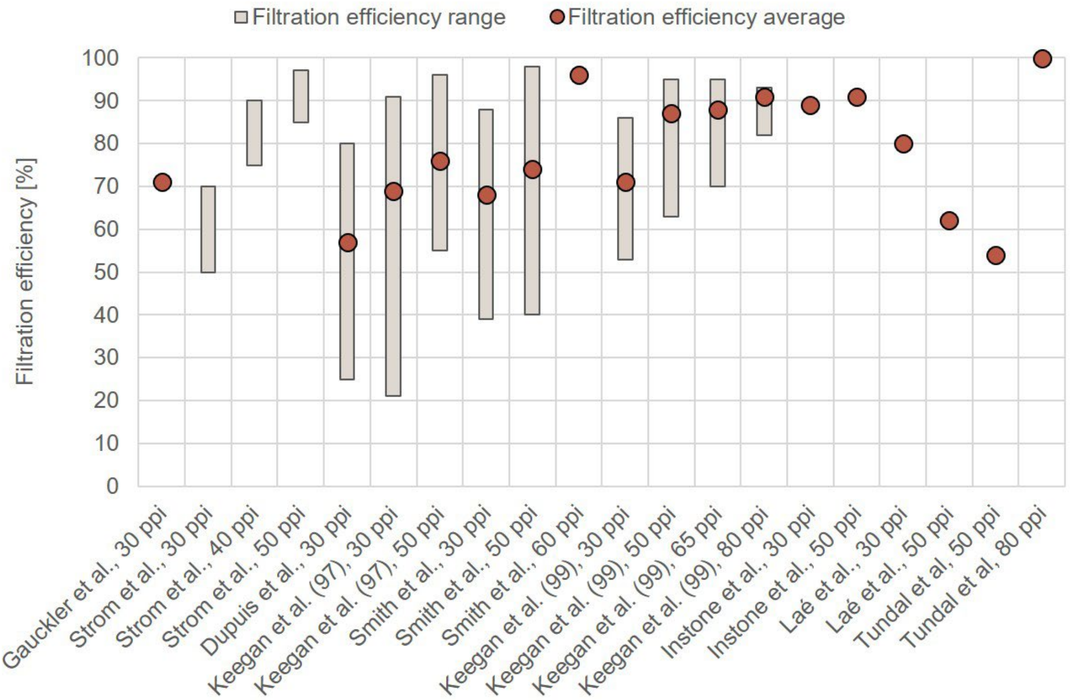

Figure 2.11: Summary of reported CFF filtration efficiencies, both average and ranges, based on studies by different authors [10,16–20,68,70,82], where the author's name and filter PPI are on the x-axis. The efficiencies are based on inclusion sizes > 15 or 20 µm, and the data is retrieved from filtration trials with different alloys, superficial velocities, number of trials, and amounts of melt.

Effect of grain refiner additions

The detrimental effect of grain refiner additions on the filtration efficiency when additions are made before the filtration step is a well-known problem reported by many scientists [68,70,83–86]. The effect has been described to be an issue when the amount of inclusions in the melt is high, while for a clean melt the effect has been reported to be insignificant [83,85]. There is no undisputed mechanism explaining the detrimental effect of grain refiners. Still, several scientists [83–85] have proposed that the observed effect is due to the surge of grain refiner particles (titanium diboride (TiB_2) or titanium carbide (TiC)), either preventing the formation of- or breaking the bridges (described in Chapter 2.4.2.) already formed at the functional pore windows. Towsey *et al.* [83] investigated if there were any effects of other elements/constituents within grain refiner rods by adding (i) a pure aluminium rod (just the rod to see the impact of any potential undissolved aluminium), (ii) a rod containing only the $TiAl_3$ phase (no grain refiner particles to check for any impact of partially dissolved $TiAl_3$ particles), and (iii) a generally high inclusion load. Neither of these elements showed any significant negative impact on the filtration efficiency, similar to that of the grain refiner rod additions [83].

As the grain refiners come in many different compositions, also with different particles that are the acting grain refining substrates, an interesting question is whether this influences the detrimental effect on filtration. Through testing of several TiB_2-based grain refiners with different compositions, *i.e.,* grain refiner where the acting particle is TiB_2 but there is a varying amount of, *e.g.*, excess Ti, which is expected to affect agglomeration of particles, Towsey *et al.* [84] reported that the different grain refiners affected the filtration performance with varying degree. Keegan *et al.* [85] further stated that the AlTi3B1-rod appeared to have the most severe impact on the filtration performance.

Effect of surface chemistry and -roughness

In the early stages of CFF and filtration research, the focus has largely been on predictive estimations of the filtration process and filtration mechanisms, the effect of functional pore sizes and PPI, and the effect of melt velocity *etc.* Little focus has been directed towards studying the effect of the filter surface and/or the filter material, where the filters used almost exclusively have been Al_2O_3-based. However, the impact of the filter surface and filter chemistry is a topic that has gained interest in recent years.

SiC-based filters, with a composition of ~ 60 % SiC (silicon carbide) and ~ 30 % SiO_2 (silica), have been studied in comparison with Al_2O_3-based filters by some scientists [87,88], both on the pilot- and laboratory scales. Bao *et al.* [87] performed pilot scale trials and reported a slightly improved filtration efficiency for the SiC-based filter compared to the Al_2O_3-filter. This was further supported by Syvertsen *et al.* [88] through a comparative study with both laboratory- and pilot-scale trials, where the improved performance of the SiC-based filters over the Al_2O_3-based filters was more significant. A series of different oxide-based CFF surfaces have further been tested through filtration trials by Voigt *et al.*, both in a foundry environment [22] and in pilot-scale filtration experiments [23]. The filter surface chemistries were produced through the replica method by Voigt *et al.* [89,90] at TU Bergakademie Freiberg by applying a combined dip-spin coating procedure where an Al_2O_3 skeleton was coated with a slurry containing the new oxide, with subsequent sintering at high temperature without the use of a binder. The following oxide based filter surface chemistries were tested: SiO_2 (silica) [22], TiO_2 (rutile) [22,23], Al_2O_3 (alumina, coated on the Al_2O_3 skeleton to achieve comparable pore size) [22,23], $3Al_2O_3{\cdot}2SiO_2$ (mullite) [22,23], $MgAl_2O_4$ (spinel) [22,23]. Through testing in the foundry environment [22] using 2.3 kg of an AlSi7Mg alloy and analysing the filter post filtration in SEM, it was observed that the filters with the surface chemistries of Al_2O_3 and $MgAl_2O_4$ contained the most inclusions, while the three remaining surfaces contained similar amounts (bifilms were not counted). The pilot scale filtration trials [23] were performed with 750 kg of an AlSi7Mg0.3 alloy with the addition of inclusions to have comparable amounts and types of inclusions between the different trials. Based on measurements with LiMCA, it was reported that all filters showed average filtration efficiencies higher than 85 %, where the Al_2O_3 filter exhibited the better average removal efficiency overall, while the TiO_2 filter showed the worst average removal efficiency. The $3Al_2O_3{\cdot}2SiO_2$ filter exhibited the best filtration efficiency for inclusions with a size < 60 µm, but for larger inclusions the filtration efficiency was partly very low and thus the overall filtration performance was not favourable, even less so than for the $MgAl_2O_4$ filter [23].

Voigt *et al.* have further investigated the effect of surface roughness of Al_2O_3 filters [24,25], functionalised nano-surface of Al_2O_3 filters [25,86], and carbon bonded Al_2O_3 filters [24] on the filtration performance and efficiency of CFFs. The rough and functionalised nano-surface of the filters were produced by applying a coating slurry consisting of Al_2O_3 particles/powder of different sizes, ranging from very small (d_{50} = 80 nm, for the nano filter the slurry was 100 % of these) to larger

($d_{50} = 0.5$ µm and $d_{50} = 33$ µm, the rough filter was made with 50 % of each), where the reference filters were made with a combination of several particle sizes [25]. The effect of filter surface roughness was tested in a pilot scale loop filtration line using 1.3 tons of pure aluminium (Al99.5), where the rough filter was observed to exhibit an improved filtration performance compared to the reference and functionalised nanofilters [25]. The enhanced filtration performance included a higher average filtration efficiency than the other filters, as well as a strong decreasing trend of the LiMCA N20 counts before the filter (the melt was running in a loop) not observed for the other filters. The rough filter performance was accompanied by higher resistance to flow. This higher pressure drop over the filter compared to the others could be traced back to an increased number of inclusion deposits. The effect of functionalised nano filters was tested in both short-term and long-term filtration trials, where no significant difference in filtration performance was observed compared to the reference filters [25,86]. The effect of carbon bonded Al_2O_3 filters was investigated through two short-term filtration trials in a foundry environment by analysing the metal that had passed through the filters using cold-PoDFA. It was shown that the carbon bonded filter exhibited an improved filtration performance compared to the Al_2O_3 reference, as well as an improved performance compared to the Al_2O_3 reference with increased surface roughness [24].

2.5. Chemical and thermal stability of CFFs

In the previous chapter the filtration performance of CFFs was discussed, which perhaps is the most important and thereby frequently studied property of these filters. However, even other properties could indirectly affect the filtration performance or be requirements for the actual filter application. Two of these properties are the chemical stability of CFFs, *i.e.,* to what degree the filters are inert in contact with aluminium and its alloys, and the thermal stability of CFFs, here defined as the (compression) strength of the filters when exposed to high temperatures. Additionally, the strength of the filters at room temperature is essential during handling and transport, as the filters are weak and brittle materials. During use the filters are subjected to harsh environments, both during the placement of the filters in the filter box with potential thermal shocks and subsequent preheating, as well as during contact with the flow of hot and corrosive aluminium and aluminium alloys. Thus, the filter's susceptibility to react with molten aluminium and its resistance to mechanical and thermo-mechanical stresses, as well as these effects' impact on the filter integrity, are of great importance but have not been studied in detail.

2.5.1. Chemical stability of CFFs

The chemical stability of CFFs can be viewed in terms of the constituents of the filters (as presented in Chapter 2.3.1.): the chemical stability of additions and constituents in minority, *e.g.,* the binder, and the chemical stability of the main constituent, *i.e.,* the ceramic material.

Chemical stability of the phosphate binder in CFFs

As described in Chapter 2.3.1., CFFs for molten aluminium filtration have in the last decades been dominated by Al_2O_3-based filters with a phosphate binder, more specifically where $AlPO_4$ acts as the bonding phase. In 2009 it was estimated that 98 – 99 % of the total use of CFFs in aluminium casthouses were of this filter type [21], and they are still widely used today. It is, however, a known phenomenon that the commonly used phosphate binder is not chemically inert during filtration of aluminium alloys high in magnesium. Despite this, very little has been published on the topic and there is no clear understanding as to why and how the binder reacts.

Through immersion testing of phosphate bonded Al_2O_3-based filters in a 5182 aluminium alloy (typically ~ 4.5 wt.-% Mg and ~ 0.4 wt.-% Mn), Aubrey *et al.* [21] confirmed the presence of Mg_3P_2 and MgO in the spent filters using x-ray diffraction, and proposed the following reaction:

$$3AlPO_4 + 3Mg \rightarrow Mg_3P_2 + 3MgO + AlP \tag{2.7}$$

Another possible reaction has been described by Solem *et al.* [91]:

$$2Al + AlPO_4 + Mg \rightarrow AlP + MgAl_2O_4 \tag{2.8}$$

Solem *et al.* [91] further published Gibbs free energy (ΔG^0) diagrams, with ΔG^0 as a function of temperature, for reactions between common elements in molten aluminium and phosphorus (1 mole). Out of the chosen elements present (C, Na, Si, Al, Fe, Ca) at the temperature interval of interest (~ 600 – 800 °C), the formation of AlP was the most favourable, *i.e.,* with the most negative ΔG^0, as the elements calcium and iron showed a higher affinity to react with aluminium rather than phosphorus [91]. However, the presence of excess magnesium and the formation of Mg_3P_2 were not included in those diagrams. Still, if they were, it would have shown that the formation of Mg_3P_2 would be more favourable (more negative ΔG^0) than the formation of AlP at the described temperature interval. In a related study by Doutre [92], not on the stability of CFFs but on bone ash, a fine powder often used in the aluminium industry where the main constituent is $Ca_3(PO_4)_2$ with small amounts of $CaCO_3$, $Mg_3(PO_4)_2$ and CaF_2 [93], it was established that both AlP and Mg_3P_2 can be reaction products when bone ash comes in contact with aluminium-magnesium alloys. The amount of magnesium present in the alloy proved to have an effect on the different reaction products [92]. This could potentially be transferable to the reaction between the CFF phosphate binder and the molten aluminium.

Regardless of the mechanism behind the binder-aluminium reaction, Aubrey *et al.* [21] performed further immersion tests by varying the melt magnesium content, melt temperature, and immersion time. The experimental conditions were set to (i) a melt magnesium content equal to 1.01 wt.-% or 4.83 wt.-%, (ii) melt temperatures between 675 – 750 °C, and (iii) test durations between 30 and 120 minutes. Spent filters were analysed visually using a stereomicroscope with cross-polarized light, and reacted filters were identified by discolouration. Furthermore, an increase in magnesium/temperature/duration appeared to increase the amount of reacted area. Solem *et al.* [91] performed thermal tests on substrates made from the slurry used to produce phosphate bonded Al_2O_3-based CFFs in a vacuum induction furnace, both with and without contact with aluminium, and observed that phosphorus in the substrates diffused from the bulk to the surface, regardless of aluminium contact.

There is little reported on what effect the reactivity of the phosphate binder will have, but both the potential reaction products AlP and Mg_3P_2 have been reported to react with water or moisture in the air and form phosphine gas (PH_3) [21,92]:

$$AlP + 3H_2O \rightarrow PH_3(g) + Al(OH)_3 \tag{2.9}$$

$$Mg_3P_2 + 6H_2O \rightarrow 2PH_3(g) + 3Mg(OH)_2 \qquad (2.10)$$

$PH_3(g)$ is known as an extremely flammable gas (F+) [94] and has an autoignition temperature of 38 °C [95]. Furthermore, it is known to be very toxic (T+) and dangerous to the environment (N) [94].

Chemical stability of common ceramics in CFFs

As described in Chapter 2.3.1, examples of ceramics commonly applied in CFFs for molten aluminium filtration are Al_2O_3, SiO_2, SiC or combinations of these. The application of these ceramics is not limited to CFFs but can be used in other similar applications, *e.g.,* within the aluminium industry as refractories. In the context of such applications, these ceramics are more heavily studied compared to the limited available data in the area of CFFs. In the case of Al_2O_3-SiO_2 refractories applied in molten aluminium furnace bottoms and side walls, aluminium is known to penetrate pores as well as react with the refractory forming corundum (Al_2O_3) and dissolving silicon into the melt according to Equation (2.11) [96–98]:

$$4Al + 3SiO_2 \rightarrow 2Al_2O_3 + 3Si \qquad (2.11)$$

If magnesium is present, formation of spinel and dissolution of silicon according to Equation (2.12) is possible [98]:

$$Mg + 2Al + 2SiO_2 \rightarrow MgAl_2O_4 + 2Si \qquad (2.12)$$

Gibbs energy calculations for potential reactions show that SiO_2 and $3Al_2O_3{\cdot}2SiO_2$ (mullite) will be decomposed by aluminium if present, and the same for SiO_2 and Al_2O_3 with magnesium [98]. There are, however, other aspects that Gibbs energy calculations do not take into account, *e.g.,* the process kinetics, as well as other properties such as porosity, and it should be noted that if the oxides are part of larger compounds their reactivity may be changed [98]. Regarding SiC, it is well established that it can react with molten aluminium according to Equation (2.13) [99]:

$$4Al + 3SiC \rightarrow Al_4C_3 + 3Si \qquad (2.13)$$

The amount of silicon in molten aluminium may affect the reaction, but it has been reported that SiC reacts according to Equation (2.13) for melts with less than 10 wt.-% of silicon at 700 °C [100].

With these experiences from refractories and aluminium composites, one would expect the ceramics applied for CFFs to react with the aluminium melt. However, no literature reports that CFFs without a phosphate binder reacts with molten aluminium. Bao *et al.* [87] performed pilot-scale loop filtration trials with 15 tons of an aluminium-magnesium alloy (~ 1.00 wt.-% Mg and ~ 0.07 wt.-% Si) while using a filter consisting of 58-64 % SiC and 20 – 33 % SiO_2. The expected reactivity of the filter was investigated by measuring the amount of silicon dissolved in the melt by spectrographic analysis, as well as the number of Al_4C_3-particles by PoDFA, both before and after the filter. The analyses were, however, unable to detect any differences. Voigt *et al.* further performed both foundry-scale and continuous loop filtration trials with 2.3 kg [22] and 750 kg [23] of an AlSi7Mg0.3 alloy, respectively, for a series of oxidic filter surfaces (Al_2O_3, $MgAl_2O_4$, $3Al_2O_3{\cdot}2SiO_2$, TiO_2 and SiO_2 (only foundry-scale)). By analysis of the melt compositions, no indications of the filters contaminating the melts were observed for the foundry-scale filtration trials with low amounts of metal [22]. The filter surfaces of spent filters from the continuous loop filtration trials were analysed with electron microscopy (SEM, EDS, and EBSD), and no changes were observed for any of the filter surfaces except for the TiO_2 surface where single grains of $Al_2Na_2Ti_6O_{16}$ had formed [23].

2.5.2. Thermal stability of CFFs

As mentioned earlier, the thermal stability of CFFs is in the present project, defined as the filter's resistance to compression at elevated temperatures and while submerged in molten aluminium. Cold compression strength, *i.e.,* at room temperature, is then very important as a reference and baseline to the thermal stability. As there is very little data available in the literature on compression testing at elevated temperatures and in aluminium, a more thorough literature review of cold compression testing is given.

General cold compression of ceramic foams

Simplified and idealised descriptions of ceramic foam unit cells as described by Ashby [101] can be seen in Figure 2.12, both three- and two-dimensional in (a) and (b), respectively. Figure 2.12 (a) shows how a functional pore might be simplified with the thickness of the struts/walls defined as "t" and the pore dimensions (assuming square functional pores with equal height/width/depth) "l". Figure 2.12 (b) shows a two-dimensional presentation of functional pores when the force is applied perpendicular to the pores, as in compression, where the adjacent struts initially bend leading to bending fracture.

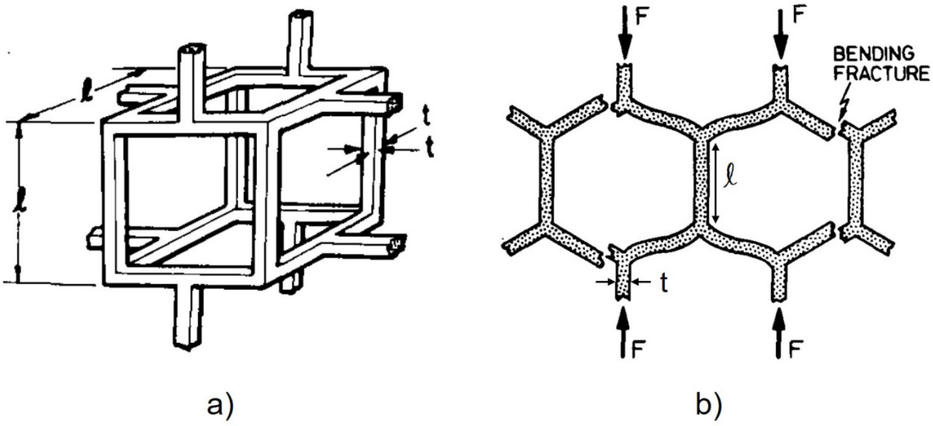

Figure 2.12: Descriptions of ceramic foam unit cells: (a) three-dimensional and (b) two-dimensional with bending fracture. Retrieved from Ashby [101] and reprinted with the permission of Springer Nature.

According to Ashby [101], the stress-strain curves of ceramic foams exhibit three different shapes or regions during compression: linear elasticity, collapse and densification. The linear elasticity region is described by the bending of the struts and occurs at low strains. The following region, collapse, is when a fracture occurs, and this appears as a plateau of almost constant stress in the stress-strain curves. The densification region occurs as the strain is further increased to where the functional pore walls crush together, leading to increased stress. The two first regions, linear elasticity and constant stress collapse, were also described experimentally by Meille *et al.* [102] through compression testing on foams produced using polyethylene (PE) spheres. However, for ceramic foams produced by the replica technique using PUR foams, like for CFFs, the experimental reports are different. Several scientists [103–106] have reported that the linear elasticity region is not completely linear in stress-strain curves, but rather that it is linear overall as a jagged curve with slight drops in stress caused by the failure of local struts without failure of the entire foam sample. The constant stress collapse region has also been reported differently by other scientists [104,105,107], see Figure 2.13, where the collapse is identified by a significant drop in stress so that the maximum applied stress before foam failure is shown as a sharp peak in the stress-strain curves. Voigt *et al.* [105] defined the overall foam failure as a drop in the applied stress (load) of 70 %, which was confirmed by observations post compression.

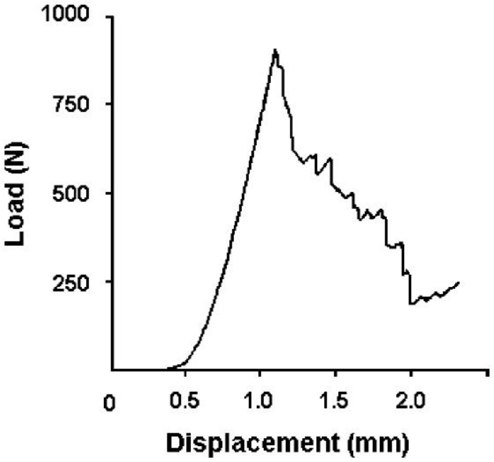

Figure 2.13: Example of a load-displacement curve of a ceramic foam, showing a significant drop in load (stress) after the peak value. Retrieved from Oliveira et al. [104], and reprinted with the permission of Elsevier.

According to Ashby [101], the most important part of describing the ceramic foam structure, and the parameter on which the mechanical properties above all else depend, is the relative density:

$$\rho_{rel} = \frac{\rho_{foam}}{\rho_{solid}} \approx \left(\frac{t}{l}\right)^2 \tag{2.14}$$

where ρ_{rel} is the relative density, ρ_{foam} the density of the whole foam, and ρ_{solid} the density of the solid in which the foam is made, *i.e.,* the density of the bulk material. t and l are, respectively, the thickness and length of the struts/walls, as seen in Figure 2.12. Ashby and Gibson [101,108] further described the relative density associated with the compression strength of ceramic foams:

$$\sigma_{fc} = C \cdot \sigma_{sc} \cdot \left(\frac{\rho_{foam}}{\rho_{solid}}\right)^{3/2} \tag{2.15}$$

where σ_{fc} is the foam compression strength, σ_{sc} the compression strength of the solid (bulk material) of which the foams are made, and C a constant. Equation (2.15) can be slightly revised based on different experimental studies, according to Oliveira *et al.* [104], where the exponent of the relative density varies in the range of 2.2 to 3.6. Regardless, from the equation it can be seen that the compression strength of the foam will increase with increasing relative densities. This has also been reported by many other scientists [102,103,107,109,110].

Ashby [101] further suggests the compression strength of foams to be insensitive to defects such as flaws, *e.g.,* from the production process, cracks in the microstructure, and significant variations in the pore size. Many scientists [104,107,110–112] have, however, questioned this statement, describing that such defects have a significant detrimental effect on both the compression strength and variability of the results. The considerable impact of defects on the compression strength has further been described to result in larger samples fracturing at less applied stress compared to smaller samples, simply because the probability of larger samples possessing pre-existing defects is higher [104,111]. Due to the production method, *e.g.*, where the sintering step leads to shrinkage of varying degrees dependent on composition, the final structure will necessarily consist of some flaws and cracks. Another aspect necessarily present, which is not specifically a flaw but something that separates CFFs from other foams, is the strut cavities formed due to the burn-off/vaporisation of the PUR foam, as described in Chapter 2.3.1. and in Figure 2.6. This is an aspect normally not included in mechanical models. Brezny *et al.* [112] did, however, propose a connection between the strength of separate struts and both their outer and inner (strut cavity) dimensions:

$$\sigma_{\text{sf}} = \frac{36 \cdot P \cdot L \cdot D}{(9 \cdot \pi \cdot D^4 - 16 \cdot b \cdot h^3)} \tag{2.16}$$

where σ_{sf} is the strut fracture strength, P the applied load at fracture, L the length of the strut, D the outside diameter of the strut, while b and h are the base and height of the strut cavities (which usually are triangular in shape).

Voigt *et al.* [105] performed an experimental study on how the compressive strength was affected by different parameters. It was shown that the compression strength was highly affected, implying that one should be careful directly comparing strength values between studies, except if the parameters and procedures are identical. Still, trends within each study can be compared as they should be more universal. There is no clear reported trend for the correlation between compression strength and pore size, *i.e.,* PPI in the case of CFFs, where higher PPI equals smaller functional pores. Oliveira *et al.* [104] described that an increase in compression strength due to a reduction in porosity is associated with a decrease in pore size, where an increase in porosity or pore size would decrease the compression strength. However, experimental results did not show an apparent decrease in compression strength for foams with larger pore sizes [104]. By further viewing experimental results from other publications, some scientists report that increasing pore sizes correlates to a decrease in compression strength [102,113], while other scientists report increasing compression strengths [107] or that there are small differences in compression strength without any specific trend [105].

CFF compression at elevated temperature and in aluminium melt

Despite the application of CFFs in the aluminium industry, which includes operation at elevated temperatures and in contact with molten aluminium, there is little, if anything, of relevance in published literature. The only relevant study was performed by Goretta *et al.* [109] and is an experimental study performed on ceramic foam samples of high purity Al_2O_3 (~ 99.1 wt.-% Al_2O_3) retrieved from a known filter producer. The samples were compression tested in air at room temperature, as well as every 100 °C starting at 800 °C and with 1500 °C as the highest temperature, where each sample was equilibrated at testing temperature for 30 minutes before compression. It was reported that a compression strength similar to room temperature was observed at 800 °C, an increase in compression strength at 900 °C, then similar to room temperature again in the interval 1000 – 1200 °C, with a decrease in compression strength for temperatures > 1200 °C [109]. The results were explained by the presence of an Al_2O_3 glassy phase which increased the strength at 900 °C due to initial glass softening that covered flaws within the ceramic structure. The decrease in strength with increasing temperatures was explained by a further glass softening that would decrease the viscosity of the glassy phase.

3. Materials and Methods

The experiments in the current study can be divided into three main parts, which will be presented in the following order: chemical stability trials, thermal stability trials, and pilot-scale loop filtration trials. However, an overview of the filters, aluminium melts, and characterisation methods will first be presented. Many of them are common for the different experiments and highlight how the experiments are connected.

3.1. Filters and aluminium melts

The CFFs tested in the present project were either received from commercial producers or produced using the replica method at TU Bergakademie Freiberg in Germany [89,90]. Some of the filters from commercial producers were manufactured utilising a phosphate binder, while others were not. The filters produced at TU Bergakademie Freiberg were, as mentioned in Chapter 2.4.2., made of pure sintered Al_2O_3 skeleton with a second coating layer consisting of either Al_2O_3 or a different surface chemistry (ceramic surface chemistries for all filters except for the carbon bonded filter, where the carbon surface chemistry was produced differently [114,115]). An overview of all the different filters used is given in Table 3.1, Table 3.2 and Table 3.3. A total of six different commercial filters and 7 different filters produced at TU Bergakademie Freiberg were tested. The details and the motivation for testing will be explained in Chapter 4.

Table 3.1: Overview of all the CFFs tested during the chemical stability trials.

Experimental Category	Experimental Details	Filter Surface	Filter Producer	Name/ Information
Chemical stability	Electromagnetic priming	Al_2O_3-based	Commercial	Filter A, phosphate bonded
		Al_2O_3	TU Freiberg	Filter B
		C-bonded Al_2O_3	TU Freiberg	Filter C
		$MgAl_2O_4$	TU Freiberg	Filter D
		TiO_2	TU Freiberg	Filter E
		$3Al_2O_3 \cdot 2SiO_2$	TU Freiberg	Filter F
	Gravity priming	Al_2O_3-based	Commercial	Filter A, phosphate bonded
		Al_2O_3	TU Freiberg	Filter B
		C-bonded Al_2O_3	TU Freiberg	Filter C
		$MgAl_2O_4$	TU Freiberg	Filter D
		TiO_2	TU Freiberg	Filter E
		$3Al_2O_3 \cdot 2SiO_2$	TU Freiberg	Filter F
		Al_2O_3 with increased roughness	TU Freiberg	Filter G
		Al_2O_3-based	Commercial	Filter H, phosphate bonded

Table 3.2: Overview of all the CFFs tested during the thermal stability trials.

Experimental Category	Experimental Details	Filter Surface	Filter Producer	Name/ Information
Thermal stability	At room- and elevated temperature	Al_2O_3-based	Commercial	Filter A, phosphate bonded
		Al_2O_3	TU Freiberg	Filter B
		Al_2O_3-based	Commercial	Filter H, phosphate bonded
		Al_2O_3-based	Commercial	Filter I
		Al_2O_3-based	Commercial	Filter J
		Al_2O_3-based	Commercial	Filter K
	Submerged in molten aluminium	Al_2O_3-based	Commercial	Filter A, phosphate bonded
		Al_2O_3	TU Freiberg	Filter B
		Al_2O_3-based	Commercial	Filter H, phosphate bonded
		Al_2O_3-based	Commercial	Filter I
		Al_2O_3-based	Commercial	Filter J

Table 3.3: Overview of all the CFFs tested during the pilot-scale loop filtration trials.

Experimental Category	Filter Surface	Filter Producer	Name/ Information
Filtration trials	Al_2O_3	TU Freiberg	Filter B
	C-bonded Al_2O_3	TU Freiberg	Filter C
	Al_2O_3 with increased roughness	TU Freiberg	Filter G
	Al_2O_3-based	Commercial	Filter I
	Al_2O_3-based	Commercial	Filter K
	Al_2O_3 with increased roughness 2	TU Freiberg	Filter L

The aluminium melts used for the different experimental procedures are presented in Table 3.4. The values in the table are the intended compositions, where magnesium is the main alloying element and variable between the different trials. The detailed chemical composition of the melts as measured is presented in the respective publications. From Table 3.4 it can be seen that the combination of pure aluminium and melts with ~ 2.2 wt.-% magnesium is repeated between the experimental categories (except for the filtration trials where an alloy with an intermediate magnesium concentration was applied at ~ 0.9 wt.-%). It can also be seen that the melts at the laboratory scale were made either by additions of magnesium or by mixing different ingots.

Table 3.4: The intended composition of the used aluminium melts for the different experiments, focusing on aluminium and magnesium. n/a indicates that there is no additional information.

Experimental Category	Experimental Details	Aluminium Melts	Melt Origin
Chemical stability	Electromagnetic priming	Pure aluminium (~99.8 wt.-%)	Pure aluminium ingots
		Aluminium-magnesium alloy (~2.2 wt.-% Mg)	Pure aluminium ingots with additions of Mg
	Gravity priming	Pure aluminium (~99.7 wt.-%)	Pure aluminium ingots
		Aluminium-magnesium alloy (~2.2 wt.-% Mg)	Mixing of pure aluminium and 5182 ingots
Thermal stability	N/A	Pure aluminium (~99.8 wt.-%)	Pure aluminium ingots
		Aluminium-magnesium alloy (~2.2 wt.-% Mg)	Pure aluminium ingots with additions of Mg
Filtration trials	N/A	6082 alloy with extra magnesium (~ 0.9 wt.-% Mg)	Pilot-scale furnace operations

3.2. Material characterisation methods

This section briefly summarises the different sample and material characterisation techniques applied during the current study, as well as the experimental parameters used.

Light optical microscopy (LOM)

Two different light optical microscopes (LOM) with associated image software were applied in the current study, *i.e.,* a Leica MEF4M [116] connected to the ProgRes® CapturePro software [117] and a Zeiss Axio Vert.A1 [118] connected to the ZEN core software [119]. The LOM was applied for imaging, where a polarised light and a teal colour filter or a light wavelength adjuster were used for a clearer image and to analyse if the colour changes observed were real.

Scanning electron microscopy (SEM)

A Zeiss Ultra 55 Limited Edition field emission scanning electron microscope (FE-SEM) [120] was applied for the secondary electron (SE) and backscatter electron (BSE) imaging, as well as associated composition analyses. The working distance was 10 mm and the accelerating voltages applied were in the range of 10 – 20 kV.

Energy dispersive X-ray spectrometry (EDS)

An XFlash Detector 4010 energy-dispersive X-ray spectrometer [121] associated with the FE-SEM was applied for chemical composition point and area analyses, as well as composition mappings.

Electron probe microanalysis (EPMA)

A JEOL JXA-8500F electron probe micro analyser (EPMA) [122] was applied to investigate the presence of elements as composition mappings (Al, O, P, C, Si, Mg, Ti, Fe, K, B) at areas of interest identified previously using LOM, as well as some random areas. The analyses were performed on areas of ~ 1 x 1 mm^2 with a probe current of 30 nA.

Transmission electron microscopy (TEM)

A Helios G4 UX Dual-beam focused ion beam scanning electron microscope (FIB-SEM) [123] was used to cut out a thin lamella from the metal-filter interface of a filter. Initial coarse thinning of the lamella was performed with $Ga+$ ions at an accelerating voltage of 30 kV, while for the finer thinning the accelerating voltage was reduced to 5 and 2 kV. The transmission electron microscopy (TEM) [124] was performed using a JEOL ARM 200FC with a double Cs aberration corrected cold field emission gun (FEG), connected to a Centurio energy dispersive X-ray spectrometer (EDS) and a Quantum ER GIF electron loss spectrometer (EELS). The FEG was operated at an accelerating voltage of 200 kV.

Optical emission spectroscopy (OES)

An ARL 4460 spark optical emission spectrometer (SOES) [125] was applied to analyse the chemical composition of the aluminium melts. For analysis, disc samples (~ 50 mm diameter and 9 mm thickness) were cast using a copper chill mould. The analysis was performed at the R&D centre of Hydro Aluminium in Sunndalsøra, Norway.

3.3. Chemical stability experimental procedure

The chemical stability trials were performed using two separate experimental procedures, identified by their priming sequence. The procedure with the electromagnetic priming was performed at the laboratory of the Department of Materials Science and Engineering at NTNU, while the gravity priming procedure was performed at the R&D facility of the SELEE Corporation in Hendersonville, North Carolina, USA.

3.3.1. With electromagnetic priming

A resistance furnace (muffle furnace) and Salamander Super A8 crucibles were used for the trials, where the inside surface of the crucibles was coated with boron nitride (BN) before each trial. Approximately 2.2 kg of aluminium was melted to a temperature of 730 °C for each trial. Argon gas (5N) was applied on the top of the melt surface to reduce oxidation of the melt at a flow rate of 2 standard litres per minute (SLPM).

Cubic filters of 5 x 5 x 5 cm^3 were used, and one filter was tested per crucible per trial. The priming procedure was performed by placing the crucible in an electromagnetic coil made of copper tubes, as the combined illustration and picture of the experimental setup presented in Figure 3.1 shows. The filter was preheated in a resistance furnace at 600 °C with subsequent immersion of the filter into the melt while applying an electromagnetic field measured to 80.0 mT in the centre of the coil. The electromagnetic field was applied for 20 – 35 seconds (although priming was observed to occur instantly), and the crucible containing the submerged filter sample was returned to the resistance furnace for the rest of the trial.

The total duration of the trial (after priming) was 120 minutes. Immediately after priming and thereafter every 30 minutes, the aluminium melt was sampled for chemical composition analysis using a ladle coated with BN and a copper chill mould. Before each sampling, the melt was skimmed, and the submerged filter was moved around within the melt. After the last metal sample at the trial end, *i.e.,* after 120 minutes, the filter was removed from the melt and left to cool at ambient temperature in air. After 30 minutes of cooling, a phosphine gas (PH_3) indicating Dräger-Tube® [126] was applied to measure any PH_3 gas emissions.

3.3.2. With gravity priming

A customised resistance furnace setup, applied with an automated temperature control system, was used for the gravity priming trials. Noltina Stabil crucibles were filled with 41 kg of aluminium, which was melted and kept at a temperature of 730 °C. Due to the high metal amount, the same melt was used for three sequential trials. The trials were performed in atmospheric conditions, inevitably leading to some oxidation of the aluminium-magnesium alloy. Thus, 1 – 3 kg of aluminium-magnesium alloy ingots were added between trials to keep the magnesium concentration constant.

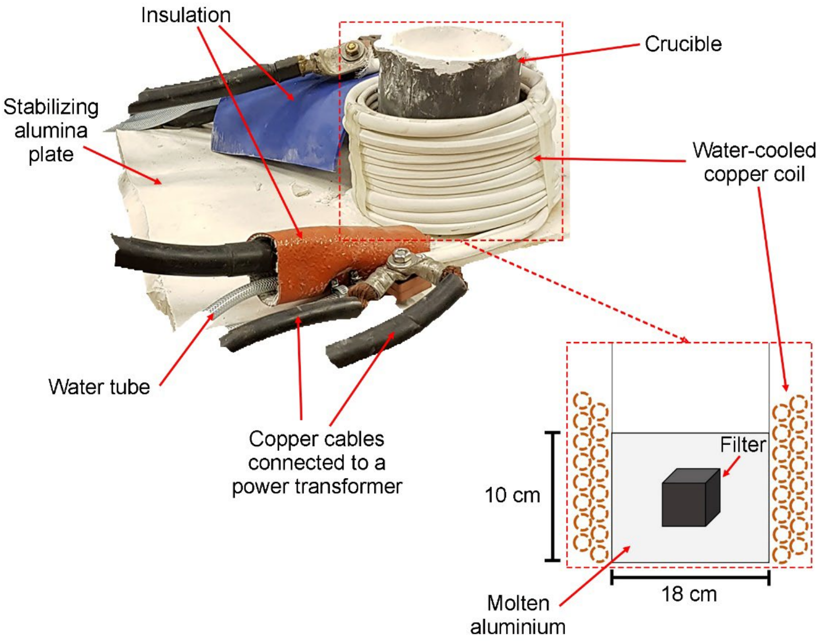

Figure 3.1: Chemical stability trials with electromagnetic priming. The picture shows how priming was performed, and the sketch of the position of the filter during the tests. Retrieved from Bergin et al. [59], which was published under the Creative Commons Attribution 4.0 International License: https://creativecommons.org/licenses/by/4.0/.

Cylindrical filter samples with a height of 5 cm and a diameter of 4 cm were tested, whereby four filters were tested simultaneously in each trial. The filters were placed in individual tubes of fused silica, as seen in the overview of the experimental setup in Figure 3.2. Filters were fastened with the use of inert Ca-Al-B glass. The silica tubes were coated with BN at the bottom, approximately at the same height as the filters. An air velocity burner was used for filter preheating to temperatures in the range of 708 – 840 °C, where the filter tubes were placed in a vent system to avoid direct heating. The preheated filter tubes were fastened to the lower end of the setup rod, see Figure 3.2. Filter priming was achieved by the gravity head of the aluminium, similar to conventional priming, where the filters upon submersion were subjected to a metallostatic pressure high enough to force the metal into the pores. The filter tubes in which the filters were fastened enabled air to vent out from the filters. The rod holding the filter tubes was further fastened to a rotating wheel at the top of the setup, which, while rotating, would move the rod and thus the filters up and down in the molten aluminium. This movement simulated the filtration step with melt flow through the filter functional pores and, simultaneously, caused a slow stirring of the melt. The reciprocating up and down movement was comparable to industrial melt flows at a calculated flow rate of 14.11 kg/(cm^2 · hour) per filter. This was based on the pace and height of the vertical movement (24.2 seconds for the filters to go down 20 cm and up again) and with the assumption that the entire filter volume was aluminium, leading to a flow rate of 0.049 kg/second which was divided by the filter inlet area of 12.57 cm^2.

The filter tubes were fastened in such a way that they could be removed separately, and thus the test duration varied between 30, 60, 90 and 120 minutes. The aluminium melt was sampled at time zero and thereafter every 30 minutes, and melt skimming was performed before each sampling. Upon filter tube removal, each tube was initially placed on a chill plate to reduce metal drainage, while further cooling was performed in air.

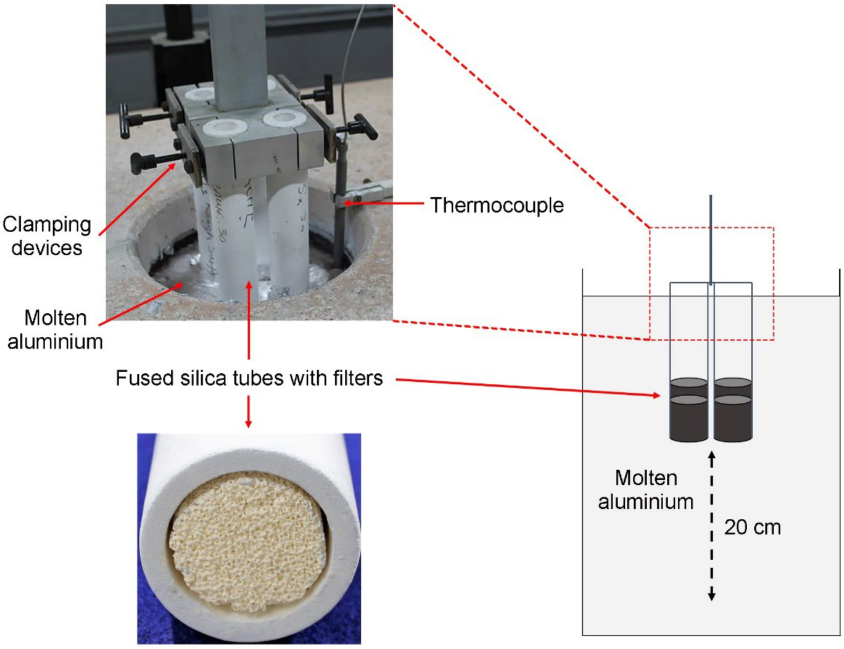

Figure 3.2: The gravity priming experimental setup for the chemical stability trials. The sketch shows the overall setup, while the pictures show how the filters were seated in the test tubes and further fastened to the rod moving up and down. Retrieved from Bergin et al. [59], which was published under the Creative Commons Attribution 4.0 International License: https://creativecommons.org/licenses/by/4.0/.

3.3.3. Analysis of data

All filters, both as received and from both experimental procedures, were cut, embedded in epoxy, polished and analysed visually in LOM and SEM. Selected areas of interest were further analysed in EPMA. All samples from the aluminium melt were analysed in OES. The melt-filter interface of one filter from the experimental procedure with gravity priming was analysed in TEM. Potential release and amount of PH_3-gas were measured using Dräger-Tubes® from all filters post-trial in the experimental procedure with electromagnetic priming.

3.4. Thermal stability experimental procedure

3.4.1. Compression at room- and elevated temperature

CFFs with a thickness of 5 cm were cut either into cylindrical samples with a diameter of 5 cm using a diamond bit core drill with applied water for cooling, or into cubic samples with a width and depth of 5 cm using a water jet. In both cases, the samples were dried overnight at 100 °C. The dry samples were weighed, and the outer dimensions of the samples were measured using a calliper, and thus the overall foam density was calculated. An MTS 880 Hydraulic Tensile Testing Machine [127] with pistons having a diameter of 5 cm was used for the compression testing, where the compression speed was 2 mm/min. A picture and an illustration of the dry compression testing (both at room and elevated temperatures) can be seen in Figure 3.3.

One of the filter types was subjected to more extensive compression testing at room temperature. This included testing both cylindrical and cubic samples of filters with a PPI of 30, 65 and 80. For all other filter types, only cylindrical samples with a PPI of 30 were tested. In addition to the initial testing, repetition trials were performed on different batches of all the filter types to get an indication of the quality consistency of the filter types tested in the present project.

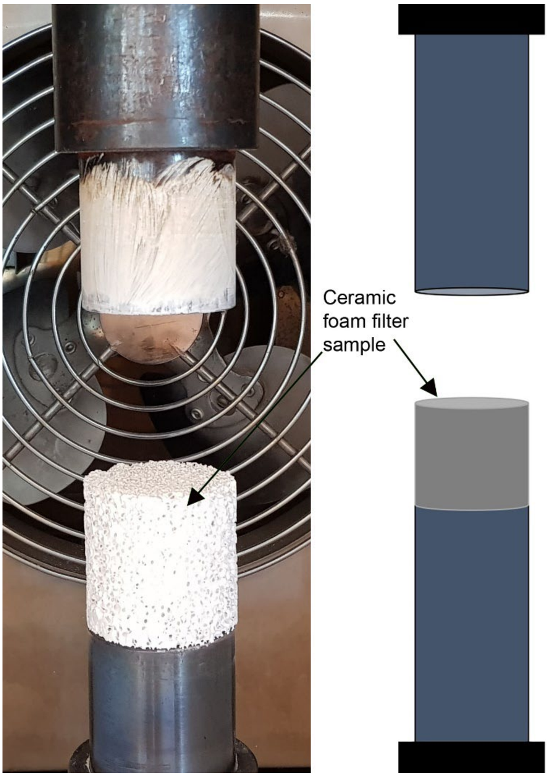

Figure 3.3: The dry compression testing setup for cylindrical filter samples, i.e., compression testing at room- and elevated temperatures. Retrieved from Bergin et al. [128].

For the compression strength testing at elevated temperatures, the cylindrical filter samples were preheated in a resistance furnace at 800 °C for different heating durations. The actual compression step of the testing at elevated temperatures was performed like the compression tests at room temperature and is presented in Figure 3.3. Before compression testing, the temperature development within the filter samples, and thus the filter temperature during heating and compression, was measured on a series of dummy samples. These dummy samples were prepared as seen in Figure 3.4, with a K-type thermocouple pierced into the filter for continuous temperature monitoring. The tests revealed that the filter sample temperature reached 800 °C after ~ 8 minutes and that the temperature dropped to ~ 730 °C at compression. Thus, the temperature of the filter samples at compression is comparable to the operating temperatures of CFFs. The parameters and number of tests for the dry compression testing, *i.e.,* at room- and elevated temperatures, can be seen in Table 3.5.

Figure 3.4: An example of how the dummy samples were prepared by inserting a thermocouple to record the temperature development within the filter samples.

Table 3.5: Overview of the parameters and number of samples (repetition trials not included) for compression testing at room- and elevated temperatures. n/a indicates that the cells are not applicable for the current row and column.

Parameter	**Room Temperature Testing**	**Testing at Elevated Temperatures**	
Heating temperature	n/a	800 °C	800 °C
Duration of heating	n/a	10 minutes	2 hours
Testing temperature	~ 25 °C	~ 730 °C	~ 730 °C
Number of samples tested	22	10	10

3.4.2. Compression in molten aluminium

There are two requirements to enable the compression testing of filter samples submerged in molten aluminium. One is a container that can hold the molten aluminium and where compression can occur, and the other is priming the filter so that the filter actually can be submerged in the melt. Priming was achieved by applying an electromagnetic coil as was described for the chemical stability trials in Chapter 3.3.1, but of a different size resulting in an electromagnetic field of 20 mT measured in the centre of the coil. The filter samples, which all were 30 PPI and cut into the same cylindrical shape as during dry testing, were submerged into ~ 550 grams of melt. The electromagnetic field was applied for 5 minutes, and solidification of the aluminium with a filter sample immersed within occurred seconds after the electromagnetic field was removed. Figure 3.5 (a) shows a picture of a solidified sample. A container was specifically designed for the compression testing, consisting of welded steel with a groove at the bottom to fit on the bottom piston in the compression apparatus. The inside of the container was lined with MASTIC 85 refractory ceramic fibres [129] (Pyrotek® Inc., USA) and coated with BN, as shown in Figure 3.5 (b), where a photograph of the container filled with a primed and solidified sample can be seen. The container and sample, as shown in Figure 3.5 (b), were placed in a resistance furnace at 750 °C until the aluminium was molten and the temperature reached, see Figure 3.5 (c).

Figure 3.5: Photographs showing critical parts of the compression testing setup of filter samples submerged in molten aluminium: (a) a solidified metal sample with a primed filter sample submerged within, (b) a metal sample placed in the prepared container, and (c) melting of the metal sample in a resistance furnace before compression testing.

Once the molten aluminium reached the test temperature the melt surface was skimmed, and the container was placed in the compression apparatus, as seen in Figure 3.6. The compression speed was equal to that of the dry testing at 2 mm/min. In addition to the actual compression testing with a filter sample, reference compression tests were also performed on the aluminium melt only, *i.e.,* without a submerged filter sample.

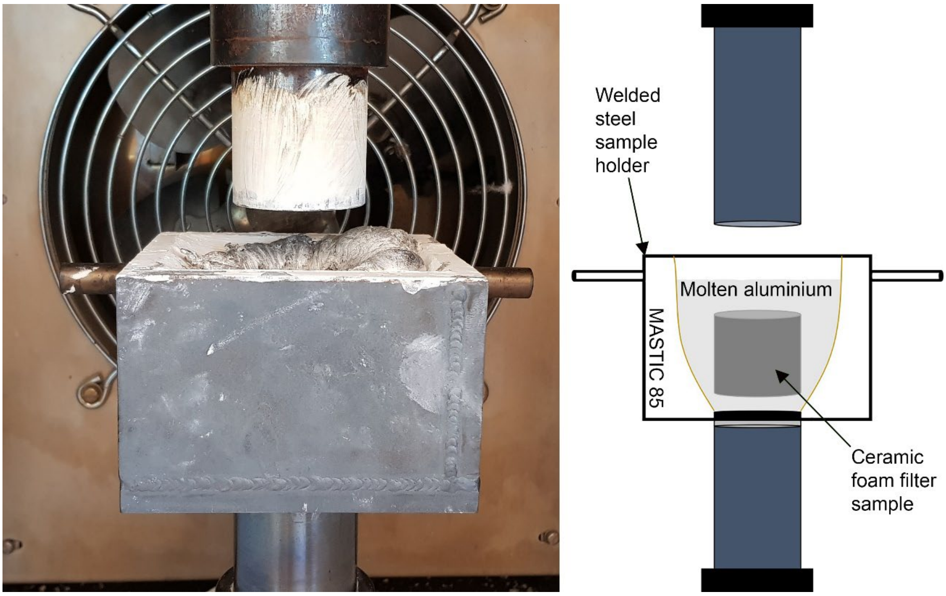

Figure 3.6: Compression testing procedure for a filter sample submerged in molten aluminium, with the custom-made steel container filled with MASTIC 85. Retrieved from Bergin et al. [128].

3.4.3. Analysis of data

All as received filters were cut, embedded in epoxy, and polished, with subsequent visual analysis in SEM, as well as compositional analysis with EDS. The produced load-displacement curves were analysed in terms of the slope before the maximum load, and the maximum load was used to calculate the compression strength according to Equation (3.1):

$$\Sigma_{\mathrm{fc}} = \frac{F_{max}}{A} \tag{3.1}$$

where σ_{fc} is the compression strength, F_{max} the maximum load, and A the loaded area.

3.5. Pilot scale loop filtration experimental procedure

3.5.1. Outline and experimental parameters

All CFFs were of 30 PPI with a thickness varying in the range of 47 – 50 mm. Due to limitations during the production in view of the maximum size of the filters, all were produced as symmetric trapeziums of ~ 178 x 178 mm^2 at the larger side/inlet and ~ 150 x 150 mm^2 at the smallest side/outlet. To achieve sufficient flow in the launder loop and avoid stagnation, four filters of the same filter type were applied in parallel per trial, as seen in Figure 3.7, with a ceramic filter adapter cross in between. A total of 10 trials over 5 days were performed, with two trials per day.

The trials were performed at the Hydro Aluminium R&D facility in Sunndalsøra, Norway, where an overview of the experimental setup can be seen in Figure 3.7. As seen from the figure, the experimental setup consists of a large casting furnace which, for the current trials, was filled with 8 tons of electrolysis metal and alloying elements to produce the alloy (6082 with extra magnesium). Each day, a new melt was prepared so that two consecutive trials were performed using the same melt.

The experimental setup further consists of a launder system connected in a loop so that, with the help of a mechanical metal pump, the metal leaves the furnace on one side and enters again on the other. The filter box applied was a DFF® box, where its principle is described in Chapter 2.3.2. Red numbers in Figure 3.7 represent the positions for melt quality analysis and the additions made to the melt, where 1 and 4 indicate LiMCA II [26] measurements, 2 and 3 sampling of metal for PoDFA [27] analysis, while 5 indicates the position for additions into the melt over the trial duration. Two different additions were made, of which one was the addition of 4 kg of compacted aluminium saw chips every 10 minutes for each trial to keep a steady amount of incoming inclusions at the filter inlet. During one of the trials, 67 kg of saw chips were added towards the end to see the effect of heavy additions on the melt quality and the filtration process. The other addition at point 5 was grain refiner additions (AlTi5B1) with the purpose of observing its effect on the filtration process. The grain refiner addition was made at the second trial each day and for the second half of those trials, *i.e.,* after approximately 40 minutes of filtration without grain refiner additions. The addition was performed continuously at a rate of 1 kg/ton of aluminium, given a melt flow rate of 10 ton/h in the launder. The total duration of each trial varied slightly. Still, in general, the first trial each day (no grain refiner) lasted about 40 minutes, while the second trial (with grain refiner) lasted about 80 minutes.

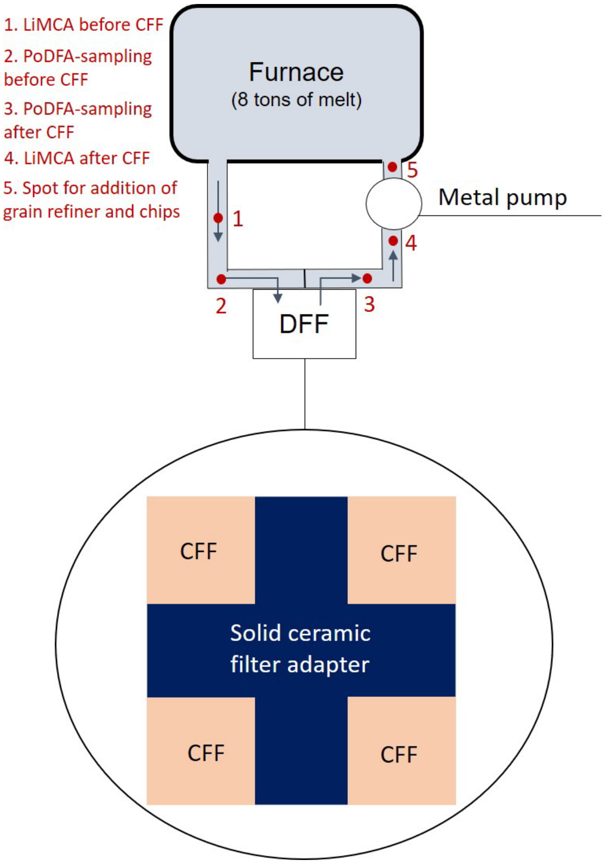

Figure 3.7: An overview of the experimental setup for the pilot-scale loop filtration trials, including the (i) furnace filled with 8 tons of melt, (ii) loop and its sampling- and addition points, (iii) metal pump, and (iv) DFF® filter box with a filter adapter. Retrieved from Bergin et al. [130], and reprinted with the permission of Springer Nature.

3.5.2. Analysis of data

During the trials, both the temperature of the melt in the launder, as well as the pressure drop over the filter box, were continuously measured. The LiMCAs were also constantly measuring, and the data were analysed in detail afterwards. Six PoDFA sampling sequences were performed in each trial (one sample before and after the filter during each sequence), and the samples were subsequently analysed using the AMCA method (described in Chapter 2.4.2.). The melt flow rate was calculated by inserting a refractory dam into the launder at the end of most trials. The dam had a hole of a known diameter, forcing the metal flow in the launder through that hole. Lasers were then used to measure the pressure drop (formed due to the reduced area of flow) over the dam. Lastly, all spent filters were cut and visually inspected before being embedded in epoxy, polished, and analysed visually in LOM and SEM, as well as compositionally with EDS.

3.6. Thermodynamic calculations

3.6.1. HSC Chemistry®

The Reaction Equations module of HSC Chemistry® 9.9.2.3 [131] was applied to calculate the Gibbs free energy (ΔG) as a function of temperature for several different reactions. An example of this is the formation of $PH_{3(g)}$ from AlP and Mg_3P_2 in contact with H_2O, as well as the reaction between phosphorus and other common elements present in aluminium, *e.g.,* magnesium.

3.6.2. FactSage™

The Equilib module and the Predom module of FactSage™ 7.3 [132] were applied with the databases FactPS, FToxid and FTlite. In both cases, the software uses Gibbs free energy minimisation, where it is assumed that equilibrium exists between all phases and that reaction kinetics are neglectable. Both modules were run with input variables replicating the chemical stability experimental procedure with electromagnetic priming (described in Chapter 3.3.1.), *i.e.,* with additions of a phosphate bonded Al_2O_3-based CFF into an aluminium-magnesium-alloy at 730 °C, in an open system with added argon-gas to hinder oxidation. The Equilib module served as input to the Predom module, where a predominance diagram of the Al-Mg-P-O system at 727 °C was created, with the partial pressures of $O_2(g)$ and $P_2(g)$ on each axis.

4. Summary of Papers and Results

This chapter presents the most relevant results and conclusions of the present project on the topics of chemical stability (Part I), thermal stability (Part II), and filtration performance (Part III). It is a summary of the published work, added as supplements, as well as results that have not been published.

4.1. Part I: Chemical stability of CFFs in molten aluminium

Two papers were published or submitted for publication on CFF chemical stability upon filter contact with molten aluminium.

4.1.1. Paper 1: Experimental Study on the Chemical Stability of Phosphate Bonded Al_2O_3-based Ceramic Foam Filters (CFFs)

Introduction

In relation to Paper 1, the described chemical stability experimental procedures were used to test two commercial phosphate bonded filters and six new and innovative sintered filters. The testing included submersion of filters in pure aluminium melts (~ 99.5 wt.-% Al) and an aluminium-magnesium alloy (~ 2.2 wt.-% Mg) at 730 °C, with analysis of melt compositions as a function of time, as well as spent filter investigations using various microscopy techniques. Measurements of PH_3 gas emissions from spent filters were also performed.

Results and conclusions

The obtained results showed that filters produced with a phosphate binder reacted with magnesium in the melt. This filter degradation was accompanied by discolouring of the filter from bright white to brown and further to black for what was believed to be a severely reacted filter. EPMA analysis of areas with a mix of white and discoloured filter, as well as OES analysis of samples retrieved from the melt, revealed that magnesium diffused from the melt and into the discoloured areas of the filter. In contrast, the same areas were depleted of phosphorus, leading to an increased phosphorus content in the melt. It was shown that an increase in exposure time and magnesium concentration led to a more severe filter degradation. In the worst case, pieces of the filter struts were observed to fracture, potentially contaminating the melt. Even though a high magnesium concentration led to a more severe filter degradation, TEM analysis revealed that the phosphate binder reacted with magnesium even at a very low concentration (0.00035 wt.-% Mg).

According to the thermodynamic calculations, the likely mechanism behind this filter degradation is the formation of AlP and $MgAl_2O_4$ (spinel) from the $AlPO_4$ binding phase, however, this was not proven. Measurements of phosphine gas formation (PH_3(g)) using Dräger-Tubes® revealed PH_3 only for the phosphate bonded filter submerged in the aluminium-magnesium alloy. The average amount of PH_3 gas was measured to be 3.3 ppm, significantly higher than NIOSH's recommended exposure limits [133] of 0.3 (TWA[1]) and 1.0 (STEL[2]) ppm.

---

[1] TWA (Time-Weighted Average) is described as the average exposure over an 8-hour period, *i.e.,* a working day.

[2] STEL (Short-Term Exposure Limit) is described as the average exposure over a period of 15 minutes.

Neither of the new and innovative sintered filters showed any signs of being reactive with either of the aluminium melts. Furthermore, none of the filters was observed to emit PH_3 gas. It was observed however, that some of the filters had defects in their coating, *i.e.,* in the applied second layer, which in most cases was a ceramic layer sintered to the Al_2O_3-base. This can be seen in Figure 4.1 and Figure 4.2, which show areas with no coating or cracks in the coating. This applied to the filter surface chemistries of TiO_2, $3Al_2O_3 \cdot 2SiO_2$ and $MgAl_2O_4$. It is important to note that the origin of these defects is unknown, and they may be from the production step or the image preparation procedures such as cutting and/or polishing. Still, the mentioned filters were not included in the later study on the filtration performance.

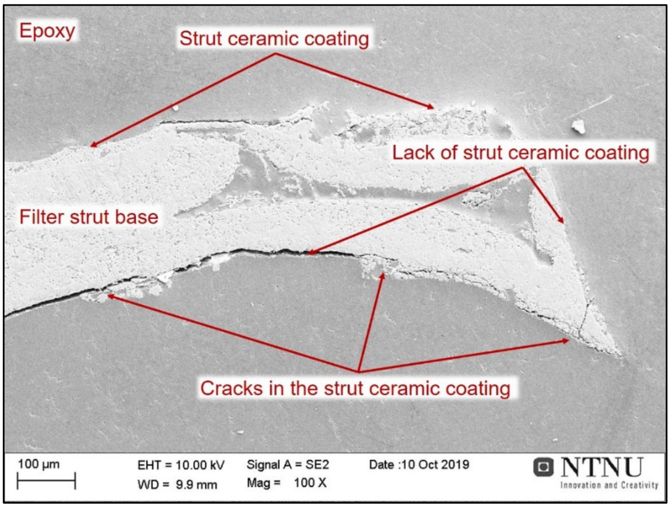

Figure 4.1: SEM micrograph showing an example of ceramic coating defects for the $3Al_2O_3 \cdot 2SiO_2$ surface chemistry on the Al_2O_3 strut base. The filter was cut and mounted in epoxy and not subjected to any testing.

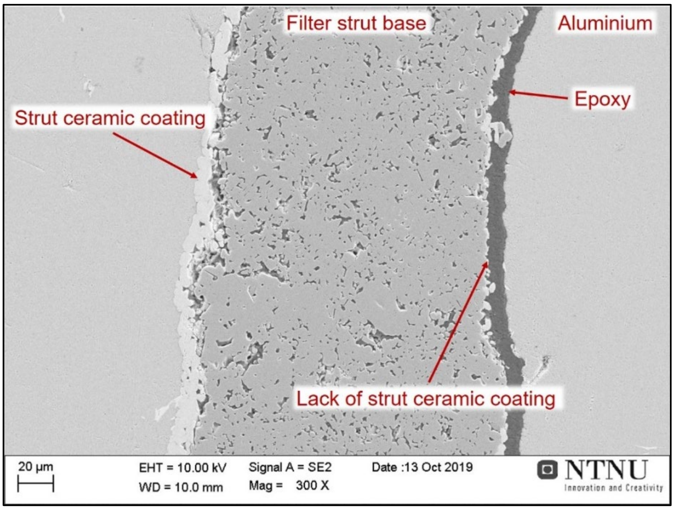

Figure 4.2: SEM micrograph showing an example of ceramic coating defects for the TiO_2 surface chemistry on the Al_2O_3 strut base. The filter was tested in the gravity priming procedure in the aluminium-magnesium alloy for a test duration of 120 min.

The effect of wetting between the molten aluminium and the filter substrate is expected to play a significant role in view of the filtration performance. Due to that, numerous studies [24,86,88,134–138] have been performed where wetting trials using a sessile drop technique have been compared to results from filtration trials in an attempt to correlate the wetting with the filtration performance. These reported wetting trials have been performed with different procedures, where the goal often has been to remove the oxide layer as much as possible to achieve an aluminium-filter substrate interface. This has been justified by the assumption that there is aluminium-filter contact during filtration. However, this has not been proven, and given that the filter pores (including microporosity) are filled with air before filtration and that the necessary oxygen partial pressure for aluminium oxide formation is very low ($1.01325 \cdot 10^{-44}$ Pa at 700 °C [136]), it could be a bold assumption. Figure 4.3 shows a TEM-image of the interface between a filter (an alumina grain) and the aluminium, retrieved from the bulk of a spent filter from the presently performed chemical stability gravity priming experimental procedure. In this particular area, there is an aluminium-filter interface, *i.e.,* no aluminium oxide layer between the filter and the aluminium. This supports using wetting trials for filtration performance studies, given the absence of an oxide layer. Still, it is essential to note that the area shown in Figure 4.3 is not necessarily representative of the whole filter.

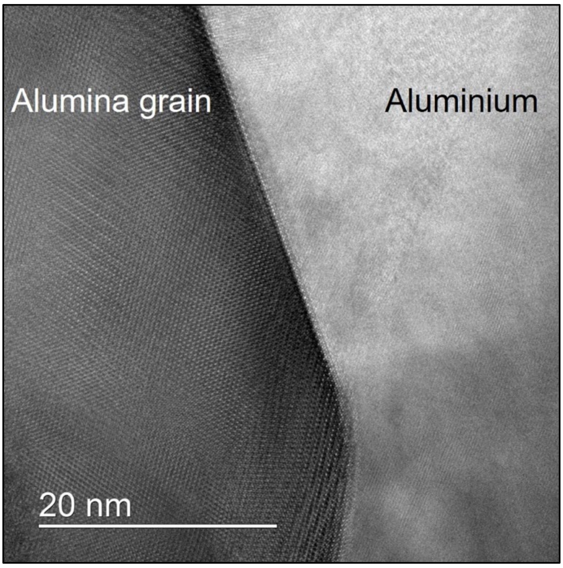

Figure 4.3: High-resolution bright field TEM-image of the interface between an alumina grain in a spent CFF and the aluminium. The analysed area, retrieved using a FIB-SEM, was taken from the bulk of a commercially produced CFF (Filter A) exposed in the gravity priming setup to pure aluminium (Al99.5).

Limitations and further work

The main limitation of the present work on the chemical stability of the filters is that the mechanism behind the degradation of the phosphate binder was only estimated by thermodynamic calculations and not determined experimentally. This also applies to the formation of the PH_3 gas, where it would be interesting to accurately determine the gas composition and to measure the total amount of PH_3(g) that potentially could emit from a reacted filter.

For further work, it would also be interesting to investigate what effect the filter degradation of the phosphate bonded filters would have on the mechanical strength of the filters. Additional further work would be performing filtration tests on the new and innovative filters deemed most promising.

4.1.2. Paper 2: Silicon Depletion from Ceramic Foam Filters (CFFs) during Aluminium Melt Filtration in a Pilot-Scale Setup

Introduction

CFFs can, as previously mentioned, consist of several different ceramics whereby silica (SiO_2) sintered together with other ceramics is one of several common compositions. At the same time, SiO_2-based refractories are expected to react with the aluminium melt. Paper 2 presents observations on spent filters after pilot-scale loop filtration trials using 8 tons of a 6082 alloy (with extra additions of Mg), where the filter consisted of Al_2O_3 and SiO_2 sintered together.

Results and conclusions

The spent filter analysis with the use of LOM revealed that the filters were partly discoloured, from bright white as produced to a mix of black and white areas, which correlated with the absence of silicon for the black areas. It was therefore concluded that silicon depletion from the filters and into the melt had occurred during trials.

Limitations and further work

There was a variation in results between two nearly identical tests. The difference in reacted area between the two filters was significant. For the most reacted filter it was estimated that ~ 58 % of the total filter area was reacted, in contrast to ~ 3 % for the least reacted filter. Further work would include repetition of experiments, lab-scale experiments replicating the conditions of the initial experiments, and TEM-analysis of spent filters.

4.2. Part II: Thermal stability of CFFs in air and molten aluminium

Two papers were published or submitted for publication on CFF thermal stability in air and while submerged in molten aluminium. In addition to the published results and conclusions, additional results that have not been published are presented.

4.2.1. Paper 3: Compression Testing of Ceramic Foam Filters (CFFs) Submerged in Aluminium at Operating Temperature

Introduction

The compression strength and the change in strength as an effect of temperature are essential properties for filter integrity during use in a casthouse, and thus also for the filter suitability and filtration performance. Paper 3 describes developed procedures for compression testing of filter samples at elevated temperatures in air and while submerged in aluminium, with initial results.

Results and conclusions

The compression testing at elevated temperatures was done at ~ 730 °C. This is similar to the temperature at operating conditions both during filter preheating and filtration, as well as identical to the temperature of the chemical stability immersion tests. For the compression of filter samples submerged in molten aluminium, a sample container was constructed out of welded steel and filled with refractory fibres. The load-displacement curves revealed a shape similar to that of testing in air. Compared with room temperature testing, the results showed a decrease in compression strength for heating durations longer than 10 minutes and a further decrease for testing in molten aluminium.

Compression testing was performed on filter samples of different shapes and PPIs. It can be seen from Figure 4.4 that the effect of sample shape is inconclusive, where the compression strength is equal at 30 PPI while it partly decreases for the two other PPIs (there is some overlapping of the standard deviations). It was concluded that neither of the sample shapes was preferential but that all testing should be performed with the same sample shape, *i.e.,* cylindrical (same dimensions as pistons). It can further be seen that the effect of PPI on the compression strength is inconclusive, which is in accordance with literature as described in Chapter 2.5.2. For both cubic and cylindrical samples the compression strength is highest for 65 PPI, while for 30 PPI and 80 PPI, the difference in strength is dependent on the shape. The effect of PPI on the compression strength at room temperature was also investigated on a few other filter types, supporting this behaviour. As a result, all further compression testing was performed on 30 PPI filters.

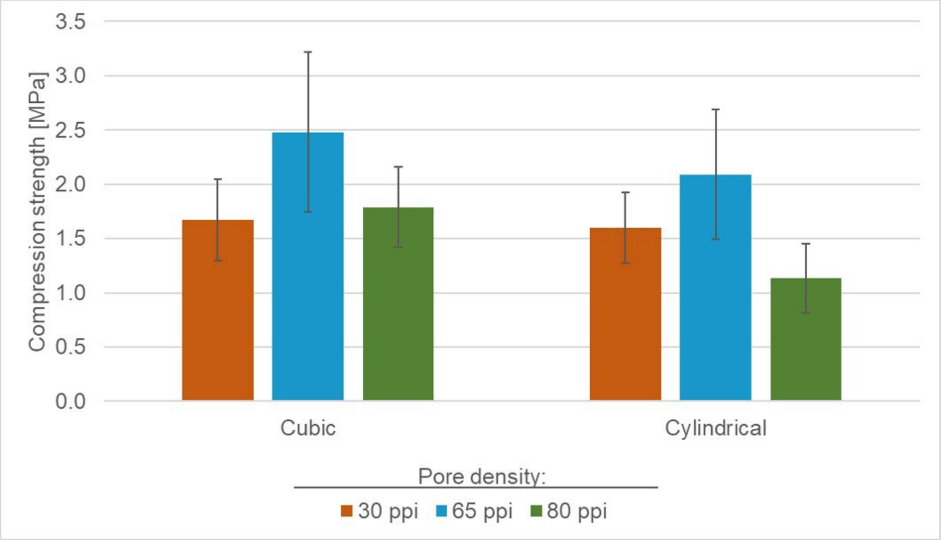

Figure 4.4: The effect of sample shape and PPI on the compression strength and standard deviations at room temperature, where all tests were performed on the same CFF type. The cubic filter samples had dimensions of 5 x 5 x 5 cm^3, while the cylindrical filter samples had a height and diameter of 5 cm.

Limitations and further work

The procedure for the compression in aluminium is performed in two steps, where the filter sample initially is primed and then solidified in the aluminium before being remelted for the compression testing. The filter sample will then be subjected to solidification shrinkage, which likely will affect its overall strength. However, it is difficult to know how significant the impact is. Another aspect affecting the measured strength is the cutting of the filter samples from a larger filter, which may induce microscopic cracks or damage to the samples. Additionally, the CFFs are produced with thicker struts at the edges, and thus, filter samples cut from the bulk are likely to have lower strength. As further work, it would be interesting to apply the newly developed procedures for a range of different CFFs, to investigate how the compression strength of the different filters will be affected by elevated temperatures and contact with liquid aluminium. It would also be interesting to test the effect of different melt compositions.

4.2.2. Paper 4: Investigation of Mechanical and Thermo-Mechanical Strength of Ceramic Foam Filters (CFFs)

Introduction

In relation to Paper 4, the developed compression testing procedures were applied to six different filter types, *i.e.,* five commercial filter types and one new and innovative filter. Only one of the new and innovative filters was compression tested due to the time-consuming production and testing steps. In addition, it was assumed that the strength of these filters would be comparable, as all were made with the same sintered Al_2O_3-skeleton. Two different melt compositions were used (pure aluminium and an aluminium-magnesium alloy), and the filter submersion time was 5 minutes.

Results and conclusions

The obtained results were, to a large degree, in accordance with the results of one filter presented in Paper 3, but there were some variances between the different filters. At room temperature, the average compression strengths for the different CFFs were in the range of 1.19 – 5.19 MPa, where the new and innovative filter had the highest strength. The commercial filters possessed a significantly lower compression strength. There was, with few exceptions, a decrease in compression strength as an effect of elevated temperature for all filters. This decrease was in the range of 9 – 59 % as compared to room temperature. An example of the decrease in compression strength with elevated temperatures can be seen in Figure 4.5 for the new and innovative filter.

For compression testing of filter samples submerged in molten aluminium, there was a decrease in compression strength as compared to room temperature for all filters, where Figure 4.6 shows the strengths for all filter types in aluminium. No difference in compression strength between the two melt compositions can be seen. However, it is still possible that the previously described filter degradation (Paper 1) affects compression strength for longer melt-filter contact durations. The reduction in compression strength from room temperature testing to testing in molten aluminium varied in the range of 43 – 69 %.

One of the commercial filters tested in dry conditions was not tested submerged in aluminium due to a large spread in compression strength during the repetition trials.

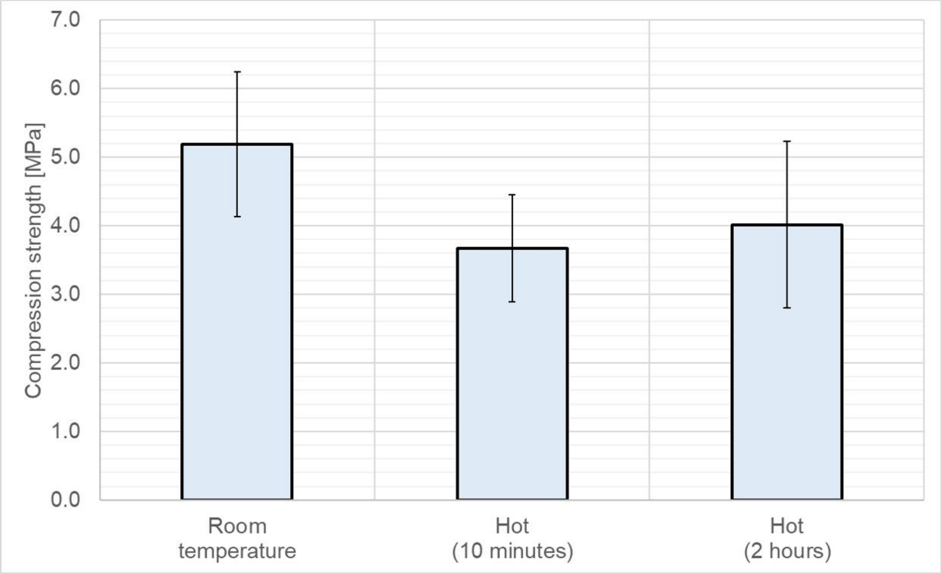

Figure 4.5: Average compression strengths with accompanying standard deviations at room- and elevated temperature, with heating durations of 10 minutes and 2 hours, for the new and innovative filter (Filter B).

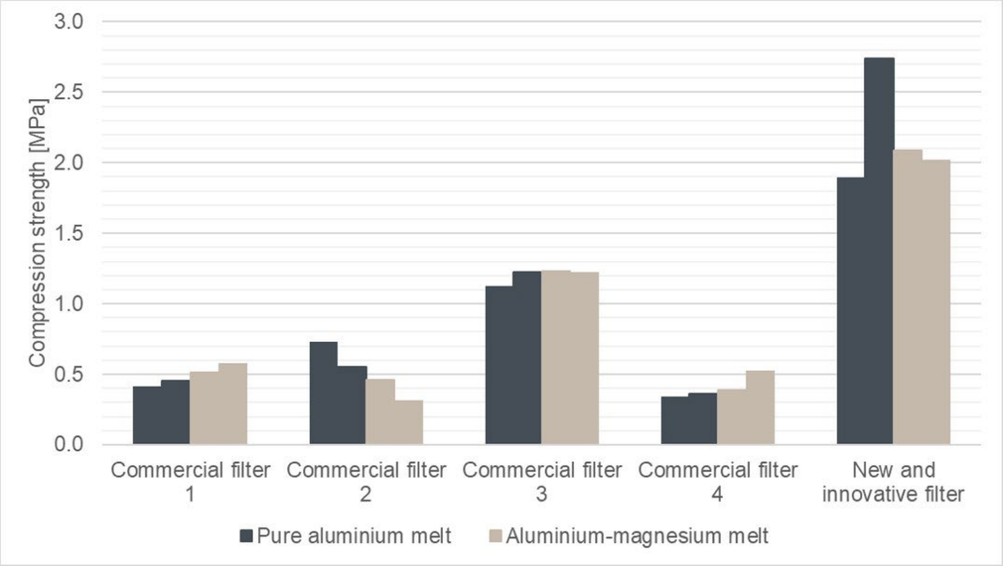

Figure 4.6: Compression strengths of all CFF types tested in pure aluminium and the aluminium-magnesium alloy.

The explanation behind the observed decreasing compression strengths, as well as the few exceptions where there was no change, is presently not known. Two possible effects are thermal shock, occurring when the filter samples are placed in and retrieved from the hot furnace, and softening of the ceramic structure, as described in the literature [109]. At present there is, however, no evidence for either. The effect of thermal shock is undisputed, but the significance of the effect is unknown, and it does not appear to be the full explanation based on the variation in the results.

Limitations and further work

For longer submersion times, it would be interesting to study the effect of the filter degradation of phosphate bonded filters on the compression strength. Also, improvements to the procedure for testing at elevated temperatures would be interesting, either by eliminating thermal shock induced or by determining the significance of the thermal shock.

4.3. Part III: Filtration performance of CFFs in a pilot-scale setup

Paper 5 presents the results from the pilot-scale filtration trials. In addition, two papers [139,140] based wholly or partly on results from the same trials were published, however, these will not be described here and are not added as supplements either.

4.3.1. Paper 5: Performance of Regular and Modified Ceramic Foam Filters (CFFs) during Aluminium Melt Filtration in a Pilot-Scale Setup

Introduction

In Paper 5, the results from the pilot-scale loop filtration trials were presented, where the filtration performance of the most promising filters identified during Part I and Part II of the present project was assessed. This included both new and innovative filters, as well as commercial filters, the latter partly as references. The pilot-scale trials were performed with 8 tons of a 6082-alloy (with extra additions of magnesium, ~ 0.9 wt.-% Mg) based on electrolysis metal, as well as additions of AlTi5B1-grain refiner in some of the trials.

There was an intention to include a commercial phosphate bonded filter to see the effect of the filter degradation on the filtration performance and thereby enabling a comparison of those results with the reference filters tested under identical conditions. Unfortunately, there was a production error at the supplier, and therefore this was not possible.

Results and conclusions

Continuous LiMCA- and pressure drop measurements over the filter with lasers, PoDFA analysis, as well as analysis of spent filters using LOM and SEM all revealed that the melts used for the trials were fairly clean, *i.e.,* with low amounts of inclusions. However, in both the PoDFA- and the spent filter analysis, common inclusions such as Al_2O_3-films (including aluminium-magnesium films), MgO, $MgAl_2O_4$ and TiB_2 were identified in small amounts. The performance of all the different filters was similar, with no significant differences. The total average removal efficiencies for the presented trials were in the range of 85 – 93 %, which is in the upper region of what is expected for 30 PPI filters. A significant decrease in the removal efficiency upon grain refiner addition was observed, however, without any signs of inclusion/oxide “bridges” in any of the spent filters (regardless of any grain refiner additions), questioning the often-suggested mechanism for the decreasing filtration efficiency with grain refiner additions.

Limitations and further work

As further work, it would be interesting to perform additional experiments, *e.g.,* in a different setup, to verify the present results.

5. Concluding Remarks

The aim of the present work has been to investigate the suitability and performance of new and innovative CFFs in light of the known limitations of the currently used filters. This was performed through lab-scale testing of the chemical stability (immersion in molten aluminium) and thermal stability (compression testing at elevated temperatures and in molten aluminium) of both commercial and newly designed CFFs, as well as pilot-scale filtration trials with the most promising CFFs based on the stability trials.

CFFs produced with a phosphate binder were observed to be reactive in contact with aluminium melts containing magnesium, which is in contrast to sintered filters without a binder. This filter degradation resulted in magnesium and phosphorous diffusion to and from the filter, respectively, with an increasing extent for increasing magnesium concentrations. The phenomena were also observed at very low concentrations of magnesium (0.00035 wt.-% Mg). Furthermore, the degraded filter was observed to react with the humidity in the air during cooling, releasing phosphine gas ($PH_3(g)$) exceeding recommended exposure concentrations. A similar observation, *i.e.,* filter degradation, was made on a spent sintered alumina filter with SiO_2, showing indications of silicon depletion.

The compression strength of the CFFs was, with three exceptions, significantly lower after exposure to elevated temperature compared to room temperature. A further decrease in compression strength, in the range of 43 – 69 %, was observed for filter samples submerged in molten aluminium. At the current melt-filter submersion time of 5 minutes, the melt composition had no significant influence on the compression strength. Thus, the strength was not affected by the magnesium-induced filter degradation during this short exposure time.

Based on the chemical- and thermal stability trials, as well as previously reported data, the most promising CFFs to be tested in the pilot-scale filtration campaign proved to be the Al_2O_3 filters with increased roughness and the carbon bonded Al_2O_3, which were compared to both commercial and non-commercial references. However, no significant difference in filtration performance was observed for any of the filters, which is believed to be a direct result of the operational conditions during these trials.

6. Further Work

The chemical reactivity of phosphate bonded CFFs has been established in the present study. Also, indications of reactivity of SiO_2-based CFFs have been seen and discussed. There are, however, some unanswered questions relating to the effect of filter degradation on the compression strength and the overall filtration performance. Compression tests on phosphate bonded filters with longer durations of melt submersion, as well as filtration trials using two LiMCA units to test the effect of phosphate binder (*e.g.,* different amounts of binder) on filtration performance, would therefore be of interest. It appears, however, that phosphate bonded filters, with time, will be completely phased out. Thus, chemical stability trials on newly developed filters would, based on this, be needed to secure the safety of the operators, as well as the quality of the final product.

Although the thermal stability tests performed in the present work are believed to be valid and representative for the potential stresses the filters are subjected to during use, there is room for improvement. For the dry testing at elevated temperatures, upgrades in the experimental setup and the procedure to either isolate, quantify, and/or remove the effect of thermal shock would be a convincing way to demonstrate the compression benefits of one filter type over another, *i.e.,* chemical composition, porosity, and design. This could, *e.g.*, be achieved by controlled heating of the filter samples and performing the compression without changing the temperature. For testing of filters submerged in molten aluminium, the step of solidifying the primed filter sample with subsequent remelting should be avoided, which could be achieved by performing the priming step and the compression step in the same laboratory or, even better, in the same experimental setup (which unfortunately was not possible during the present work).

6.1. Future perspective on a global level

Since the year 2000, the production of aluminium has increased by more than 100%, and its demand is rising steadily [7]. At the same time the increase in recycling is substantial, and by 2050 it is expected that most of the increase in the aluminium demand will be covered by a 50/50-ratio of primary- and recycled aluminium [7]. As the supply of aluminium to society then with time will be kept up by recycling, the limiting factors may become the scrap availability and price of energy.

In view of this, the global perspective of aluminium filtration is that the need for a cleaner metal will increase at the same time as the input material will change and be less clean, putting a higher demand on the filtration technology. Improvements in the CFF technology have the opportunity to revolutionise the industry by continuing to be a simple and cost-efficient method, but with possibilities for a significantly increased filtration efficiency. More research is therefore needed on the CFF fundamentals, *i.e.*, the actual conditions within the filter during filtration, and how the different filtration mechanisms and surface properties of the filter (*e.g.,* chemistry, structural morphology, flow characteristics) are affected by different operating parameters. With an improved knowledge of these topics, CFFs can be designed and improved accordingly. Other research topics of interest, likely with a relatively more modest improvement in filtration performance, could be the industrial application of multistage and/or reverse filtration. However, despite the clear potential of CFFs, the increasing demand for cleanliness might also be a challenge in regards to competition.

References

[1] UC Rusal, The History of Aluminium Industry, (n.d.). https://www.aluminiumleader.com/history/industry_history/ (accessed January 3, 2022).

[2] Copper Development Association Inc., History of Copper, (2022). https://www.copper.org/education/history/ (accessed January 3, 2022).

[3] J. Nutting, Steel: History, (2019). https://www.britannica.com/technology/steel/History (accessed January 3, 2022).

[4] D.G. Altenpohl, Aluminum: Technology, Applications, and Environment. A Profile of a Modern Metal, Sixth Edit, The Aluminum Association, Inc., Washington D.C., 1998.

[5] thyssenkrupp Materials (UK) Ltd, Melting Point of Aluminium, (2018). https://www.thyssenkrupp-materials.co.uk/melting-point-of-aluminium (accessed January 3, 2022).

[6] The International Aluminium Institute, Statistics - Primary Aluminium Production, (2021). https://international-aluminium.org/statistics/primary-aluminium-production/ (accessed January 3, 2022).

[7] The International Aluminium Institute, IAI Material Flow Model - 2021 Update, (2021). https://international-aluminium.org/resource/iai-material-flow-model-2021-update/ (accessed November 2, 2021).

[8] B.E. Hixson, C. Dube, D.D. Smith, The Influence of Melt Charge Materials on Molten Metal Quality at JW Aluminum, Light Metals. (2015) 983–986.

[9] T. Abel Engh, Principles of Metal Refining, Oxford University Press Inc., New York, 1992.

[10] L.J. Gauckler, M.M. Waeber, C. Conti, M. Jacob-Dulière, Industrial Application of Open Pore Ceramic Foam for Molten Metal Filtration, Light Metals. (1985) 251–262.

[11] J. Campbell, Castings, 2nd ed., Elsevier Butterworth-Heinemann, Oxford, 2003.

[12] C. Conti, P. Netter, Deep Filtration of Liquid Metals: Application of a Simplified Model Based on the Limiting Trajectory Method, Separations Technology. 2 (1992) 46–56.

[13] B. Friedrich, C. Kräutlein, K. Krone, Melt Treatment of Copper and Aluminium - The Complex Step Before Casting, in: Proceedings of The International Conference on Continous Casting of Non-Ferrous Metals, Wiley-Vch, DGM, 2006.

[14] C.E. Eckert, R.E. Miller, D. Apelian, R. Mutharasan, Molten Aluminum Filtration: Fundamentals and Models, Light Metals. (1984) 1281–1304.

[15] D. Apelian, R. Mutharasan, Filtration: A Melt Refining Method, JOM. 32 (1980) 14–19.

[16] L.A. Strom, J.W. Black, R.I.L. Guthrie, C. Tian, Non-Ferrous Alloy Filtration Efficiency Study of Fully Sintered Reticulated Ceramics Utilizing LiMCA and LAIS, Light Metals. (1992) 1093–1100.

[17] N.J. Keegan, W. Schneider, H.-P. Krug, V. Dopp, Evaluation of the Efficiency of Ceramic Foam and Bonded Particle Cartridge Filtration Systems, Light Metals. (1997).

[18] D.D. Smith, L.S. Aubrey, W.C. Miller, LiMCA II Evaluation of the Performance Characteristics of Single Element and Staged Ceramic Foam Filtration, Light Metals. (1998) 893–916.

[19] S. Instone, M. Badowski, W. Schneider, Development of Molten Metal Filtration Technology for Aluminium, Light Metals. (2005) 933–938.

[20] N.J. Keegan, W. Schneider, H.-P. Krug, Evaluation of the Efficiency of Fine Pore Ceramic Foam Filters, Light Metals. (1999) 1031–1040.

[21] L.S. Aubrey, R. Olson, D.D. Smith, Development of a Phosphate - Free Reticulated Foam Filter Material for Aluminium Cast Houses, Materials Science Forum. 630 (2009) 137–146.

[22] C. Voigt, B. Fankhänel, E. Jäckel, C.G. Aneziris, M. Stelter, J. Hubálková, Effect of the Filter Surface Chemistry on the Filtration of Aluminum, Metallurgical and Materials Transactions B. 46 (2015) 1066–1072. https://doi.org/10.1007/s11663-014-0232-7.

[23] C. Voigt, E. Jäckel, F. Taina, T. Zienert, A. Salomon, G. Wolf, C.G. Aneziris, P. Le Brun, Filtration Efficiency of Functionalized Ceramic Foam Filters for Aluminum Melt Filtration, Metallurgical and Materials Transactions B. 48 (2017) 497–505. https://doi.org/10.1007/s11663-016-0869-5.

[24] C. Voigt, J. Hubálková, T. Zienert, B. Fankhänel, M. Stelter, A. Charitos, C.G. Aneziris, Aluminum Melt Filtration with Carbon Bonded Alumina Filters, Materials. 13 (2020) 1–13. https://doi.org/10.3390/ma13183962.

[25] C. Voigt, B. Dietrich, M. Badowski, M. Gorshunova, G. Wolf, C.G. Aneziris, Impact of the Filter Roughness on the Filtration Efficiency for Aluminum Melt Filtration, Light Metals. (2019) 1063–1069. https://doi.org/10.1007/978-3-030-05864-7_130.

[26] ABB, Mobile Liquid Aluminium Cleanliness Analyzer, LiMCA III, (2021). https://new.abb.com/products/measurement-products/analytical/metallurgical-analyzers/limca-iii (accessed November 29, 2021).

[27] ABB, Inclusion Identification and Quantification Analysis, PoDFA, (2021). https://new.abb.com/products/measurement-products/analytical/metallurgical-analyzers/podfa (accessed November 29, 2021).

[28] N.N. Greenwood, A. Earnshaw, Chemistry of the Elements, 2nd ed., Butterworth-Heinemann, 1997.

[29] Norsk Hydro ASA, Karmøy Technology Pilot, (2021). https://www.hydro.com/en/media/on-the-agenda/karmoy/ (accessed October 22, 2021).

[30] A. Kvithyld, A. Nordmark, D. Dispinar, S. Ghaderi, K. Lapointe, Quality Comparison between Molten Metal from Remelted Sheets; Mill Finish and Coated, Light Metals. (2012) 1031–1035.

[31] V. Kevorkijan, Challenges and Advantages of Recycling Wrought Aluminium Alloys from Lower Grades of Metallurgically Clean Scrap, Materiali in Technologije/Materials and Technology. 47 (2013) 13–23.

[32] The International Aluminium Institute, Sustainability, (2018). https://recycling.world-aluminium.org/review/sustainability/ (accessed November 2, 2021).

[33] M. Bertram, Monday Stats Post, International Aluminium Institute. (2021). https://international-aluminium.org/resource/aluminium-recycling-fact-sheet-2/ (accessed November 2, 2021).

[34] M.A. Dewan, M.A. Rhamdhani, J.B. Mitchell, C.J. Davidson, G.A. Brooks, M. Easton, J.F. Grandfield, Control and Removal of Impurities from Al Melts: A Review, Materials Science Forum. 693 (2011) 149–160. https://doi.org/https://doi.org/10.4028/www.scientific.net/msf.693.149.

[35] S.S.S. Kumari, R.M. Pillai, B.C. Pai, Role of Calcium in Aluminium Based Alloys and Composites, International Materials Reviews. 50 (2005) 216–238. https://doi.org/10.1179/174328005X14366.

[36] A. Abd El-Aty, Y. Xu, X. Guo, S.H. Zhang, Y. Ma, D. Chen, Strengthening Mechanisms, Deformation Behavior, and Anisotropic Mechanical Properties of Al-Li alloys: A Review, Journal of Advanced Research. 10 (2018) 49–67. https://doi.org/10.1016/j.jare.2017.12.004.

[37] J. Campbell, Entrainment Defects, Materials Science and Technology. 22 (2006) 127–145. https://doi.org/10.1179/174328406X74248.

[38] M. Di Sabatino, L. Arnberg, S. Rørvik, A. Prestmo, The Influence of Oxide Inclusions on the Fluidity of Al-7 wt.%Si Alloy, Materials Science and Engineering A. 413–414 (2005) 272–276. https://doi.org/10.1016/j.msea.2005.08.175.

[39] X. Dai, X. Yang, J. Campbell, J. Wood, Effects of Runner System Design on the Mechanical Strength of Al-7Si-Mg Alloy Castings, Materials Science and Engineering A. 354 (2003) 315–325. https://doi.org/10.1016/S0921-5093(03)00021-2.

[40] G. Eisaabadi Bozchaloei, N. Varahram, P. Davami, S.K. Kim, Effect of Oxide Bifilms on the Mechanical Properties of Cast Al-7Si-0.3Mg Alloy and the Roll of Runner Height after Filter on their Formation, Materials Science and Engineering A. 548 (2012) 99–105. https://doi.org/10.1016/j.msea.2012.03.097.

[41] G.E. Totten, D.S. MacKenzie, eds., Handbook of Aluminum: Volume 1: Physical Metallurgy and Processes, CRC Press, 2003.

[42] D.D. Smith, K.R. Butcher, L.S. Aubrey, Selee Corp Tackles Liquid Salts in Molten Aluminium, Aluminium International Today. 12 (2000).

[43] D. Apelian, R. Mutharasan, C.A. Romanowski, Commercially Available Porous Media for Molten Metal Treatment: A Property Evaluation, Light Metals. (1982) 935–968.

[44] P. Netter, C. Conti, Efficiency of Industrial Filters for Molten Metal Treatment Evaluation of a Filtration Process Model, in: Essential Readings in Light Metals: Volume 3 Cast Shop for Aluminum Production, 2016: pp. 271–284.

[45] J.P. Desmoulins, H. D'Hondt, J.M. Hicter, P. Netter, Which Filter What Plant? The Pechiney Research Approach, Light Metals. (1989) 757–767.

[46] The Free Library: American Foundry Society Inc., History of Ceramic Foam Filtration. (Aluminum Silver Anniversary Paper)., Modern Casting. (2003). https://www.thefreelibrary.com/History+of+Ceramic+Foam+Filtration.+(Aluminum+Silver+Anniversary...-a0103795701 (accessed November 12, 2021).

[47] H. Duval, C. Rivière, É. Laé, P. Le Brun, J.-B. Guillot, Pilot-Scale Investigation of Liquid Aluminum Filtration through Ceramic Foam Filters: Comparison between Coulter Counter Measurements and Metallographic Analysis of Spent Filters, Metallurgical and Materials Transactions B. 40B (2009) 233–246.

[48] Pyrotek Inc., SIVEX Ceramic Foam Filters, (2021). https://www.pyrotek.com/products/casthouse/show/ProductLine/sivex-ceramic-foam-filters (accessed November 13, 2021).

[49] K. Schwartzwalder, H. Somers, A. V. Somers, Method of Making Porous Ceramic Articles, US 3,090,094, 1963.

[50] M. V. Twigg, J.T. Richardson, Fundamentals and Applications of Structured Ceramic Foam Catalysts, Industrial & Engineering Chemistry Research. 46 (2007) 4166–4177.

[51] M.J. Pryor, T.J. Gray, Ceramic Foam Filter, US 3,947,363, 1976.

[52] J.C. Yarwood, J.E. Dore, R.K. Preuss, Ceramic Foam Filter, US 3,962,081, 1976.

[53] J.W. Brockmeyer, Ceramic Foam Filter, US 4,343,704, 1982.

[54] A.N. Leonov, M.M. Dechko, Theory of Design of Foam Ceramic Filters for Cleaning Molten Metals, Refractories and Industrial Ceramics. 40 (1999) 537–542.

[55] A. Nishikawa, Technology of Monolithic Refractories, in: Plibrico Japan Company Limited, Tokyo, Japan, 1984.

[56] A.S. Wagh, Chemically Bonded Phosphate Ceramics - Twenty-First Century Materials with Diverse Applications, in: 2nd ed., Elsevier, 2016: pp. 141–142.

[57] M. Scheffler, P. Colombo, eds., Cellular Ceramics: Structure, Manufacturing, Properties and Applications, John Wiley & Sons, 2006.

[58] Pyrotek Inc., 565 Sivex Application Guidelines E4 - For Sivex Ceramic Foam Filtration Systems, (n.d.). https://www.pyrotek.com/DeliverFile/e8949c2cdcf637e617f6ea2fcdb28d09 (accessed November 13, 2021).

[59] A. Bergin, C. Voigt, R. Fritzsch, S. Akhtar, L. Arnberg, C.G. Aneziris, R.E. Aune, Experimental Study on the Chemical Stability of Phosphate Bonded Al2O3-based Ceramic

Foam Filters (CFFs), Metallurgical and Materials Transactions B 2021. March (2021) 2008–2025. https://doi.org/https://doi.org/10.1007/s11663-021-02144-3.

[60] J.E. Dore, A Practical Guide on How to Optimize Ceramic Foam Filter Performance, Light Metals. (1990) 791–796.

[61] F. Breton, P. Waite, P. Robichaud, Advanced Compact Filtration (ACF): An Efficient and Flexible Filtration Process, Light Metals. (2013) 967–972.

[62] F. Caron, J.-F. Desmeules, Dynaprime Filtration Technology Experience at Alcoa Baie-Comeau, Light Metals. (2020) 972–980.

[63] M.W. Kennedy, S. Akhtar, R. Fritzsch, J.A. Bakken, R.E. Aune, Apparatus and Method for Priming a Molten Metal Filter, US9605332B2, 2017.

[64] M.W. Kennedy, Removal of Inclusions from Liquid Aluminium using Electromagnetically Modified Filtration, Norwegian University of Science and Technology, 2012.

[65] R. Fritzsch, Electromagnetically Enhanced Priming of Ceramic Foam Filters, Norwegian University of Science and Technology, 2016.

[66] U. Tundal, I.K. Steen, T. Haugen, J.O. Fagerlie, Apparatus and Method for the Removal of Unwanted Inclusions from Metal Melts. WO 2016/126165 A1, WO 2016/126165 A1, 2016.

[67] S. Bao, M. Syvertsen, F. Syvertsen, B.E. Gihleengen, U. Tundal, T. Pettersen, Laboratory Scale Study of Reverse Priming in Aluminium Filtration, Light Metals. (2019) 1105–1111.

[68] U. Tundal, I.K. Steen, Å. Strømsvåg, T. Haugen, J.O. Fagerlie, A. Håkonsen, Drain Free Filtration (DFF) - A New CFF Technology, Light Metals. (2019) 1097–1104.

[69] F.A. Acosta G., A.H. Castillejos E., A Mathematical Model of Aluminum Depth Filtration with Ceramic Foam Filters: Part I. Validation for Short-Term Filtration, Metallurgical and Materials Transactions B. 31B (2000) 491–502.

[70] E. Laé, H. Duval, C. Rivière, P. le Brun, J.-B. Guillot, Experimental and Numerical Study of Ceramic Foam Filtration, Light Metals. (2006) 285–290.

[71] S. Ray, B. Milligan, N. Keegan, Measurement of Filtration Performance, Filtration Theory and Practical Applications of Ceramic Foam Filters, in: Aluminium Cast House Technology, 2005: pp. 1–12.

[72] D.C. Chesonis, A Holistic Approach to Molten Metal Cleanliness, Light Metals. (2017) 1411–1418.

[73] F. Frisvold, Filtration of Aluminium: Theory, Mechanisms, and Experiments, Norwegian University of Science and Engineering, 1990.

[74] S. Bao, Filtration of Aluminium - Experiments, Wetting, and Modelling, Norwegian University of Science and Technology, 2011.

[75] M. Syvertsen, I. Johansen, A. Kvithyld, S. Bao, U. Eriksen, B.E. Gihleengen, S. Akhtar, A. Bergin, A. Johansson, Evaluation of CFF and BPF in Pilot Scale Filtration Tests, Light Metals. (2020) 963–971.

[76] D.A. Doutre, B. Gariépy, J.P. Martin, G. Dubé, Aluminum Cleanliness Monitoring: Methods and Applications in Process Development and Quality Control, Light Metals. (1985) 296–304.

[77] C. Dupuis, F. Dallaire, B. Maltais, The Measurement of Controlled Size Particles in Molten Aluminum Using the LiMCA II Technique, Light Metals. (1999) 1069–1082.

[78] M. Badowski, R. Schmoll, A Comparison of Cold and Hot PoDFA Procedure for Particle Monitoring in Liquid Aluminium, Light Metals. (2016) 837–842.

[79] H. Zedel, R. Fritzsch, S. Akhtar, R.E. Aune, Estimation of Aluminum Melt Filtration Efficiency Using Automated Image Acquisition and Processing, Light Metals. (2019) 1113–1120.

[80] H. Zedel, R. Fritzsch, S. Akhtar, R.E. Aune, Automated Metal Cleanliness Analyzer (AMCA) - An Alternative Assessment of Metal Cleanliness in Aluminum Melts, Light Metals. (2021) 778–784.

[81] L.N.W. Damoah, L. Zhang, Removal of Inclusions from Aluminum through Filtration, Metallurgical and Materials Transactions B: Process Metallurgy and Materials Processing Science. 41 (2010) 886–907. https://doi.org/10.1007/s11663-010-9367-3.

[82] C. Dupuis, R. Dumont, The Impact of LiMCA Technology on the Optimization of Metal Cleanliness, Light Metals. (1993) 997–1002.

[83] N. Towsey, W. Schneider, H.-P. Krug, A. Hardman, N. Keegan, The Influence of Grain Refiners on the Efficiency of Ceramic Foam Filters, Light Metals. (2001) 291–295.

[84] N. Towsey, W. Schneider, H.-P. Krug, The Effects of Rod Grain Refiners with Differing Ti/B Ratio on Ceramic Foam Filtration, Light Metals. (2002) 931–936.

[85] N. Keegan, S.F. Ray, An Evaluation of Industrial Filtration Systems, Aluminium International Today. 15 (2003) 21–23.

[86] C. Voigt, B. Fankhänel, B. Dietrich, E. Storti, M. Badowski, M. Gorshunova, G. Wolf, M. Stelter, C.G. Aneziris, Influence of Ceramic Foam Filters with Al2O3 Nanocoating on the Aluminum Filtration Behavior Tested With and Without Grain Refiner, Metallurgical and Materials Transactions B: Process Metallurgy and Materials Processing Science. 51 (2020) 2371–2380. https://doi.org/10.1007/s11663-020-01900-1.

[87] S. Bao, M. Syvertsen, A. Nordmark, A. Kvithyld, T. Engh, M. Tangstad, Plant Scale Investigation of Liquid Aluminium Filtration by Al2O3 and SiC Ceramic Foam Filters, Light Metals. (2013) 981–986.

[88] M. Syvertsen, A. Kvithyld, S. Bao, A. Nordmark, A. Johansson, Parallel Laboratory and Industrial Scale Aluminium Filtration Tests with Al2O3 and SiC Based CFF Filters, Light Metals. (2014) 1041–1046. https://doi.org/10.1002/9781118888438.ch173.

[89] C. Voigt, E. Jäckel, C.G. Aneziris, J. Hubálková, Investigations of Reticulated Porous Alumina Foam Ceramics Based on Different Coating Techniques with the Aid of µCT and Statistical Characteristics, Ceramics International. 39 (2013) 2415–2422.

[90] C. Voigt, T. Zienert, P. Schubert, C.G. Aneziris, J. Hubálková, Reticulated Porous Foam Ceramics with Different Surface Chemistries, Journal of the American Ceramic Society. 97 (2014) 2046–2053. https://doi.org/10.1111/jace.12977.

[91] C.K.W. Solem, R. Fritzsch, R.E. Aune, Preliminary Experimental Study of the Thermal Stability and Chemical Reactivity of the Phosphate-Based Binder Used in Al2O3-Based Ceramic Foam Filters (CFFs), in: Extraction, The Minerals, Metals & Materials Society, 2018: pp. 1153–1163.

[92] D.A. Doutre, Hazards Associated with the Use of Bone Ash in Contact with Molten Aluminum, Light Metals. (2010) 797–800. https://doi.org/10.1007/978-3-319-48228-6_135.

[93] H. Salmang, H. Scholze, Keramik, in: 7th ed., Springer, 2007: p. 784.

[94] European Parliament and of the Council of the European Union, Regulation (EC) No 1272/2008, 2008.

[95] Linde, Säkerhetsdatablad, HSE-Datasheet. (2020). https://www.linde-gas.se/sv/images/Fosfin_1.1_SE_tcm586-443518.pdf (accessed January 4, 2021).

[96] K.J. Brondyke, Effect of Molten Aluminum on Alumina-Silica Refractories, Journal of the American Ceramic Society. 36 (1953) 171–174.

[97] M. Allahevrdi, S. Afshar, C. Allaire, Additives and the Corrosion Resistance of Aluminosilicate Refractories in Al-5Mg, JOM. 50 (1998) 30–34.

[98] A. Yurkov, Refractories for Aluminium: Electrolysis and the Cast House, Springer International Publishing, 2015.

[99] J.C. Viala, P. Fortier, J. Bouix, Stable and Metastable Phase Equilibria in the Chemical Interaction between Aluminium and Silicon Carbide, Journal of Materials Science. 25 (1990) 1842–1850.

[100] D.J. Lloyd, The Solidification Microstructure of Particulate Reinforced Aluminium/SiC Composites, Composites Science and Technology. 35 (1989) 159–179.

[101] M.F. Ashby, Mechanical Properties of Cellular Solids., Metallurgical Transactions. A, Physical Metallurgy and Materials Science. 14 A (1983) 1755–1769. https://doi.org/10.1007/BF02645546.

[102] S. Meille, M. Lombardi, J. Chevalier, L. Montanaro, Mechanical Properties of Porous Ceramics in Compression: On the Transition Between Elastic, Brittle, and Cellular Behavior, J Eur Ceram Soc. 32 (2012) 3959–3967. https://doi.org/10.1016/j.jeurceramsoc.2012.05.006.

[103] R. Brezny, D.J. Green, Uniaxial Strength Behavior of Brittle Cellular Materials, Journal of the American Ceramic Society. 76 (1993) 2185–2192. https://doi.org/10.1111/j.1151-2916.1993.tb07753.x.

[104] F.A.C. Oliveira, S. Dias, M.F. Vaz, J.C. Fernandes, Behaviour of Open-Cell Cordierite Foams under Compression, J Eur Ceram Soc. 26 (2006) 179–186. https://doi.org/10.1016/j.jeurceramsoc.2004.10.008.

[105] C. Voigt, J. Storm, M. Abendroth, C.G. Aneziris, M. Kuna, J. Hubálková, The Influence of the Measurement Parameters on the Crushing Strength of Reticulated Ceramic Foams, Journal of Materials Research. 28 (2013) 2288–2299. https://doi.org/https://doi.org/10.1557/jmr.2013.96.

[106] J. Hubálková, C. Voigt, A. Schmidt, K. Moritz, C.G. Aneziris, Comparative Phenomenological Study of Fracture Behavior of Ceramic and Glass Foams under Compressive Stress Using In Situ X-Ray Microtomography, Advanced Engineering Materials. 19 (2017) 1–9. https://doi.org/10.1002/adem.201700286.

[107] C.Q. Dam, R. Brezny, D.J. Green, Compressive Behavior and Deformation-Mode Map of an Open Cell Alumina, Journal of Materials Research. 5 (1990) 163–171. https://doi.org/10.1557/JMR.1990.0163.

[108] L.J. Gibson, M.F. Ashby, Cellular Solids: Structure and Properties, 2nd ed., Cambridge University Press, Cambridge, UK, 1997.

[109] K.C. Goretta, R. Brezny, C.Q. Dam, D.J. Green, A.R. de Arellano-Lopéz, A. Dominguez-Rodriguez, High Temperature Mechanical Behavior of Porous Open-Cell Al2O3, Materials Science and Engineering A. 124 (1990) 151–158. https://doi.org/10.1016/0921-5093(90)90145-S.

[110] W. Acchar, F.B.M. Souza, E.G. Ramalho, W.L. Torquato, Mechanical Characterization of Cellular Ceramics, Materials Science and Engineering A. 513–514 (2009) 340–343. https://doi.org/10.1016/j.msea.2009.02.012.

[111] R. Brezny, D.J. Green, Fracture Behavior of Open-Cell Ceramics, Journal of the American Ceramic Society. 72 (1989) 1145–1152. https://doi.org/https://doi.org/10.1111/j.1151-2916.1989.tb09698.x.

[112] R. Brezny, D.J. Green, C.Q. Dam, Evaluation of Strut Strength in Open-Cell Ceramics, Journal of the American Ceramic Society. 72 (1989) 885–889. https://doi.org/10.1111/j.1151-2916.1989.tb06239.x.

[113] R. Brezny, D.J. Green, The Effect of Cell Size on the Mechanical Behavior of Cellular Materials, Acta Metallurgica Et Materialia. 38 (1990) 2517–2526. https://doi.org/10.1016/0956-7151(90)90263-G.

[114] M. Emmel, C.G. Aneziris, Development of Novel Carbon Bonded Filter Compositions for Steel Melt Filtration, Ceramics International. 38 (2012) 5165–5173.

[115] B. Luchini, J. Hubálková, T. Wetzig, J. Grabenhorst, J. Fruhstorfer, V.C. Pandolfelli, C.G. Aneziris, Carbon-Bonded Alumina Foam Filters Produced by Centrifugation: A Route towards Improved Homogeneity, Ceramics International. 44 (2018) 13832–13840.

[116] Leica Microsystems Wetzlar GmbH, Leica MEF4A/MEF4M, (n.d.). https://www.upc.edu/sct/ca/documents_equipament/d_129_id-513.pdf (accessed January 6, 2022).

[117] Jenoptik, FAQ (Frequently Asked Questions) to ProgRes(R) CapturePro software, (2022). https://www.jenoptik.com/products/cameras-and-imaging-modules/microscope-cameras/faq-progres-capturepro-software (accessed January 6, 2022).

[118] ZEISS Germany, ZEISS Axio Vert.A1 - Inverted Routine Microscope for Materials, (2022). https://www.zeiss.com/microscopy/int/products/light-microscopes/axio-vert-a1-for-materials.html (accessed January 6, 2022).

[119] ZEISS Germany, ZEISS ZEN core - Software Suite for Connected Microscopy from the Materials Lab to Production, (2022). https://www.zeiss.com/microscopy/int/products/microscope-software/zen-core.html (accessed January 7, 2022).

[120] FELMI ZFE, Zeiss Ultra 55, (2022). https://www.felmi-zfe.at/instrumentation/sem/zeiss-ultra-55/ (accessed January 7, 2022).

[121] Bruker, Quantax EDS for SEM, (2021). https://www.bruker.com/en/products-and-solutions/elemental-analyzers/eds-wds-ebsd-SEM-Micro-XRF/quantax-eds-for-sem.html (accessed January 7, 2022).

[122] NTNU, JEOL JXA-8500F Electron Probe Micro analyzer (EPMA), (2022). https://www.material.ntnu.no/lab/material/equipment/ProdInfoEPMA.pdf (accessed January 7, 2022).

[123] Thermo Fisher Scientific Inc., Helios G4 UX DualBeam System, (2018). https://assets.thermofisher.com/TFS-Assets/MSD/Datasheets/Helios-G4-UX-Datasheet-Materials-Science.pdf (accessed January 7, 2022).

[124] NTNU, Transmission Electron Microscopes (TEM), (2017). https://www.ntnu.edu/temgemini/tem (accessed January 7, 2022).

[125] Thermo Fisher Scientific Inc., ARL 4460 Metals Analyzer, (2007). http://thermo.com.cn/Resources/200802/productPDF_922.pdf (accessed January 7, 2022).

[126] Drägerwerk AG & Co, Dräger-Tubes® for short-term measurements, (2019). https://www.draeger.com/en-us_us/Applications/Products/Portable-Gas-Detection/Gas-Detection-Tubes/Tubes/Short-term-Tubes (accessed December 12, 2019).

[127] P.C. Skaret, MTS 880, (2014). https://www.ntnu.no/wiki/display/imtlab/MTS+880 (accessed January 7, 2022).

[128] A. Bergin, C. Voigt, R. Fritzsch, S. Akhtar, L. Arnberg, C.G. Aneziris, R.E. Aune, Investigation of Mechanical and Thermo-Mechanical Strength of Ceramic Foam Filters (CFFs), Ceramics International. (2022) Submitted for publication.

[129] Pyrotek Inc., Mastics and Mortars, (2022). https://www.pyrotek.com/primary-solutions/aluminium/foundry/show/ProductLine/mastics-and-mortars (accessed January 7, 2022).

[130] A. Bergin, C. Voigt, R. Fritzsch, S. Akhtar, L. Arnberg, C.G. Aneziris, R.E. Aune, Performance of Regular and Modified Ceramic Foam Filters (CFFs) during Aluminium Melt Filtration in a Pilot Scale Setup, TMS Light Metals 2022. (n.d.) 640–648.

[131] Metso:Outotec, HSC Chemistry, (2022). https://www.hsc-chemistry.com/ (accessed January 7, 2022).

[132] Thermfact and GTT-Technologies, FactSage, (2022). https://www.factsage.com/ (accessed January 7, 2022).

[133] National Institute for Occupational Safety and Health, Phosphine - Immediately Dangerous to Life or Health Concentrations (IDLH), (2014). https://www.cdc.gov/niosh/idlh/7803512.html (accessed September 17, 2019).

[134] H. John, H. Hausner, Influence of Oxygen Partial Pressure on the Wetting Behaviour in the System Al/Al2O3, Journal of Materials Science Letters. 5 (1986) 549–551.

[135] S. Bao, K. Tang, A. Kvithyld, M. Tangstad, T. Abel Engh, Wettability of Aluminum on Alumina, Metallurgical and Materials Transactions B. 42 (2011) 1358–1366.

[136] S. Bao, M. Syvertsen, A. Kvithyld, T. Engh, Wetting Behavior of Aluminium and Filtration with Al2O3 and SiC Ceramic Foam Filters, Transactions of Nonferrous Metals Society of China. 24 (2014) 3922–3928.

[137] C. Voigt, L. Ditscherlein, E. Werzner, T. Zienert, R. Nowak, U. Peuker, N. Sobczak, C.G. Aneziris, Wettability of AlSi7Mg Alloy on Alumina, Spinel, Mullite and Rutile and its Influence on the Aluminum Melt Filtration Efficiency, Materials and Design. 150 (2018) 75–85.

[138] J. Yang, S. Bao, S. Akhtar, P. Shen, Y. Li, Influence of Grain Refiners on the Wettability of Al2O3 Substrate by Aluminum Melt, Metallurgical and Materials Transactions B. 52 (2021) 382–392.

[139] R. Fritzsch, T.L. Schanche, H. Zedel, A. Bergin, S. Akhtar, L. Arnberg, R.E. Aune, Aluminum Melt Cleanliness Analysis based on Direct Comparison of Computationally Segmented PoDFA Samples and LiMCA Results, Light Metals. (2022) 633–639.

[140] C. Voigt, J. Hubálková, A. Bergin, R. Fritzsch, S. Akhtar, R.E. Aune, C.G. Aneziris, Short- and Long-Term Aluminum Filtration Trials with Carbon-Bonded Alumina Filters, Light Metals. (2022) 626–632.

A. Publications

Paper 1

Experimental Study on the Chemical Stability of Phosphate-Bonded Al_2O_3-Based Ceramic Foam Filters (CFFs)

ARE BERGIN, CLAUDIA VOIGT, ROBERT FRITZSCH, SHAHID AKHTAR,
LARS ARNBERG, CHRISTOS G. ANEZIRIS, and RAGNHILD E. AUNE

Production of high-quality aluminum products requires an extensive melt treatment process, even more so with the increasing focus on recycling and sustainability. Filtration is a commonly used process segment for removal of non-metallic inclusions in aluminum, and ceramic foam filters (CFFs) are often used as the filtration media. In the present study, the chemical stability of phosphate-bonded Al_2O_3-based CFFs has been investigated. Three filters with different chemical compositions have been submerged into pure aluminum (with traces of Mg) and in an aluminum-magnesium melt (~ 2 wt pct Mg) at 730 °C. In addition to filter characterization before and after exposure to molten metal, using various imaging and X-ray techniques, the melt itself was analyzed by spark optical emission spectroscopy. The generation of phosphine gas was also measured by the use of Dräger tubes, and thermodynamic calculations performed using FactSage™. The phosphate-bonded filters were observed to react with the magnesium present in the molten aluminum even at very low magnesium concentrations (0.00035 wt pct), and as the magnesium concentration increased the severity of the degradation became more and more evident. The exposure time proved to have detrimental effect on the filter structure, with pieces of the filter struts broken off causing melt contamination. Severe filter degradation also resulted in color changes with accompanying diffusion of magnesium and phosphorus to and from the filter, respectively. Moreover, phosphine gas was released in amounts exceeding recommended exposure limits when the filter came in contact with the humidity in the air after testing. Good agreement was established to exist between the results from the thermodynamic calculations performed and the experimental results.

https://doi.org/10.1007/s11663-021-02144-3

I. INTRODUCTION

CERAMIC foam filters (CFFs) are widely used for the removal of non-metallic inclusions from molten metal during the casting step, and they are manufactured in large quantities with the use of a replica technique that is patented by Schwartzwalder *et al.*[1] The production process of ceramic foam filters consists of several steps in which a polyurethane (PUR) foam initially is coated by a ceramic slurry, followed by removal of excess slurry and a sintering step where the polyurethane decomposes and the ceramic foam remains. The key feature of ceramic foam filters is the porosity which can be divided into three main categories: (1) functional porosity (pores surrounded by the struts), (2) material porosity (pores within the struts), and (3) strut cavities (a result from decomposition of the polymeric foam), see Figure 1.

The main introduction of ceramic foam filters into the aluminum (Al) industry occurred in the 1970s[2] followed by a number of patents specifically describing filtration of aluminum.[3–5] Today, ceramic foam filters made of calcined alumina (Al_2O_3) are typically used in this area to improve the cleanliness of the cast metal. The filter ability to remove particles and inclusions is dependent on several factors, in which perhaps the most important one is the density of the functional pores, usually denoted ppi (pores per inch). It has been reported in the

---

ARE BERGIN is with the Department of Materials Science and Engineering, Norwegian University of Science and Technology (NTNU), 7034 Trondheim and also with the Research and Technology Development, Hydro Aluminium AS, 6600, Sunndalsøra, Norway. Contact e-mail: are.bergin@hydro.com; are.bergin@ntnu.no CLAUDIA VOIGT and CHRISTOS G. ANEZIRIS are with the Institute of Ceramics, Refractories and Composite Materials, Technische Universität Bergakademie Freiberg, 09599 Freiberg, Germany. ROBERT FRITZSCH, LARS ARNBERG, and RAGNHILD E. AUNE are with the Department of Materials Science and Engineering, Norwegian University of Science and Technology (NTNU). SHAHID AKHTAR is with the Karmøy Primary Production, Hydro Aluminium AS, 4265, Håvik, Norway

Manuscript submitted October 6, 2020, accepted March 4, 2021.

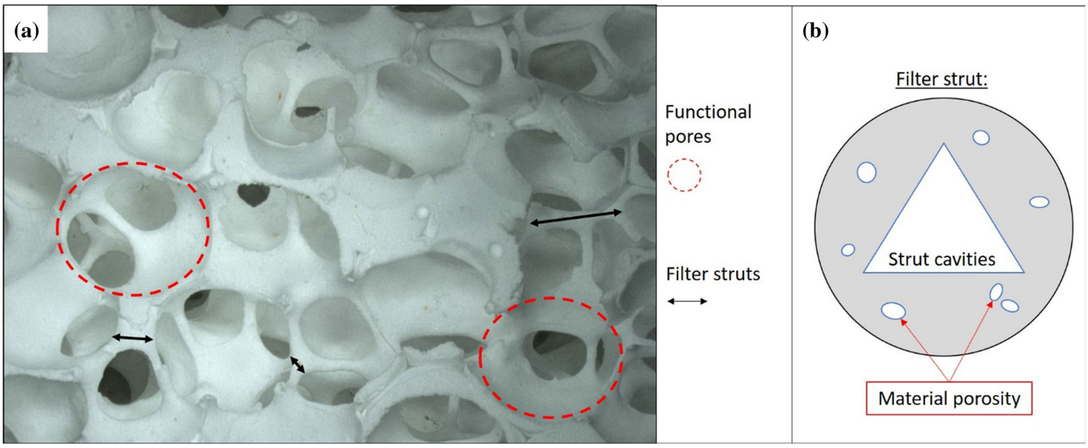

Fig. 1—A schematic presentation of pores in a ceramic foam filter: (*a*) a photograph of a filter where the functional pores and filter struts are marked, and (*b*) the strut cavity and material porosity of a filter strut.

literature that the filtration efficiency is in the range of 25 to 90 pct for 30 ppi filters and 55 to 95 pct for 50 filters.[6]

As pure Al_2O_3 has a melting point of 2050 °C,[7] the sintering temperatures of pure alumina filters are rather high, which causes an energy-intensive sintering step. Like most refractory materials, ceramic foam filters are cost sensitive which applies mostly due to their single use application. A reduction in production costs is, however, possible with the addition of an inorganic binder that reduces the sintering temperature and thereby the energy consumption. An often-used inorganic binder is phosphate, which provides excellent strength at low temperatures allowing easy product handling, and a reduction of the sintering temperature from around 1600 °C (pure alumina) to around 1300 °C. Additionally, the phosphate-bonded ceramics are suitable for fast sintering processes.[8] However, shrinkage is a negative effect of high-temperature sintering, which might deform the pores and lead to micro-crack formation especially for larger filter geometries. Due to this, suppliers tend to use slurry compositions where shrinkage is reduced to a minimum.

The constituents in the slurry of a conventional phosphate-bonded alumina ceramic foam filter are, as described in the patent by Brockmeyer,[5] 50 to 80 pct Al_2O_3, 1 to 5 pct of montmorillonite, 1 to 10 pct ceramic fibers, and 5 to 25 pct of a phosphate binder. According to Nishikawa,[8] monoaluminum phosphate ($Al(H_2PO_4)_3$) transforms to $Al(PO_3)_3$ at 315 °C with subsequent formation to a metaphosphate glass at temperatures between 1090 °C and 1300 °C, which is further transformed to $AlPO_4$ (berlinite) at temperatures between 1300 °C and 1500 °C. In the presence of alumina, the formation of $AlPO_4$ from $Al(PO_3)_3$ is accelerated and takes place at much lower temperatures, *i.e.*, between 700 °C and 1000 °C. $AlPO_4$ coats the alumina particles and thus acts as the bonding phase.[9]

In regard to phosphate-bonded ceramics, MgO has proven to act as a setting agent that accelerates the solidification of the ceramic slurry.[10] Furthermore, phosphates and magnesia can generate low-melting compounds (e.g., $Mg(PO_3)_2$ at 1165 °C), and MgO has been reported to break the aluminum phosphate bonds which decreases the mechanical strength of a ceramic foam filter at high temperatures.[10]

For the use of ceramic foam filters in other applications, such as hot gas filtration, it has been found that the manufacturing challenge lies in finding a suitable binder that can withstand the harsh and corrosive conditions that the filters in most cases are subjected to.[11]Within the area of molten aluminum filtration, it is known that the commonly used phosphate-bonded ceramic foam filters are less resistant when filtrating magnesium (Mg) containing alloys. However, the $AlPO_4$ degradation mechanism is not clearly understood, and very little have been reported on the topic in the literature. According to Aubrey *et al.*,[12] X-ray diffraction analysis of phosphate-bonded Al_2O_3-based ceramic foam filters, after immersion testing in an AlMg4.5Mn0.4 melt, confirmed the presence of Mg_3P_2 and MgO in the exposed filters. As a result, Eq. [1] was proposed to have taken place during the trials.

$$3\mathrm{AlPO_4} + 3\mathrm{Mg} \rightarrow \mathrm{Mg_3P_2} + 3\mathrm{MgO} + \mathrm{AlP}. \qquad [1]$$

Solem *et al.*[13] published diagrams with Gibbs free energy as a function of temperature for reactions between a series of common alloying elements in aluminum and 1 mole of phosphorus, which indicated that the formation of AlP is highly favorable at the casting temperature of aluminum. The formation of Mg_3P_2 was, however, not included in those diagrams, but if that had been the case it would have shown that Mg_3P_2 is more favored/stable than AlP at the temperature interval of interest (600 to 800 °C).

Related work has been performed by Doutre,[14] which describes that both AlP and Mg_3P_2 are potential products from reduction of bone ash when in contact with an aluminum-magnesium (Al-Mg) alloy. Bone ash, in which the main constituent is $Ca_3(PO_4)_2$ with small amounts of $CaCO_3$, $Mg_3(PO4)_2$, and CaF_2,[7] is a fine white powder created by the calcination of animal bones and is used on refractory materials in the aluminum industry to prevent molten metal from sticking/reacting with the refractory. Both AlP and Mg_3P_2 could further react with water or moisture in the air according to Eqs. [2] and [3] and form phosphine gas (PH_3).[14] The formation of PH_3 (g) was proved post melt exposure by Aubrey *et al.*, using Dräger tubes and a handheld photoionization detector.[12]

$$Mg_3P_2 + 6H_2O \rightarrow 2PH_{3(g)} + 3Mg(OH)_2 \qquad [2]$$

$$AlP + 3H_2O \rightarrow PH_{3(g)} + Al(OH)_3. \qquad [3]$$

PH_3 (g) is defined as an extremely flammable (F+) and very toxic (T+) gas, which is dangerous for the environment (N).[15] The recommended exposure limits for PH_3 (g) set by the US National Institute for Occupational Safety and Health (NIOSH) are 0.3 ppm for TWA* and 1 ppm for STEL **.[16] In addition, PH_3 (g) has an autoignition temperature of 38 °C,[17] and has been identified as a likely cause for salt cake† landfill fires.[14]

In 1997, an estimated 800,000 tons of salt cake was annually landfilled in the US,[18] and it has been estimated that salt slags typically can emit around 0.03 to 0.06 m^3 $PH_{3(g)}$ per ton salt cake.[19]

The main objective of the present study has been to investigate the chemical stability of phosphate-bonded Al_2O_3-based ceramic foam filters in contact with molten aluminum, *i.e.,* with pure aluminum and an aluminum-magnesium (Al-Mg) alloy, as well as to measure any subsequent release of PH_3 (g). In addition, thermodynamic calculations have been performed to support the findings.

II. EXPERIMENTAL MATERIALS AND PROCEDURES

A. *Characterization of Aluminum Melts and Ceramic Foam Filters*

All ceramic foam filters were subjected to two different aluminum melts to test the influence of magnesium on their chemical stability, *i.e.* pure aluminum (with traces of magnesium) and an aluminum-magnesium alloy (AlMg2). The AlMg2 alloy was manually prepared from pure aluminum ingots with additions of magnesium to the melt at 740 °C and subsequent stirring for ~ 1 minute. The use of spark optical emission spectroscopy (SOES-ARL 4460, Thermo Fischer Scientific) revealed that there were small variations in the composition of the AlMg2 batches, especially in regard to the Mg concentration (ranging from 2.22 to 2.32 wt pct), see Tables I and II.

Three different Al_2O_3-based ceramic foam filters were tested in two distinct experimental set-ups, see Table III. As can be seen from the table, the majority of the tested filters were of grade 30 except for the 100pctAl_2O_3 filter used during the gravity priming procedure, which was of grade 40 (grade is a newly introduced term explaining functional pore size equal to ppi (pores per inch)). All filters were characterized as received, by embedding samples of the filters in an epoxy resin with subsequent grinding and polishing. The polished samples were investigated with the help of an Ultra 55 LE scanning electron microscope (SEM) (Zeiss, Germany) equipped with an XFlash Detector 4010 energy-dispersive X-ray microanalysis (EDS) unit (Bruker AXS, Germany). The chemical composition of the different filters is also presented in Table III, and is based on 6 measurements from a window size of ~ 10 × 10 μm^2. As can be seen from the table, the Al_2O_3+P1 and Al_2O_3+P2 filters were phosphate-bonded ceramic foam filters, whereas the 100pctAl_2O_3 filter was phosphate free and used as a reference. Additionally, mercury intrusion porosimetry (MIP) measurements were performed for evaluation of the size of the pore structures using an Autopore 5 (Micromeritics, USA). A penetrometer (with a cup volume of 15 cm^3 and a stem volume of 0.392 cm^3) was used, which allowed for measurements of relatively large samples (> 10 × 10 × 10 mm^3). A total of 295 measuring points was used, ranging between 0.15 and 420 MPa, with an equilibrium time of 5 seconds. The measured pressure p was converted into the corresponding pore radius r with the help of Washburn's equation (see Eq. [4]) where θ is the contact angle (140° was used) and γ the surface tension of mercury (0.485 Nm^{-1} was used).

$$p = 2\gamma \cos\theta / r. \qquad [4]$$

B. *Priming Procedures*

For the investigation of the chemical stability of ceramic foam filters when in contact with molten

---

*TWA (Time-Weighted Average) is described as the average exposure over an 8-hour period, i.e., a working day

**STEL (Short-Term Exposure Limit) is described as the average exposure over a period of 15 minutes

†Salt cake is a biproduct from the aluminum industry that normally includes used ceramic foam filters

Table I. The Average Chemical Composition of the Main Components in the Aluminum Melts Used During Gravity Priming of Ceramic Foam Filters

Alloy	Si	Fe	Cu	Mn	Mg	Zn	Al
Pure Al	0.07 ± 0.007	0.17 ± 0.005	n/a	n/a	$0.0018 \pm 3E^{-4}$	$0.01 \pm 1E^{-4}$	99.69 ±0.02
AlMg2	0.10 ± 0.02	0.19 ± 0.01	n/a	0.20 ± 0.01	2.33 ± 0.09	n/a	97.11 ±0.1

The chemical compositions were acquired by SOES at the start of each trial and are presented in [Weight Percent]. Very low or not applicable values are stated as n/a.

Table II. The Average Chemical Composition of the Main Components in the Aluminum Melts Used During Electromagnetic Priming of Ceramic Foam Filters

Alloy	Si	Fe	Cu	Mn	Mg	Zn	Al
Pure Al	$0.05 \pm 6E^{-4}$	0.14 ± 0.003	n/a	n/a	$0.00035 \pm 6E^{-5}$	n/a	99.78 ± 0.004
AlMg2	$0.06 \pm 7E^{-4}$	0.17 ± 0.002	n/a	n/a	2.26 ± 0.04	n/a	97.48 ± 0.04

The chemical compositions were acquired by SOES at the start of each trial and are presented in [Weight Percent]. Very low or not applicable values are stated as n/a.

Table III. A Test Matrix Presenting the Different Ceramic Foam Filters

Filter Identification	Electromagnetic Procedure	Gravity Procedure	Composition [Weight Percent]
$Al_2O_3 + P1$	grade 30	grade 30	Al_2O_3-based, with ~ 4.7 pct P and ~0.6 pct Si
$Al_2O_3 + P2$	—	grade 30	Al_2O_3-based, with ~ 2.8 pct P, ~ 3.2 pct Si and ~ 0.4 pct Na
100 pctAl_2O_3	grade 30	grade 40	Al_2O_3-based, no other elements identified

aluminum, it is essential to initially prime the filters, *i.e.*, filling the filter's functional porosity with molten metal and removing entrapped air. Priming of filters usually requires a metal head of several cm (lab scale) to create sufficient pressure to initiate a flow of metal through the filter.[20] This implies that a simple dipping of the filters in a molten metal bath will not achieve filling of the functional porosity.

In the present study, two different priming procedures were used, *i.e.*, gravity priming and electromagnetic priming. In the gravity priming procedure, an adequate metal head was secured to achieve metal filling of the functional pores. This priming procedure simulated conventional cast house priming and allowed for dynamic conditions in regard to total immersion time. In the case of the electromagnetic priming procedure, an electromagnetic field was used for filter priming, which also allowed for the measurement of metal composition and PH_3 (g) formation.

1. *Gravity priming*

The gravity priming trials were performed using a customized immersion set-up utilizing a resistance furnace equipped with an automatic temperature control unit and a Noltina Stabil crucible (Morgan MMS, Germany). Four fused silica tubes acting as sample holders for the filters were individually clamped and connected to a rotating wheel. This set-up allowed the tubes to be lowered into the molten metal bath and slowly lifted before being lowered again, to simulate the filtration step where metal flows through the filter, see Figure 2. The clamps were designed in such a way that the silica tubes went through the same reciprocating up-and-down motion in the bath, but could be individually removed from the bath at different times. The furnace was filled with 41 kg of aluminum which was melted and heated up to a temperature of 730 °C (see Table I for details on the chemical composition). Three trials were performed at the same day using the same 41 kg of molten aluminum, but in between each trial 1 to 3 kg of new metal was added to keep the level of the aluminum melt constant and compensate for oxidation of magnesium.

The tested filters had a diameter of 4 cm and a height of 5 cm, and prior to being used they were stored at a temperature comparable to casthouse conditions. They were glued into individual fused silica tubes, which were coated with boron nitride (BN) on the lowermost parts (approximately at the same height as the filters), using an inert Ca-Al-B glass. The four filter tubes were preheated using an air velocity burner to temperatures between 708 °C and 840 °C measured by individual thermocouples placed inside each silica tube. Efforts were made to avoid direct heating of the filters, before they were immersed into the molten aluminum. Prior to lowering the filters into the bath, the aluminum oxide layer on the surface of the molten aluminum was removed from the area of tube immersion. The priming

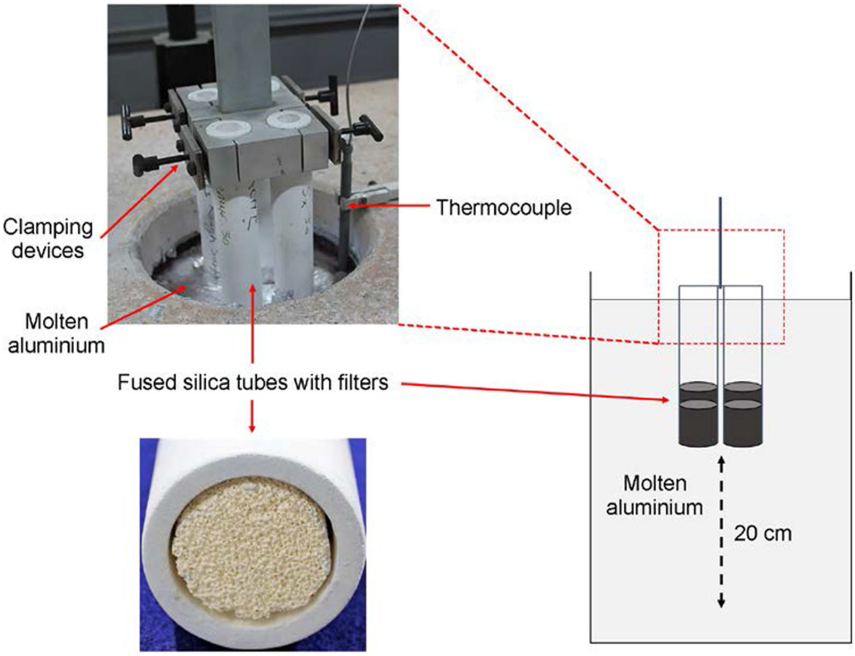

Fig. 2—Set-up of the gravity priming experiments with a reciprocating up-and-down motion of the filters in an aluminum melt.

of the filters was reached by a 20 cm vertical movement of the filter tubes, resulting in a sufficient metal head pressure, melt stirring, and melt movement within the filter. The vertical movement corresponded to an industrial filtration velocity of 14.11 kg/cm^2·hour per filter, which was calculated using the amount of metal passing through the filter per second (0.049 kg/second based on the height and the pace (24.2 seconds per motion) of the filter movement, assuming that the complete filter volume was aluminum) and dividing that by the filter inlet area (12.57 cm^2). The samples tested in the same trial were either removed simultaneously from the bath after 30, 60, 90, and 120 minutes, or one by one at different times. After removal from the bath, the filters were placed on a chill plate to minimize the drainage of the molten metal from the filters, thereby securing as much solidified aluminum within the filters as possible. Further cooling was performed in ambient conditions. All filters were tested using the gravity priming procedure.

2. *Electromagnetic priming*

The electromagnetic priming trials were performed by applying an electromagnetic field around a crucible with molten metal and submerging the filter samples into the melt,[20,21] see Figure 3. As can be seen from the figure, a coil prepared from water-cooled copper tubes in two layers were used for the generation of an electromagnetic field of 80.0 mT in the center of the coil (measured with a Hall Effect gauss meter, model 6010 by Pacific Scientific OECO, F.W. Bell®, USA). The coil was connected to a power supply delivering a voltage of 29 V and a current of 540 A. The experimental set-up is based on patented technology developed at the lab of the Department of Materials Science and Engineering, Norwegian University of Science and Technology (NTNU).[22]

The aluminum metal used during the trials (see Table II for the chemical composition) was melted at 730 °C in a resistance furnace within a boron nitride (BN)-coated Salamander Super A8 crucible (Morgan MMS, Germany). Argon gas (5N), at a flow rate of 2 standard liters per minute (SLPM), was used to reduce melt oxidation. Samples of the molten metal were secured with the help of a scoop prior to filter submersion and at an interval of 30 minutes during the trials, *i.e.*, 5 samples cast in a copper chill mold were retrieved from each trial. The chemical compositions of the samples were obtained by spark optical emission spectroscopy (ARL 4460, Thermo Fischer Scientific, USA). Prior to filter submersion as well as each sampling, the melt surface was skimmed.

The priming procedure was performed by removing the crucible with the molten metal from the furnace and positioning it in the center of the coil with subsequent immersion of a filter, with a size of 5 × 5 × 5 cm^3 and preheated to ~ 600 °C, for 20 to 35 seconds while the magnetic field was applied. Priming was observed to occur almost instantly, and a temperature drop of 22 ± 3 °C was measured as an effect of the priming procedure and the initial sampling. After priming, the crucible was placed back in the furnace for 2 hours

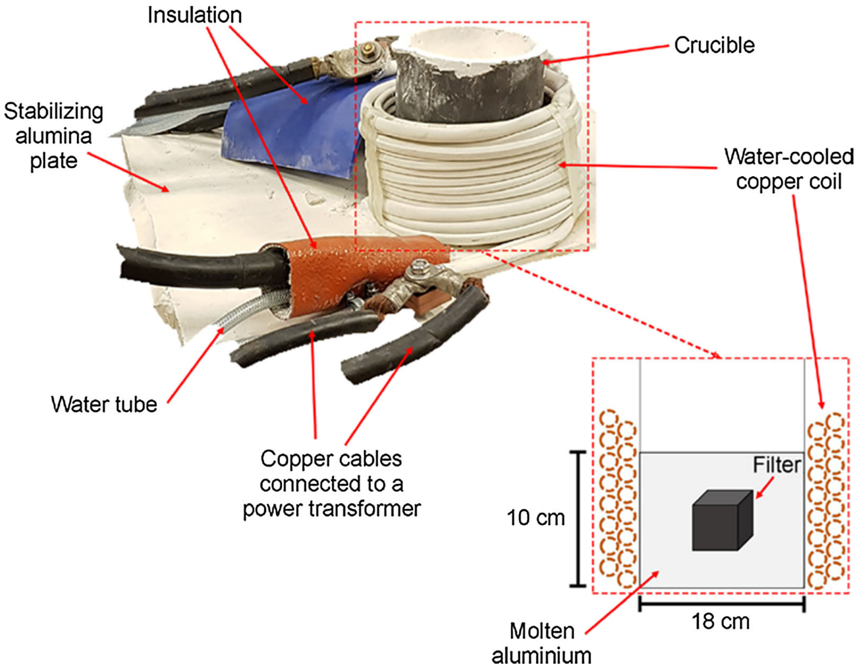

Fig. 3—Set-up of the electromagnetic priming experiments with a two layered copper coil and a crucible with a filter submerged in an aluminum melt (Color figure online).

securing melt reheating. The filter was moved around in the crucible prior to each melt sampling sequence, to obtain a high uniformity of the chemical composition of the sample as well as to induce some melt movement within the filter.

The filter was removed from the aluminum melt at the end of the trial and cooled to room temperature in air with an absolute humidity in the range 7.27 to 9.39 g/m^3 (which is based on historic data from the Norwegian Meteorological Institute[23] and the saturation pressure at different temperatures,[24] with the assumption that the humidity is equal outside and inside). The retrieval step did, however, cause some of the melt to drain from the filter (see Figure 4), which was taken into consideration during sampling. The filter was tested for generation of PH_3 (g) using a Dräger-Tube®[25] positioned ~ 1 cm above the cooling filter, ~ 30 minutes after retrieval. Due to the hazardous nature of PH_3 (g), strict safety measures were taken upon filter handling and gas measuring, *i.e.*, gas mask, gas safety detector, room ventilation, and filter sample storage in a ventilated cabinet post handling.

C. *Sample Preparation and Analyzing Methods*

A sample with the dimensions ~ 30 × 30 mm^2 was secured from each gravity primed filter, and with the dimensions ~ 15 × 15 mm^2 from each electromagnetically primed filter. The samples were cut from the bottom of each filter, at the same position each time (see Figure 4), and mounted in epoxy with subsequent grinding using SiC paper down to a size of 5 μm, with either water or ethanol as lubricant.

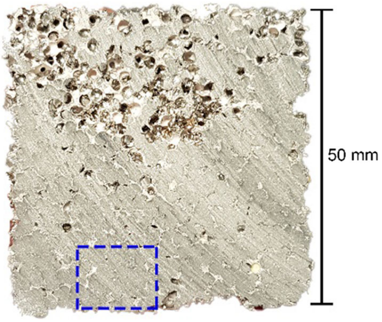

Fig. 4—Position (blue dotted square) of the sample secured from each filter tested using both the gravity- and electromagnetic priming procedures (the present filter is electromagnetically primed) (Color figure online).

The samples were analyzed by light optical microscopy (LOM) using a Leica MEF4M (Germany) unit connected to the ProgRes CapturePro software system (Jenoptik, Germany). Polarized light and a teal colored filter were used to visualize and increase the contrast between the filter media, the metal phase, and the interface between the two. Each sample was analyzed at magnifications ranging from 25× to 200×. Qualitative chemical analyses of the same areas were later performed by electron probe microanalysis (EPMA) using a JEOL JXA-8500F (Germany) unit. The analysis was performed on an area of 1 × 1 mm^2 with a probe current of 30 nA for the mapping of the elements Al, O, P, C, Si, Mg, Ti, Fe, K, and B. Analysis was also performed by field emission scanning electron microscopy (FESEM) using a Zeiss Ultra 55 Limited Edition (Germany) unit with an accelerating voltage of 10 kV and a working distance of 10 mm. The chemical composition of the cast metal samples was analyzed by spark optical emission spectroscopy (SOES) using an ARL 4460 (Thermo Fischer Scientific, USA) unit.

In addition, one sample immersed in pure aluminum was examined with the help of transmission electron microscopy (TEM). A thin lamella was collected from the filter–metal interface with a focused ion beam scanning electron microscope (FIB-SEM) using a Helios G4 UX Dual-beam (Thermo Fisher Scientific, USA) unit. The lamella was cut out from the sample and transferred to a dedicated copper half grid using a standard lift-out technique. Coarse thinning was performed at an acceleration voltage of Ga+ ions of 30 kV, while the final thinning was performed at 5 and 2 kV to minimize surface damage on either side of the lamella. Element analysis was performed with a double Cs aberration-corrected cold field emission gun (FEG) using a JEOL ARM 200FC (Japan) unit equipped with an energy-dispersive X-ray microanalysis (EDS) detector (Centurio, JEOL, Japan) and a dual electron energy loss spectrometer (EELS) unit (Quantum ER GIF, Gatan, USA). The FEG was operated at 200 kV.

III. RESULTS AND DISCUSSION

A. *Thermodynamics*

The Gibbs free energy (ΔG) as a function of temperature has been plotted for the reactions presented in Eqs. [2] and [3] with data from the Reaction Equations module of HSC Chemistry® 9.9.2.3, see Figure 5. As can be seen from the figure, the driving force for the formation of PH_3 (g) from both AlP and Mg_3P_2 is negative when the species are in contact with sufficient quantities of H_2O. Thus, both species will spontaneously form PH_3 (g) when in direct contact with either water or the moisture in the air. However, for these reactions to actually take place AlP and Mg_3P_2 will have to be present in the system.

Table IV. Equilibrium Calculations of the Output Mass of AlP and $MgAl_2O_4$ When an Al-Mg Melt Comes in Contact with a Phosphate-Bonded Al_2O_3-Based Ceramic Foam Filter at 730 °C and 1 atm Pressure (the Filter Constituents Were Added as Components in the Melt)

Species	Input Mass [g]	Output Mass [g]
Al	2200	—
Mg	55	—
Al_2O_3	45	—
$AlPO_4$	5	—
AlP	—	2
Spinel (78 wt pct $MgAl_2O_4$)	—	54

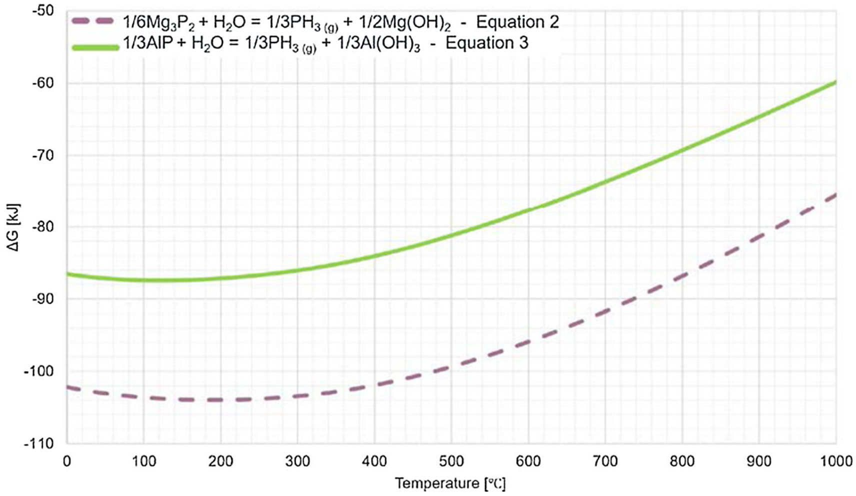

Fig. 5—Gibbs free energy (ΔG) as a function of temperature for reactions where the species AlP and Mg_3P_2 react with 1 mole of H_2O, in the temperature range of 0 to 1000 °C, drawn using data from the Reaction Equations module of HSC Chemistry® 9.9.2.3.

The amounts of AlP and $MgAl_2O_4$ produced when an Al-Mg melt comes in contact with a phosphate-bonded Al_2O_3-based ceramic foam filter at 730 °C and 1 atm pressure have been calculated in an open system with a protective atmosphere of Ar (g), see Table IV. The Equilib module in the FactSage™ 7.3 software was used for the calculation together with the FactPS, FToxid, and FTlite databases. The input values were based on the experimental conditions used in the present study during electromagnetic priming of a 50 g Al_2O_3-based filter (assumed to contain 5 wt pct of an $AlPO_4$ binder [5]), in a Mg-alloyed aluminum melt (2.5 wt pct Mg given zero Mg oxidation). Moreover, the calculation was performed in an open system over 100 steps with 2 liters of Ar (g) added at each step and ~ 0.6 liters of air with a water vapor content of ~ 30 pct at step 1 (N_2 in the air was treated as inert). It was assumed that equilibrium existed between all phases at all times, and the reaction kinetics was neglected. In addition, the filter constituents were added as components in the melt. The change in conditions over the steps, as well as the output mass of each component, proved to be insignificant.

As can be seen from Table IV, formation of AlP and $MgAl_2O_4$ will occur for the evaluated case, hence also under normal aluminum cast house conditions. In other words, some of the P released from the $AlPO_4$ binder will form AlP, while the rest will enter the aluminum melt (will be discussed in more detail later).

A predominance diagram for the system Al-Mg-P-O, assumed to consist of an ideal gas mixture of O_2 (g) and P_2 (g), was also calculated at a fixed temperature of 727 °C using the Predom module of the FactSage™ 7.3 software and the same databases as in previous calculations, see Figure 6. The area on the right side of the diagram representing the area for Al_2O_3 (s) and $MgAl_2O_4$ (s) extends to a partial pressure of O_2 (g) equal to 1×10^{-23} atm and more or less the complete interval of the partial pressure of P_2 (g). As a result, the line on the left side of this area (marked with a pink dotted line) represents the boundary layer between the filter medium and the bulk of the aluminum melt. The partial pressures of O_2 (g) and P_2 (g) were also calculated using the same case as above, *i.e.*, the electromagnetic priming conditions, resulting in values equal to 6.3×10^{-49} and 7.6×10^{-16} atm, respectively. As can be seen from the diagram, the phases that will form at these partial pressures are AlP (s) and $MgAl_2O_4$ (s) (marked with a red dot and red lines). The diagram also reveals that small changes in the partial pressures will affect phase formation.

B. *Characterization of Unexposed Filters*

The porosity of the different filter materials (as received) was investigated by the use of scanning electron microscopy, and clear differences were identified to exist, see Figure 7. As can be seen from the figure,

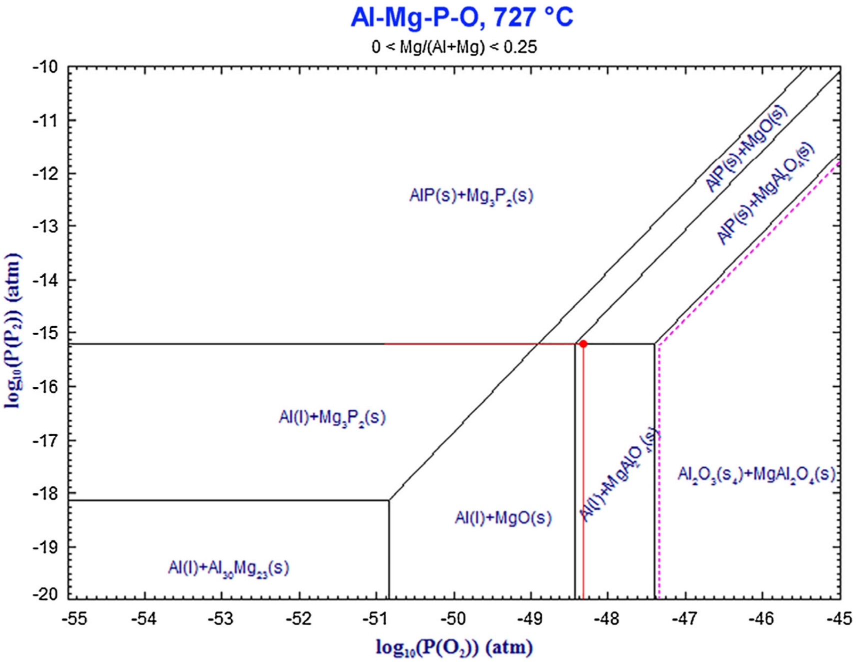

Fig. 6—A predominance diagram for the system Al-Mg-P-O at 727 °C, as calculated by FactSage™ 7.3, with the logarithm of the partial pressures of O_2 (g) and P_2 (g) on the x- and y-axis, respectively. The pink dotted line represents the boundary layer between the filter medium and the bulk of the aluminum melt, and the red dot and lines mark the calculated partial pressures for O_2 (g) and P_2 (g) during electromagnetic priming of a phosphate-bonded Al_2O_3-based ceramic foam filter in an Al-Mg melt (Color figure online).

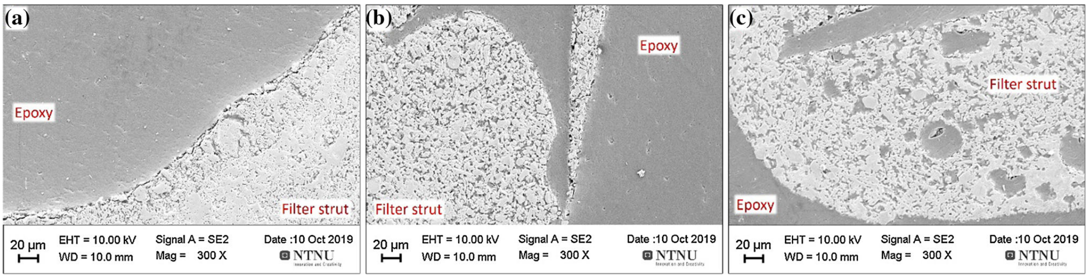

Fig. 7—SEM micrographs of the following as-received filters: (*a*) 100pctAl_2O_3, (*b*) Al_2O_3 + P1, and (*c*) Al_2O_3 + P2.

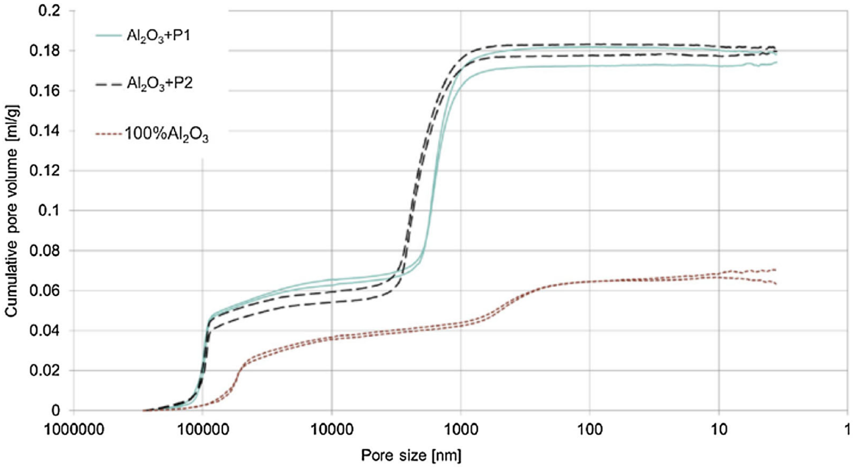

Fig. 8—Cumulative pore volume as a function of the pore size measured by mercury intrusion porosimetry (MIP).

the 100pctAl_2O_3 ceramic foam showed a relative dense microstructure of the struts compared to the commercial Al_2O_3 + P1 and Al_2O_3 + P2 foams. The latter even consisted of a significantly larger pore size than Al_2O_3 + P1.

The differences in porosity between the foams were measured by mercury intrusion porosimetry giving the following results: ~ 20 pct for 100pctAl_2O_3, ~ 37 pct for Al_2O_3 + P1 and ~ 41 pct for Al_2O_3 + P2. The cumulative pore volumes as a function of the pore size were plotted for each of the performed measurements, see Figure 8. As can be seen from the figure, a two-step increase of the cumulative pore volume can be identified. The first strong increase, where the pore sizes of the Al_2O_3 + P1 and Al_2O_3 + P2 filters were measured to be ~ 100 μm and for 100pctAl_2O_3 ~ 60 μm, corresponds to the filling of mercury in the strut cavities of the foam.[26] The variations between the phosphate-bonded Al_2O_3 and the pure Al_2O_3 filters are believed to be the result of differences in the polyurethane foam used during production, as well as in the ceramic composition (as the 100pctAl_2O_3 filter shrunk during sintering which was not the case for the phosphate-bonded Al_2O_3 + P1 and Al_2O_3 + P2 filters).

The second strong increase of the cumulative mercury volume occurred at mean pore sizes of ~ 1.5 μm for the Al_2O_3 + P1 filter, ~ 2.2 μm for the Al_2O_3 + P2 filter, and ~ 0.4 μm for the 100pctAl_2O_3 filter, corresponding to the filling of the pores in the strut, *i.e.*, the material porosity. The small mean pore size of the 100pctAl_2O_3 foam confirms the observation made by scanning electron microscopy.

The difference in pore size measured with scanning electron microscopy and mercury intrusion porosimetry can be explained by a difference in the measuring techniques. During mercury intrusion porosimetry, the pores in the interior of the sample can only be reached by mercury through a chain of entryways between the pores. As a result, the larger pores in the strut center are not intruded by mercury before the pressure needed to penetrate the narrower entryways is reached. Thus, the mercury intrusion porosimeter measures the largest entrance of a pore and not the pore cavities themselves. In contrast, scanning electron microscopy images allow the observation of the pore cavities.

The chemical composition of the ceramic foam filters was characterized using energy-dispersive X-ray micro-analysis and revealed, as previously presented in Table III, that $Al_2O_3 + P1$ and $Al_2O_3 + P2$ were phosphate-bonded filters whereas the $100pctAl_2O_3$ was phosphate free.

C. *Gravity Priming*

Light optical microscopy images of the three different filters immersed by gravity priming for 120 minutes in pure aluminum and AlMg2 are presented in Figures 9 and 10. The turquoise color seen in the images is, as previously mentioned, the result of using a teal colored filter to compensate for optical and illumination issues in order to improve contrast.

No visual degradation could be observed in either of the filters immersed in the pure aluminum melt (see Figures 9(a) through (c)) or in the case of the $100pctAl_2O_3$ filter immersed in the AlMg2 melt (see Figure 10(a)). A clear color change from milky white to different gradients/shades of brown/black was, however, visible at the edge of the $Al_2O_3 + P1$ filter immersed in AlMg2, see Figure 10(b). As can be seen from this image, a layered gradient exists from the filter–metal interface to the center of the filter strut, *i.e.,* from a darker brown/black area at the filter–metal interface and ~ 100 μm inwards (marked with 4), succeeded by a ~ 50μm lighter brown area (marked with 5), followed by an unreacted milky white area at the center of the strut (marked with 6). These changes in color indicate that a reaction and/or self-diffusion of elements to or from the filter have occurred. The $Al_2O_3 + P2$ filter, see Figure 10(c), revealed a more uniform brown/black color throughout, indicating that the changes in question had occurred throughout the whole filter strut.

Elemental mapping of the filters immersed in AlMg2 was performed by electron probe microanalysis, where the elements Al, O, P, C, Si, Mg, Ti, Fe, K, and B were analyzed. Only the most interesting results for the present study are presented, *i.e.*, the results of Al, O, P, and Mg. As can be seen from Figure 11, the $100pctAl_2O_3$ filter reveals the presence of Al and O with only a minor intrusion of Mg into the strut. No further reactions seem to have taken place.

A stepwise (layer by layer) increase of the concentration of P from the edge of the filter towards the center of the strut can be seen from the elemental mapping of the $Al_2O_3 + P1$ filter presented in Figure 12, with the lowest concentration of P at the filter–metal interface, *i.e.*, at

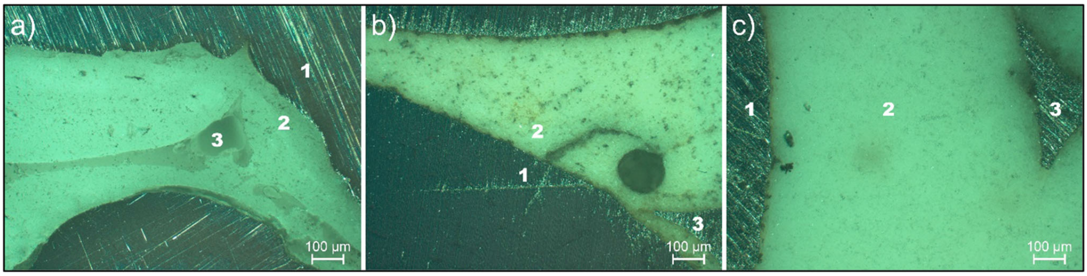

Fig. 9—LOM images at 100x magnification of the filters immersed with gravity priming for 120 min in pure aluminum: (*a*) $100pctAl_2O_3$, (*b*) $Al_2O_3 + P1$, and (*c*) $Al_2O_3 + P2$. Polarized light and a teal color filter were used, which explains the turquoise color. The numbers in the images mark the following phases: (1) aluminum, (2) filter strut, and (3) strut cavity (Color figure online).

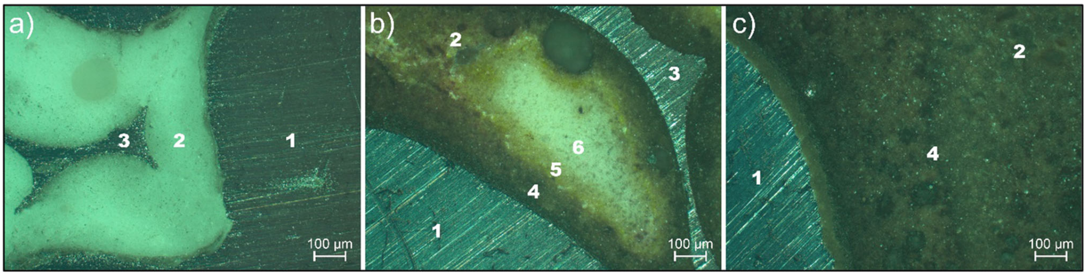

Fig. 10—LOM images at 100x magnification of the filters immersed with gravity priming for 120 min in AlMg2: (*a*) $100pctAl_2O_3$, (*b*) $Al_2O_3 + P1$, and (*c*) $Al_2O_3 + P2$. Polarized light and a teal color filter were used, which explains the turquoise color. The numbers in the images mark the following phases/medias: (1) aluminum, (2) filter strut, (3) strut cavity filled with aluminum, (4) fully reacted area, (5) moderately reacted area, and (6) slightly reacted area (Color figure online).

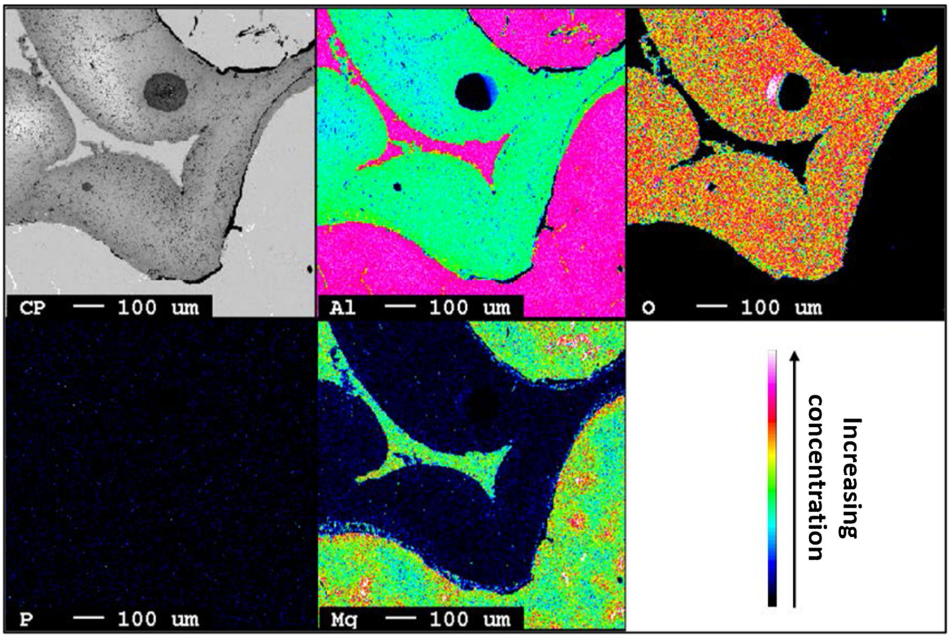

Fig. 11—EPMA mapping of Al, O, P, and Mg for the 100pctAl_2O_3 filter immersed by the gravity priming procedure in the AlMg2 melt for 120 min.

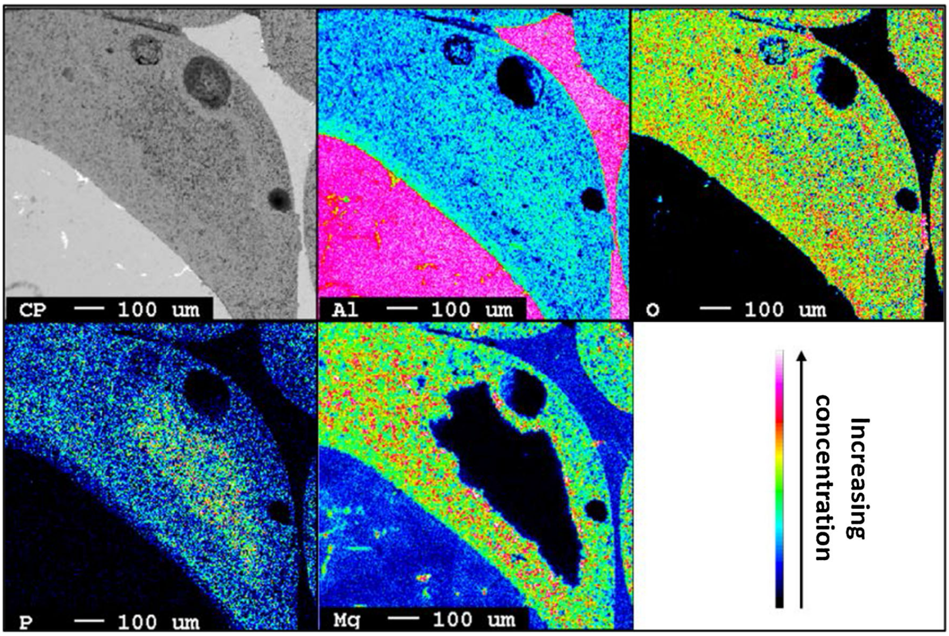

Fig. 12—EPMA mapping of Al, O, P, and Mg for the $Al_2O_3 + P1$ filter immersed by the gravity priming procedure in the AlMg2 melt for 120 min.

the edge towards the functional pore and the strut cavity. This corresponds well with the discoloration identified by light optical microscopy (Figure 10(b)) if assuming that the discoloration is a result of AlP formation and that some of the P has diffused from the filter into the metal leaving this area of the filter more or less depleted of P. In addition, an increase of the Al and the Mg concentrations was established to exist at the edge of the filter. In the case of Mg, this was the result of diffusion of Mg from the AlMg2 melt into the filter. It is, however, notable that the diffusion at the edge of the strut cavity was at a slightly lower level than at the edge of the functional pore size. The increase of the Al concentration at the edge of the filter strut was less pronounced than the Mg increase, and at the edge of the strut cavity the increase was neglectable (nearly not visible).

In Figure 13(a), a scanning electron microscopy image of the $Al_2O_3 + P1$ filter is presented. It can clearly be seen that metal has penetrated the strut cavities, as well as the material pores within the strut. It is believed that the diffusion of P from the strut edge of the filter into the metal has left pores and/or pore entryways facilitating this penetration and thereby compromising the filter structure. The presence of molten aluminum in the strut cavities has caused a larger reaction area, which in turn has increased the reaction. In Figure 13(b), it can be seen that large fragments of the ceramic structure detached from the filter strut as a result of what is believed to have been an intergranular attack due to binder degradation. Loose filter fragments may cause a reduction of the filter strength and end up in the Al melt, contaminating it and possibly also the final cast product. Even another mechanism has been reported in the literature to enable this process in industrial settings, *i.e.*, lateral compressive edge crushing, which is described as a combination of binder degradation, thermal expansion, and compressive modulus, as well as the lateral compressive stress that the filter is exposed to in the filter bowl.[12]

Elemental mapping of the $Al_2O_3 + P2$ filter revealed a stepwise (layer by layer) change in the concentration of P as well, from the edge of the filter towards the center of the strut, see Figure 14. In this case, the layer at the edge of the strut proved to have the highest concentration of P with a decrease towards the center (which is in contrast to the observations made for the $Al_2O_3 + P1$ filter). As the discoloration identified by light optical microscopy (Figure 10(c)) was more uniform brown/black, the degradation of the binder was believed to have come closer to equilibrium in view of the formation of AlP (again assuming that the discoloration is a result of AlP formation). The higher concentration of P at the edge of the strut is believed to be unreacted P that has diffused from the center of the strut towards the edge for further diffusion into the metal (which has not yet occurred). Moreover, a homogenous distribution of Al throughout the filter was established, and the diffusion of Mg from the AlMg2 melt into the filter was less pronounced with the highest concentration towards the edge of the strut. A gap filled with epoxy, believed to be the result of solidification shrinkage, was also identified to exist at the filter–metal interface containing small amounts of P.

Moreover, metal pore penetration was confirmed by scanning electron microscopy in the case of the $Al_2O_3 + P2$ filter, although at a lesser extent than described for the $Al_2O_3 + P1$ filter. The obtained structure bear close resemblance to observations reported in the literature to be the result of intergranular attacks due to binder degradation.[12]

As the experimental set-up used during the gravity priming trials allowed for the filter samples to be simultaneously immersed into the Al melt but individually withdrawn, trials were also performed varying the immersion time. Light optical microscopy images of the $Al_2O_3 + P1$ and $Al_2O_3 + P2$ filters immersed in AlMg2 for 30, 60, and 120 minutes are presented in Figure 15. As can be seen from Figures 15(a) through (c), a relatively thin discolored layer (dark brown/black) was established to have formed at the edge of the $Al_2O_3 + P1$

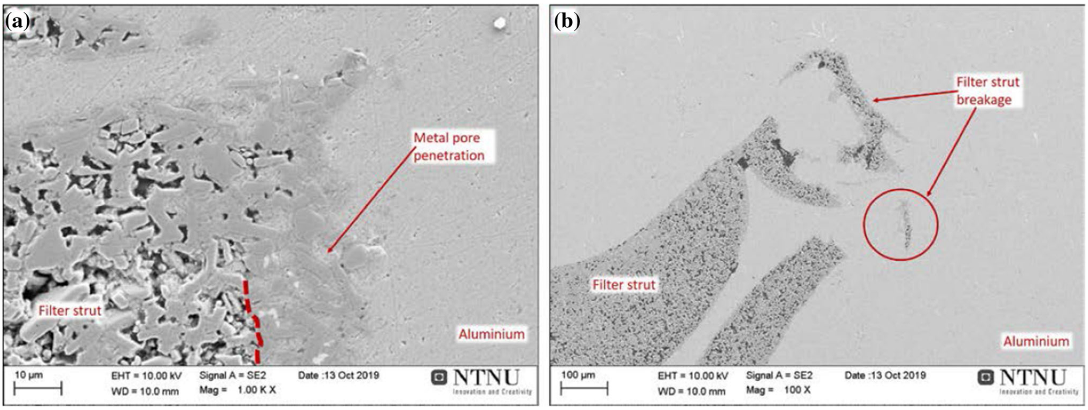

Fig. 13—SEM micrographs of the $Al_2O_3 + P1$ filter immersed by the gravity priming procedure in the AlMg2 melt for 120 min. (*a*) Metal penetration into the strut cavities and material pores within the strut, and (*b*) filter strut breakage.

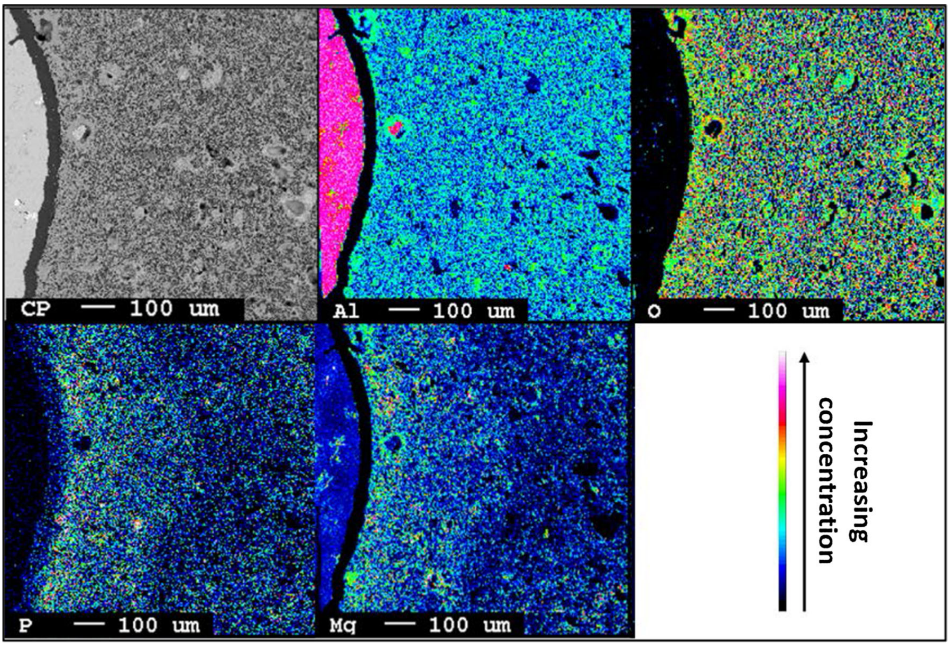

Fig. 14—EPMA mapping of Al, O, P, and Mg for the $Al_2O_3 + P2$ filter immersed by the gravity priming procedure in the AlMg2 melt for 120 min.

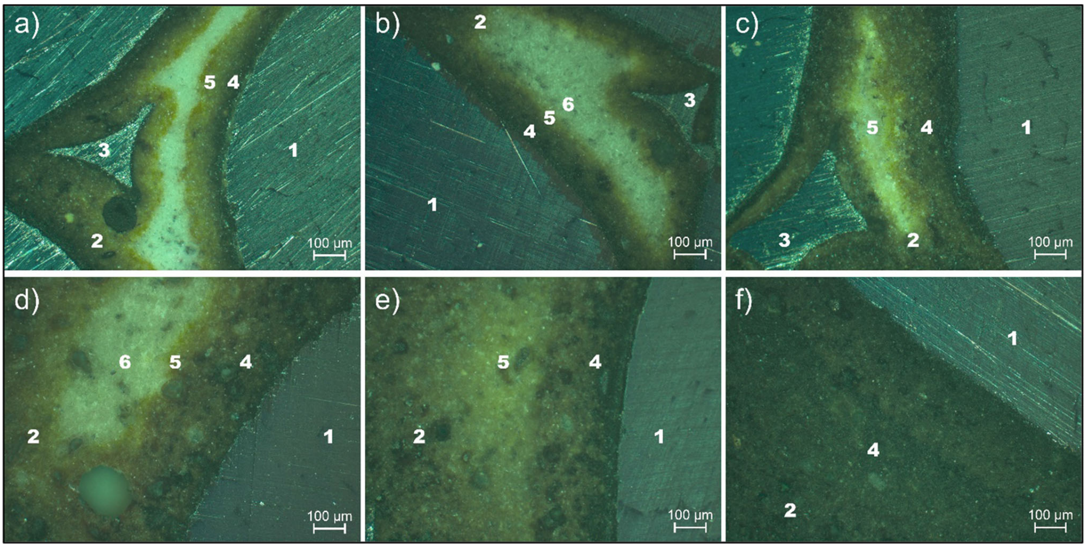

Fig. 15—LOM images at 100× magnification of $Al_2O_3 + P1$ ((*a*) through (*c*)) and $Al_2O_3 + P2$ ((*d*) through (*f*)) filters immersed by the gravity priming procedure in an AlMg2 melt for 30 min ((a) and (d)), 60 min ((*b*) and (*e*)), and 120 min ((c) and (f)). Polarized light and a teal color filter were used, which explains the turquoise color. The numbers in the images mark the following phases/medias: (1) aluminum, (2) filter strut, (3) strut cavity filled with aluminum, (4) fully reacted area, (5) moderately reacted area, and (6) slightly reacted area (Color figure online).

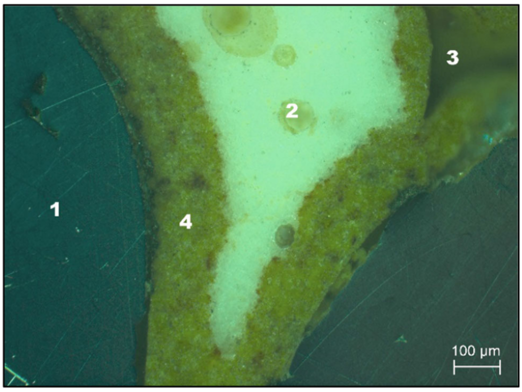

Fig. 16—LOM image at 100× magnification of the Al_2O_3 + P1 filter immersed with electromagnetic priming for 120 min in the AlMg2 melt. Polarized light and a teal color filter were used, which explains the turquoise color. The numbers in the image marks the following phases/medias: (1) aluminum, (2) filter strut, (3) strut cavity (empty), and (4) moderately reacted area (Color figure online).

filter after 30 minutes, increasing in thickness as a function of time. In the case of the Al_2O_3 + P2 filter (Figure 15(d) through (f)), the degradation of the binder seems to have progressed faster, and a thicker discolored layer was established to have formed at the edge of the filter already after 30 minutes. A completely reacted filter was the result after 120 minutes of immersion.

Based on the results from light optical microscopy, electron probe microanalysis, and scanning electron microscopy, it is clear that both phosphate-bonded filters (Al_2O_3 + P1 and Al_2O_3 + P2) have reacted with the AlMg2 melt, affecting the strength of the ceramic structure as a result of binder degradation. It should, however, be noted that the majority of the presented results are images or micrographs, which have the drawback of being methods that opens for subjective analysis. Additionally, filter struts are 3D structures and the plane in which the filter sample is cut can vary between the presented figures, thus potentially affecting the interpretation of the analysis. The advantage, on the other hand, is that all trials within each experimental procedure have been performed in the same manner.

D. *Electromagnetic Priming*

Trials with the Al_2O_3 + P1 and 100pctAl_2O_3 filters immersed in pure aluminum and AlMg2 for 120 minutes were also performed using the electromagnetic priming procedure (a relatively new and innovative procedure allowing the filling of ceramic foam filters with small functional pore sizes without a high metal pressure head [20]). The procedure has the advantages of a low ratio of metal to filter volume, as well as easy access to the aluminum melt during the trial. In other words, samples from the melt that have been in contact with the filter can be collected for further analysis of compositional changes as a result of the filter–metal contact.

Even in this case, no visual degradation could be observed by light optical microscopy in either of the filters immersed in pure aluminum or in the case of the 100pctAl_2O_3 filter immersed in AlMg2. A clear and well-defined color change from milky white to light brown was, however, defined to exist at the edge of the Al_2O_3 + P1 filter and towards the center of the filter strut when immersed in AlMg2, see Figure 16. Following the same pattern as in the gravity priming trials, elements were established to diffuse to and from the filter during immersion in the aluminum melts. The strut cavities were, however, observed to be empty and the filter strut appeared to be less reacted. This is believed to be a direct result of the difference in metal head above the filter needed to initiate priming in the case of the gravity- and electromagnetic procedures, respectively, as well as the lack of molten metal movement within the filter in the case of the electromagnetic procedure.

The chemical composition of the molten metal samples collected during the trials were later analyzed together with samples collected before filter priming, as well as samples from reference trials performed without any filter. For the pure aluminum and the AlMg2 trials, one sample was collected every 30 minutes, and with a total of 12 trials 60 metal samples were analyzed.

The concentrations of P and Mg in the metal samples, *i.e.*, in the samples taken before, during and after the immersion trials, are presented together with the average values and standard deviations for each data set in Figures 17 and 18, respectively. As can be seen from the figures, only minor changes in the concentrations of P and Mg were established to exist for the metal samples secured from the trials with the 100pctAl_2O_3 filters immersed in pure aluminum and in AlMg2. This was also the case for the reference trials. In contrast, the metal samples from the trials with the Al_2O_3 + P1 filters in AlMg2 showed a significant increase of the P concentration from ~ 0.0005 to ~ 0.004 wt pct, as well as a decrease of the Mg concentration from ~ 2.3 to ~ 2.0 wt pct. The large standard deviations obtained for the Al_2O_3 + P1 filters, see Figure 18, are believed to be due to the difference in the initial concentration of Mg in the melt between the trials. It should further be noted that the corresponding results for the trials in pure aluminum was omitted from the figure to ensure graph readability. Unexpectedly, a significant increase in the P concentration also existed for the Al_2O_3 + P1 filters immersed in pure aluminum, *i.e.*, from ~ 0.0005 to ~ 0.0015 wt pct. This is believed to be the result of the initial Mg concentration (0.00035 wt pct as a contaminant) in the pure aluminum, which in turn allowed for a reaction between the filter and the molten metal to take place. P is considered an impurity in aluminum, and even very low amounts would decrease the corrosion resistance and increase the brittleness of the cast metal.[27] It has also been reported that P negatively affects both the formation of eutectic silicon and the eutectic modification using strontium.[28]

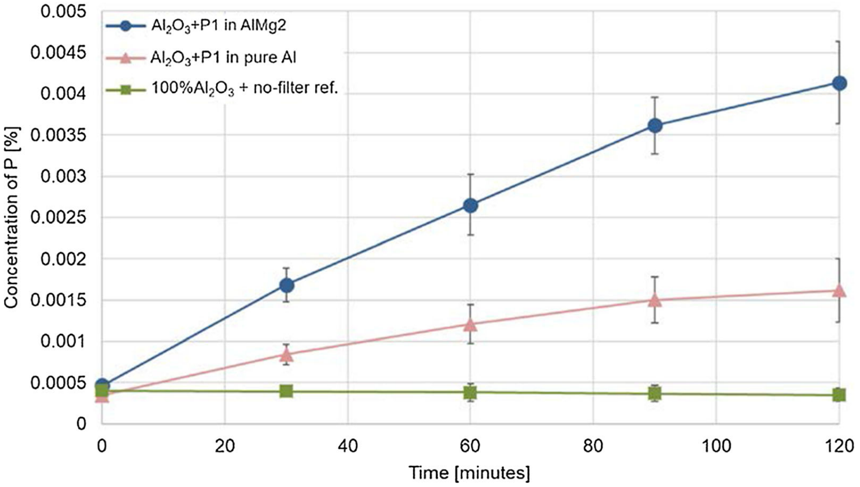

Fig. 17—Concentration of phosphorus (P) in the melt (measured through SOES analysis) as a function of the time the filters were immersed in the molten aluminum. Points are given as an average with standard deviations.

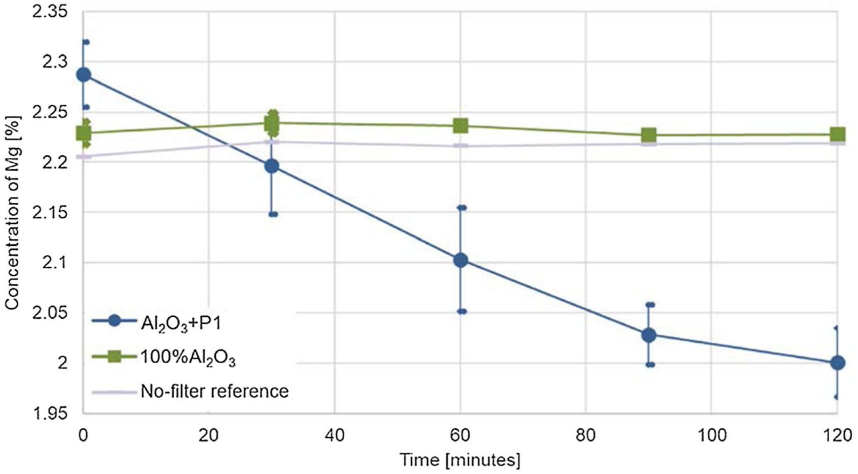

Fig. 18—Concentration of magnesium (Mg) in the melt (measured through SOES analysis) as a function of the time the filters were immersed in the molten aluminum. Points are given as an average with standard deviations.

E. *Release of PH_3 Gas*

During the electromagnetic priming trials, the amount of PH_3 released from the filters immersed in molten metal was measured for each combination of filter and aluminum melt. The filters were allowed to cool for 30 minutes in air at room temperature before the measurement of released PH_3 was performed using a Dräger-Tube® with a measuring sensitivity of 0.1 to 3 ppm. If the first test tube indicated concentrations above 3 ppm, a Dräger-Tube® with a sensitivity of 1 to 100 ppm was used. In each case, the tube was placed just above the filter and held there for 3 minutes or 9 minutes, respectively, depending on the measuring sensitivity of the tube. It should be noted that during the cooling step the filters were only exposed to the

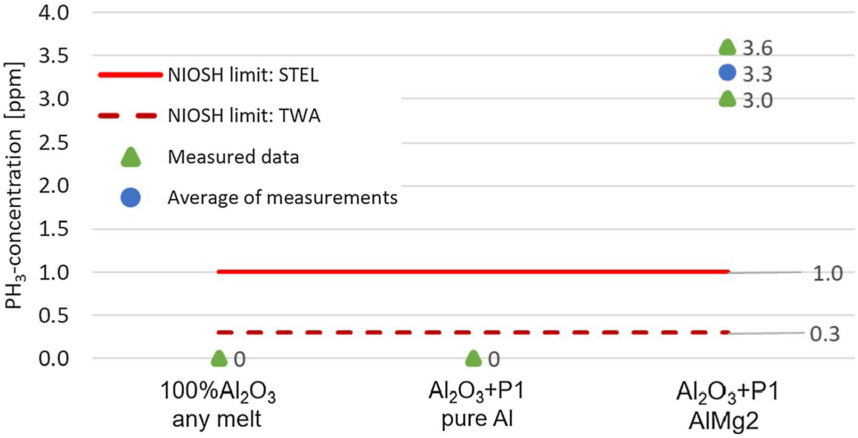

Fig. 19—Measured concentrations of PH_3 gas released from spent filters after cooling in air at room temperature for 30 min, plotted together with the NIOSH's recommended exposure limits.[16]

humidity in the air, where the absolute humidity was in the range of 7.27 to 9.39 g/m^3, which should be similar to what most spent filters are exposed to in an industrial casthouse.

The amount of PH_3 released from the spent filters is presented in Figure 19, together with the National Institute for Occupational Safety and Health's (NIOSH) recommended exposure limits (TWA‡ and STEL§).[16] As can be seen from the figure, no release of PH_3 was measured for the Al_2O_3 + P1 and 100pctAl_2O_3 filters immersed in pure aluminum. However, in the case of the Al_2O_3+P1 filter immersed in AlMg2 the measured average concentration of released PH_3 was 3.3 ppm. This value clearly exceeds the recommended exposure limits of both TWA^4 and STEL^5.[16] Considering that this concentration was measured from a 5 × 5 × 5 cm^3 filter sample while the standard filters used in casthouses today are much larger (typically 60 × 60 × 5 cm^3) is concerning. Despite the mentioned hazardous[15] and flammable[17] nature of PH_3 gas, the actual effect of an Al_2O_3+P1 filter on Health, Safety and Environment in a casthouse has not been documented.

F. *Investigation by Transmission Electron Microscopy*

Due to the fact that a clear increase of the P concentration was established to exist in the molten aluminum samples from the electromagnetic priming trials with Al_2O_3 + P1 filters immersed in pure aluminum, it was decided to look further into possible explanations. As previously mentioned, the pure aluminum that was used in that case contained very small amounts of Mg as a contaminant (0.00035 wt pct), and the overall effect of Mg on the degradation of the $AlPO_4$ binder phase was therefore believed to be important to understand.

One of the Al_2O_3 + P1 filter samples immersed in pure aluminum for 120 minutes during the gravity priming trials was therefore analyzed by transmission electron microscopy, see Figure 20. As can be seen from this cross section from the bulk of the sample, visible changes in the binder phase were observed. Energy-dispersive X-ray microanalysis of the chemical composition of unaffected and affected areas were performed, *i.e.*, on the binder phase between the Al_2O_3 grains (phase 1) which showed either a homogeneous light gray appearance (phase 2) or an inhomogeneous dark gray appearance (phase 3), in which the latter was assumed to be the phosphate binder after it had reacted with Mg. The obtained results for phases 2 and 3, acquired from an area of 0.3 × 0.3 μm^2, are presented in Table V. However, due to the limited precision of the EDS measurements, the tabulated results must be handled with caution.

As displayed in Table V, the unmodified binder (phase 2) consisted of Al, O, and P as expected, where the ratio quite accurately describes the binder to be $AlPO_4$. The reacted binder (phase 3), however, was measured to maintain the same ratio of Al and O, but with a decreased concentration of P. Furthermore, Mg was detected in this phase, which proves that the diffusion of Mg from the melt to the filter had been very strong even if the Mg concentration of the melt was only 0.0016 wt pct (measured by SOES). Furthermore, the established sharp decrease of the P concentration between phases 2 and 3 indicates that P has diffused from the filter into the melt. This could in turn explain the increase in concentration of P observed in the melt during the electromagnetic priming trials with an

---

‡TWA (Time-Weighted Average) is described as the average exposure over an 8-hour period, i.e., a working day

§STEL (Short-Term Exposure Limit) is described as the average exposure over a period of 15 minutes

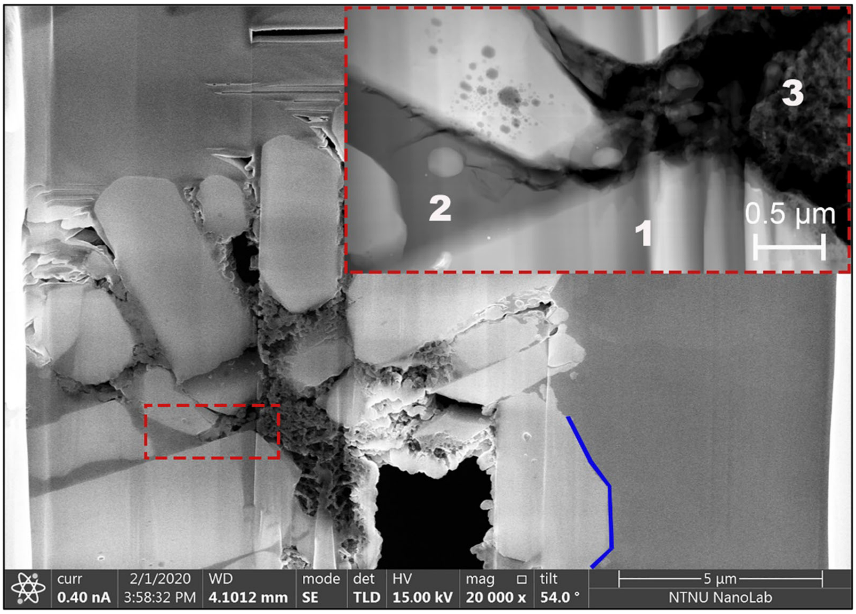

Fig. 20—A cross-section image of the filter–metal interface (marked with a blue solid line) between the $Al_2O_3 + P1$ filter and the pure aluminum. The sample was immersed in the pure aluminum for 120 min during the gravity priming procedure. The present image was retrieved from the bulk of the sample using a FIB, with subsequent element analysis of the following phases (from the section within the red dotted rectangles) using EDS: 1. alumina grains, 2. unmodified binder, and 3. reacted binder (Color figure online).

Table V. The Chemical Analysis of Phase 2 and 3 in Figure 20, Acquired by EDS from an Area of 0.3 × 0.3 μm^2 Using Transmission Electron Microscopy (TEM)

Element	Phase 2 [Weight Percent]	Phase 3 [Weight Percent]
Al	25	25
O	49	52
P	25	7
Mg	0	7

$Al_2O_3 + P1$ filter immersed in pure aluminum, as presented in Figure 17. Thus, the present result proves that reactions will occur between the filter and the aluminum melt even at very low concentrations of Mg.

IV. CONCLUSIONS

Three Al_2O_3-based ceramic foam filters were immersed in pure aluminum with traces of magnesium, as well as in an AlMg2 alloy, using two different experimental priming procedures with subsequent melt and filter analysis. Based on the trials performed, it was concluded that the phosphate-bonded filters ($Al_2O_3 + P1$ and $Al_2O_3 + P2$) suffered from binder degradation upon contact with an aluminum melt containing magnesium. The binder was observed to degrade at a magnesium concentration as low as 0.00035 wt pct, with the severity of the degradation increasing as the concentration of magnesium increased. Even the exposure time proved to have detrimental effect on the filter structure, with pieces of the filter struts breaking off and entering the melt. Clear changes in the melt composition in regard to phosphorus and magnesium were also observed, with an increasing concentration of phosphorus at the boundary layer between the filter and the metal, as well as in the molten metal itself, and an increased concentration of magnesium in the filter with a subsequent decrease in the melt. A clear color change in the filter from milky white to different gradients/shades of brown/black at the interface between the filter and the metal was the result of the chemical reaction between the aluminum melt and the phosphate-bonded filter material with subsequent release of phosphine gas exceeding the recommended exposure limits when in contact with the humidity in the air. Good agreement was established between the thermodynamic calculations performed using FactSage™ and the results of the experimental trials. As no degradation was observed in the case of the $100pctAl_2O_3$ filter, there are strong indications that the degradation and phosphine gas formation was caused by the reactions between the phosphate-bonded filter material and the magnesium containing aluminum melt.

ACKNOWLEDGMENTS

The authors would like to thank the Research Council of Norway (NFR projectnr: 284090) and the German Research Foundation (DFG) for supporting the present study as part of the Collaborative Research Centre 920 “Multi-Functional Filters for Metal Melt Filtration—A Contribution towards Zero Defect Materials.” (Project-ID 169148856) subprojects A02. Furthermore, the authors would also like to acknowledge the support of Norsk Hydro ASA, the SELEE® Corporation, and the Department of Materials Science and Engineering at the Norwegian University of Science and Technology (NTNU).

FUNDING

Open access funding provided by NTNU Norwegian University of Science and Technology (incl St. Olavs Hospital - Trondheim University Hospital).

REFERENCES

1. K. Schwartzwalder and A.V. Somers: U.S. Patent No. 3 090 094A, United States Patent Office, 1963.
2. The Free Library: American Foundry Society Inc.: History of Ceramic Foam Filtration. (Aluminum Silver Anniversary Paper)., https://www.thefreelibrary.com/History+of+Ceramic+Foam+Filtration.+(Aluminum+Silver+Anniversary...-a0103795701, (accessed 18 September 2019).
3. M.J. Pryor and T.J. Gray: U.S. Patent No. 3 947 363A, United States Patent Office, 1976.
4. J.C. Yarwood, J.E. Dore, and R.K. Preuss: U.S. Patent No. 3 962 081A, United States Patent Office, 1976.
5. J.W. Brockmeyer: U.S. Patent No. 4 343 704, United States Patent Office, 1982.
6. D.C. Chesonis: *TMS Light Met.*, 2017, pp. 1411–18.
7. H. Salmang and H. Scholze: 7th edn., Springer, 2007, p. 784.
8. A. Nishikawa: Plibrico Japan Company Limited, Tokyo, Japan, 1984, p. 109.
9. A.S. Wagh: 2nd edn., Elsevier, 2016, pp. 141–42.
10. A.P. Luz, M.A.L. Braulio, and V.C. Pandolfelli: 1st edn., Göller Verlag GmbH, 2015, pp. 214–16.
11. S. Schaafhausen, E. Yazhenskikh, A. Walch, S. Heidenreich, and M. Müller: *J. Eur. Ceram. Soc.*, 2013, vol. 33, pp. 3301–12.
12. L.S. Aubrey, R. Olson, and D.D. Smith: *Mater. Sci. Forum*, 2009, vol. 630, pp. 137–46.
13. C.K.W. Solem, R. Fritzsch, and R.E. Aune: in *Extraction*, The Minerals, Metals & Materials Society, 2018, pp. 1153–63.
14. D.A. Doutre: *TMS Light Met.*, 2010, pp. 797–800.
15. European Parliament and of the Council of the European Union: *Regulation (EC) No 1272/2008*, 2008.
16. National Institute for Occupational Safety and Health: Phosphine - Immediately Dangerous to Life or Health Concentrations (IDLH), https://www.cdc.gov/niosh/idlh/7803512.html, Accessed 17 September 2019.
17. Linde: Säkerhetsdatablad, https://www.linde-gas.se/sv/images/Fosfin_1.1_SE_tcm586-443518.pdf, Accessed 4 January 2021.
18. K. Sreenivasarao, F. Patsiogiannis, and J.N. Hryn: *TMS Light Met.*, 1997, pp. 1153–58.
19. Y. Xiao, M.A. Reuter, and U. Boin: *J. Environ. Sci. Heal.*, 2005, vol. 40, pp. 1861–75.
20. R. Fritzsch, M.W. Kennedy, J.A. Bakken, and R.E. Aune: *TMS Light Met.*, 2013, pp. 973–79.
21. M.W. Kennedy, S. Akhtar, J.A. Bakken, and R.E. Aune: *Metall. Mater. Trans. B*, 2013, pp. 1–15.
22. M.W. Kennedy, S. Akhtar, R. Fritzsch, J.A. Bakken, and R.E. Aune: U.S. Patent No. 9 605 332B2, United States Patent Office, 2017.
23. Norwegian Meteorological Institute: Trondheim, statistics, https://www.yr.no/en/statistics/graph/1-211102/Norway/Trøndelag/Trondheim/Trondheim, Accessed 1 June 2020.
24. L.E. Nevander and B. Elmarsson: *Fukthandbok: Praktik Och Teori*, Svensk byggtjänst, Solna, 1994.
25. Drägerwerk AG & Co: Dräger-Tubes® for short-term measurements, https://www.draeger.com/en-us_us/Applications/Products/Portable-Gas-Detection/Gas-Detection-Tubes/Tubes/Short-term-Tubes, Accessed 12 December 2019.
26. C. Voigt, J. Hubálková, L. Ditscherlein, R. Ditscherlein, U. Peuker, H. Giesche, and C.G. Aneziris: *Ceram. Int.*, 2018, vol. 44, pp. 22963–75.
27. E. Haugland, G.M. Haarberg, E. Thisted, and J. Thonstad: in *Essential Readings in Light Metals: Volume 2 Aluminum Reduction Technology*, G. Bearne, M. Dupuis, and G. Tarcy, eds., Springer International Publishing, Cham, 2016, pp. 229–33.
28. J.H. Kim, I.S. Kwon, K.M. Kim, C.H. Lee, and E.P. Yoon: *Mater. Sci. Technol.*, 2000, vol. 16, pp. 243–48.

Paper 2

Silicon Depletion from Ceramic Foam Filters (CFFs) during Aluminium Melt Filtration in a Pilot-Scale Setup

Are Bergin[1 2], Robert Fritzsch[1], Shahid Akhtar[3], Lars Arnberg[1] and Ragnhild E. Aune[1]

[1]Dept. of Materials Science and Engineering, Norwegian University of Science and Technology (NTNU), Alfred Getz vei 2, 7034 Trondheim, NORWAY

[2]Hydro Aluminium AS, Commercial Technology, Romsdalsvegen 1, 6600 Sunndalsøra, NORWAY

[3]Hydro Aluminium AS, Karmøy Primary Production, 4265 Håvik, NORWAY

Communicating author: Are Bergin (are.bergin@hydro.com / are.bergin@ntnu.no)

Abstract

A series of pilot-scale aluminium melt filtration trials have been performed, using a 6082-alloy and different types of ceramic foam filters (CFFs). Results from energy-dispersive X-ray microanalysis (EDS) on a commercial filter, based on sintered alumina (Al_2O_3) and silica (SiO_2), showed indications of silicon depletion upon a comparison between new- and spent filter samples.

This manuscript is not included and has been published in Light Metals 2024
https://doi.org/10.1007/978-3-031-50308-5_120

---

[1] Health, Safety and Environment

Paper 3

Compression Testing of Ceramic Foam Filters (CFFs) Submerged in Aluminium at Operating Temperature

Are Bergin, Robert Fritzsch, Shahid Akhtar, Lars Arnberg, and Ragnhild E. Aune

Abstract

Particles and inclusions are commonly removed from molten aluminium with the use of Ceramic Foam Filters (CFF). The mechanical properties of CFFs are of great importance not only during transportation, storage, and mounting, ut also in view of securing the integrity of the filters during operation. Data on the compression strength of CFFs at room temperature are available in the literature, but this is not the case for their performance under operating conditions. The main aim of the present study has therefore been to develop an experimental procedure enabling compression testing of CFFs submerged in molten aluminium at operating temperature, i.e. when exposed to actual casthouse conditions. The effect of temperature and holding time was investigated with tests performed at room temperature, at operating temperature with varying duration of filter sample preheating and submerged in molten aluminium. The developed procedure for the measurement of the compression strength for samples submerged in aluminium showed realistic and reproducible data in comparison with previous studies and testing at room temperature. The filter tested was a commercial 30 ppi Al_2O_3-based CFF, which as expected revealed a significant decrease in compression strength for the filter samples submerged in aluminium. The weakened structure of the ceramic foam is believed to be due to a reaction occurring between the CFF and the molten aluminium. Additionally, the exposed filter samples also exhibited a less brittle behaviour compared to the unexposed samples, indicating that even a softening of the ceramic structure had taken place.

Keywords

Filtration • Ceramic foam filters (CFFs) • Mechanical strength • Compression strength • Cracking

Introduction

Ceramic foams exist in numerous shapes and compositions depending on the application, and one example is filtration media during molten metal filtration. Ceramic Foam Filters (CFFs) are usually produced using the replica method patented by Schwartzwalder et al. [1], where polyurethane foam is coated with a ceramic slurry with subsequent sintering. In the sintering step, the polyurethane foam is decomposed leaving a ceramic foam replicating the polymer foam. The remaining ceramic structure is a network of struts and pores/cells, where the former are circular beams that are hollow and holds the network together while the pores/cells are holes or half-spheres allowing the molten metal to flow through. An important filtration parameter is the functional pore size of the CFFs specified by the producer in ppi (pores per inch) or grades. The higher the ppi number, the smaller are the functional pores which result in a higher filtration efficiency [2]. During handling and filtration, the CFFs have to withstand mechanical and thermomechanical stresses. In order to make predictions about the suitability of a special filter and as quality control, the compression strength of the CFFs can be tested.

During compression testing of foams, Ashby describes the resulting stress–strain curves having three regions, *i.e.* linear elasticity, collapse, and densification [3]. The linear elasticity occurs at low strains and is described by bending

A. Bergin (✉) · R. Fritzsch · L. Arnberg · R. E. Aune
Department of Materials Science and Engineering, Norwegian University of Science and Technology (NTNU), Trondheim, Norway
e-mail: are.bergin@hydro.com; are.bergin@ntnu.no

A. Bergin
Research and Technology Development, Hydro Aluminium AS, Sunndalsøra, Norway

S. Akhtar
Karmøy Primary Production, Hydro Aluminium AS, Håvik, Norway

L. Perander (ed.), *Light Metals 2021*, The Minerals, Metals & Materials Series,
https://doi.org/10.1007/978-3-030-65396-5_104

of cell walls and struts, which is followed by the collapse described to occur at almost constant stress (a plateau) and is where the cell walls and struts fracture. These two regions were also described experimentally by Meille et al. [4] during compression testing of porous alumina samples, while Dam et al. [5] reported that the second region was substantially different and varied significantly between samples during compression of alumina–mullite ceramic foams. Voigt et al. [6] defined overall failure and structural collapse of alumina ceramic foams by a force loss of 70% of the maximum force, and this was confirmed by observations of the foam actually breaking into pieces. This description of overall failure is supported by other authors [5, 7], which describe a load drop due to propagation of macroscopic cracks at the crushing point of cordierite and alumina–mullite ceramic foams. Furthermore, the region of linear elasticity can be reviewed considering previous experimental work, where it has been reported that prior to overall failure there are local failures of single struts occurring [6–9].

According to Ashby [3], the most important aspect considering the structure of foams is the relative density (ρ_{rel}), which is the parameter that the mechanical properties of foams above all else depend on (regardless of if the structure consists of open or closed cells). The relative density is defined as

$$\rho_{\text{rel}}=\frac{\rho_{\text{foam}}}{\rho_{\text{solid}}}, \tag{1}$$

where ρ_{foam} is the density of the entire foam and ρ_{solid} the density of the solid that the foam is constructed from, the latter also being referred to as the material density.

The correlation between the compression strength (σ_{fc}) of a brittle foam and the relative density was proposed by Gibson and Ashby [3, 10] to be as follows:

$$\sigma_{fc} = C \cdot \sigma_{mf} \cdot \left(\frac{\rho_{\text{foam}}}{\rho_{\text{solid}}}\right)^{3/2} \tag{2}$$

where σ_{mf} is the fracture strength of the material by which the foam is constructed and C a constant. The theory of an increasing compression strength with increasing relative density has been proven by numerous researchers [4, 5, 8, 11, 12]. The exponent of the relative density in Eq. (2) however, has been described by Oliveira et al. [7] to vary from 2.2 to 3.6 for different experimental studies.

Interestingly, Ashby states that the effect of defects such as flaws, cracks, and variations in pore size on the compressive fracture of foams, is low [3]. This has, however, been questioned by several researchers [5, 7, 12–14] stating that flaws have a clear detrimental effect on both the strength and the variability of the results. The order of magnitude for the detrimental effect flaws has on the strength of ceramic foams have been described by other authors [7, 13], which also states that larger samples would fail at lower stresses compared to smaller samples as the probability of the larger samples containing pre-existing flaws would be higher. Additionally, Voigt et al. [6] tested CFFs with different homogeneity with regard to the porosity, where the homogenous foams had a difference in porosity between the middle and the outer parts of the foam of 2% and the inhomogeneous of 19%, and showed that the compression strength of the homogeneous filters were 3–4 times higher than that of the inhomogeneous filters.

Flaws and cracks will necessarily occur in struts due to the shrinkage during sintering. Additionally, in mechanical models, the struts are often assumed to possess the same properties as the bulk solid without being hollow. Dam et al. [5] confirmed through observations that foam fracture occurred either as a transverse failure of struts or longitudinal strut splitting, suggesting that a more detailed view of the struts (than described in Eq. (2)) is important. Brezny et al. [14] proposed a relationship for the calculation of strut strength (σ_{sf}) through measurements of the struts outer and inner (hollow strut centre) dimensions, as well as the load at strut fracture for high purity alumina and alumina–10% zirconia ceramic foams:

$$\sigma_{sf} = \frac{36 \cdot P \cdot L \cdot D}{9 \cdot \pi \cdot D^4 - 16 \cdot b \cdot h^3}, \tag{3}$$

where P is the fracture load, L the strut length, D the strut outside diameter, while b and h are the base and height of the hollow strut centre which is triangular. The results presented by Brezny et al. [14] showed that the strut dimensions remained constant regardless of an increase in foam density, as higher additions of solids lead to the formation of cell faces and closed pores, and thus a constant strut strength was obtained even with changes in the density of the ceramic foam. The concept of constant strut diameter with increasing relative densities was further supported by Brezny et al. [13] for alumina and alumina–10% zirconia foams, and later by Dam et al. [5] for an alumina–mullite ceramic foam. The observed independence of strut size on density is, however, not to be mistaken for an independence of strut size on pore size, as a decrease in the ppi does increase the length and thickness of the struts as measured by Brezny et al.[15].

Based on the finite element method Voigt et al. [6] performed calculations of the stress distribution of ceramic foams between loading plates, and reported stress peaks in close proximity to the loading plates, suggesting that failure would occur there. It was further assumed that for an increase in pore size, the mentioned stress peaks would be reduced, leading to a homogenous stress distribution where failure was just as likely through the whole thickness of the foam rather than only at the layers closest to the loading plates. In a later in situ experimental study by Hubálková et al.[9], X-ray microtomography was used to carefully study compression testing of alumina ceramic foams, and it was observed that the failure occurred close to the loading plates. This was explained as an obvious phenomenon as the struts in contact with the loading plates would be exposed to a force five times higher than the applied compression stress when the porosity of the tested foams was 80%.

Voigt et al. [6] conducted an extensive study on how different parameters influenced the compressive strength during testing of porous alumina ceramic foams. Amongst other things, they reported that an increase in the foam compression strength was obtained as a result of an increase in sample size and a decrease in the size of the loading plates. The latter can be explained by a failure mechanism described by Gibson et al. [10], where they propose that there is a linear dependence between the compression strength and the square root of the loaded area. The experimental observations by Voigt et al. [6] were further supported by simulations using the finite element method (Abaqus). An increasing compression strength with increasing sample size was also reported by Heness et al. [16] in an experimental study on porous ceramic insulating bricks consisting mainly of alumina and silica. This contradicts the previously described assumption that larger samples would have lower strength due to a higher probability of flaws in the structure. This implies that compression strength values for ceramic foams cannot be directly compared, except if the sample shape and size, as well as the loaded area, are identical. Additionally, it was reported by Voigt et al. [6] that there was very little or no effect on the rate of applied load on the compression strength of ceramic foams.

It should be noted that in regard to the effect of the pore size on the compression strength of ceramic foams, *i.e.* of the ppi/grade in the case of CFFs , there is no clear trend described in literature. According to Oliveira et al. [7], an increase in the mechanical strength of the ceramic foam will be the result of reduced porosity which can be explained by an overall reduction of the pore size. Experimental observations made by other researchers have, however, shown an inconsistent connection where an increase in pore size has been described to decrease the compression strength by some researchers [4, 15] and increase the compression strength by others [5], while Voigt et al. [6] observed small differences without a specific trend.

There is limited literature on compression strength of ceramic foams at elevated temperatures. Goretta et al. [11], however, performed an experimental study on alumina ceramic foams in air at room temperature and at temperatures between 800 °C and 1500 °C by equilibrating the samples at test temperatures for 30 min. The compression strength was reported to be similar to room temperature at 800 °C, increase at 900 °C, and then again to be similar to room temperature in the interval 1000–1200 °C, and then finally decreasing again at temperatures >1200 °C. The results were explained by the fact that alumina consists of a glassy phase that increases in strength at 900 °C as a result of glass softening that covers the flaws in the ceramic structure, while the decrease in strength >1200 °C is an effect of further glass softening that would decrease the viscosity of the glassy phase.

Similar to the limited amount of literature available at elevated temperatures for CFFs, there are no studies investigating the compression strength at operating conditions, *i.e.* in contact with molten metal. As it potentially could be large differences in the filter strength in air at elevated temperatures compared to in contact with molten metal at operating temperatures, the present study aims at developing an experimental procedure enabling compression testing of CFFs at operating temperature and submerged in molten aluminium securing reproducible results. The outcome of the study is believed to be of significant importance for both CFF suppliers, as well as aluminium producers.

Experimental Procedures and Materials

Characterisation of the Ceramic Foam Filter (CFF)

All tested samples were retrieved from the same filter type, which was an Al_2O_3-based CFF with a pore size of 30 ppi supplied by Pyrotek Sivex (Czech Republic). The filter was characterised as-received by an Ultra 55 LE (Zeiss, Germany) scanning electron microscope (SEM), and analysis of the chemical composition was secured by using an XFlash Detector 4010 (Bruker AXS, Germany) energy-dispersive X-ray microanalysis unit (EDS). In addition, measurements of the filter porosity were obtained using an Autopore 5 (Micromeritics, USA) mercury intrusion porosimetry unit (MIP), and of the strut, thickness using a VHX-2000 digital microscope (Keyence, Japan).

The chemical composition presented for the samples is the average of seven measurements at a size of $\sim 200 \times 200$ μm^2 using an accelerating voltage of 20 kV and a 10 mm working distance. The mercury intrusion porosimetry was performed using a penetrometer with a cup volume of 15 cm^3 and a stem volume of 0.392 cm^3 which enabled analysis of relatively large samples ($>10 \times 10 \times 10$ mm^3). A total of 295 measuring points ranging between 0.15 MPa and 420 MPa and an equilibrium time of 5 s were used. The measured pressure (p) was converted into the corresponding pore radius (r) with the help of Washburn's equation:

$$p = (2 \cdot \gamma \cdot \cos\theta)/r, \tag{4}$$

where θ is the contact angle and γ the surface tension of mercury. In the present case, $\theta = 140°$ and $\gamma = 0.485$ Nm^{-1} was used.

Compression Testing of Filter Samples

Room Tempered and Heated Filter Samples

Cylindrical samples with a diameter of ~ 50 mm were cut from commercial size filters with a thickness of 50 mm, using a diamond bit core drill with water as the cooling medium. After cutting the filter samples were dried at 100 °C overnight, with subsequent measurements of the exact dimensions and weight enabling calculations of the foam density of the sample. The compression testing was performed using an 880 Hydraulic Tensile Testing Machine (MTS, USA) with 50 mm diameter pistons as seen in Fig. 1a, at 2 mm/min compression speed. Trials were run until the first peak in applied load was registered, as that was decided to represent a total failure of the foam as in earlier studies performed by other researchers [4–9]. The compression strength was calculated by using the following relationship:

$$\sigma_{fc} = \frac{\mathrm{F_{max}}}{\mathrm{A}}, \tag{5}$$

where F_{max} represents the peak load and A the loaded area.

The effect of temperature and holding time was initially investigated, with testing at room temperature and later at operating temperature with varying duration of sample preheating, see.

Table 1 The number of tests performed per holding time at operating temperature is also included in the table.

For the compression testing at operating temperature, the filter samples were heated in a resistance furnace at 800 °C prior to testing, see Fig. 1b. The temperature development within the filter samples was measured by the use of a K-type thermocouple in four different filter samples, see Fig. 1c. It was established that the samples reached a temperature of 800 °C after ~ 8 min in the furnace, meaning that the samples with the shortest holding time (10 min) would have just reached 800 °C upon retrieval. Furthermore, the temperature decreased quite rapidly in air after retrieval from the furnace, which resulted in a sample temperature of ~ 730 °C at compression.

Filter Samples Submerged in Molten Aluminium

Achieving submersion of CFFs in aluminium, which includes complete soaking of the filter to simulate the flow of aluminium through the filter, is a complicated process that requires an outer force pushing the molten metal into the pores of the filter and thereby priming the filter.

In the present study, an electromagnetic field of ~ 0.2 T (measured in the centre of an empty coil with a Hall Effect gauss meter, model 6010 by Pacific Scientific OECO, F.W. Bell®, USA), generated by a double-layered water-cooled copper coil, was used to submerge the samples in aluminium and thereby securing that the molten metal had entered into every pore of the filter sample. The coil, positioned around the molten metal bath and the filter sample, was connected to a step-down power transformer (230/30-26-21-17-15 V at 45 kVAr) delivering a nominal voltage of 28 V and a current of 747A at the used power ratio (230/30 V). The experimental priming set-up is based on patented technology developed at the lab of the Department of Materials Science and Engineering, Norwegian University of Science and Technology (NTNU) [2, 17, 18].

The preheated filter samples were submerged separately in ~ 550 g of pure molten aluminium (99.8 wt-% Al) at ~ 750 °C. Although full submersion was achieved almost instantly, the electromagnetic field was applied for 5 min for

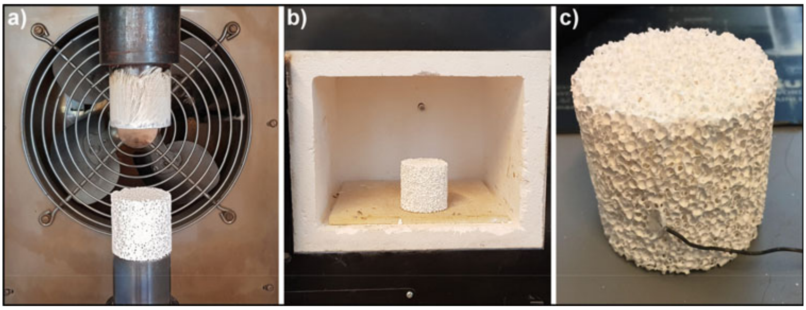

Fig. 1 Images from the experimental procedure at room temperature, as well as at operating temperature where **(a)** shows the compression test apparatus with a filter sample between the pistons, **(b)** a filter sample in the furnace used to heat the samples to 800 °C, and **(c)** how the thermocopuple was pierced into a filter sample to measure the temperature development. (Color figure online)

Table 1 Experimental variations for the compression tests performed at both room- and operating temperatures for aluminium filtration

Testing condition	Room temperature	Operating temperature		
Temperature at the start of the test	25 °C	730 °C	730 °C	730 °C
Duration of heating	–	10 min	1 h	2 h
Number of samples tested	22	10	10	10

all samples. Melt solidification, with the filter samples fully submerged in the aluminium as seen in Fig. 2a, occurred seconds after the electromagnetic field was turned off. A longer priming duration would have required extra measures such as insulation to avoid premature solidification, due to the low amount of molten metal.

The main difference between the compression tests performed at room temperature and those performed on preheated filters, was the use of a sample holder allowing the testing of the submerged filters as can be seen in Fig. 2b, c. The sample holder was made from a welded steel container specifically designed for the purpose, with a groove to fit on top of the bottom piston in the MTS 880 unit and a container to hold the aluminium melt. Additionally, the inside of the holder was filled with MASTIC 85 refractory ceramic fibres (Pyrotek® Inc., USA) to perfectly fit the shape of the primed metal sample, and then coated with boron nitride (BN) on the surface. The metal sample and the sample holder were put into the resistance furnace at 750 °C and left there until the metal was melted and the desired temperature reached, see Fig. 2b. The aluminium melt was then skimmed just before initiating the compression test. The compression rate was 2 mm/min, which was the condition used for all the tests regardless of test temperature until melt solidification (represented by a sample post-compression in Fig. 2d). Additionally, a reference test with only pure aluminium was performed using the same procedure as described above, skipping the filter priming step and instead of melting only aluminium in the sample holder directly.

Results and Discussion

As-Received Filter Characterisation

The chemical analysis of the filter using energy-dispersive X-ray microanalysis (the limited accuracy of this method should be noted), indicated that it is alumina-based (Al_2O_3) as expected with low amounts of phosphorus (P) and silicon (Si). Observations using scanning electron microscopy revealed a relatively dense microstructure consisting of tiny pores evenly distributed within the struts. Additionally, large triangular holes in the strut centres where the polyurethane skeleton had been before being burned off was observed, presented by the white arrows in Fig. 3. Further observations were a few unevenly distributed larger pores observed in the struts, pointed out by the blue arrows in Fig. 3, as well as a variation in size of the triangular holes. All the observed porosity can directly be correlated to what was described as pre-existing flaws in the literature, while the variation in size of the triangular holes can also be an effect of where the filters were cut before analysis.

The densities of the cut and tested filter samples are presented in Table 2. The foam density is based on the measured macro-dimensions and the weight of each sample, while the material density was measured on representative pieces of the filter samples with the use of a mercury intrusion porosimetry unit. The measured values for the material density were assumed to represent the bulk density

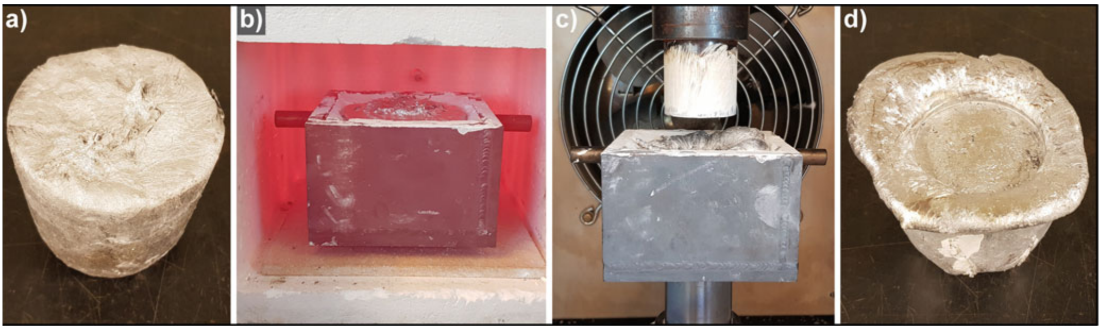

Fig. 2 Images from the experimental procedure of filter samples submerged in molten aluminium, where **(a)** shows the solidifed metal with a primed filter within before testing, **(b)** the sample holder containing the filter sample and molten aluminium in the furnace, **(c)** how the sample holder was set between the pistons, and **(d)** the solidified metal with a filter within after compression. (Color figure online)

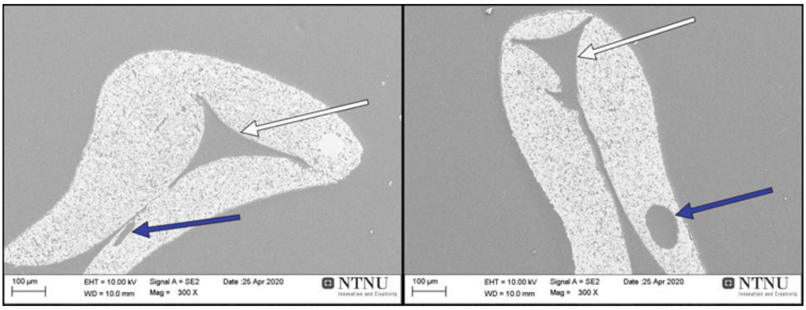

Fig. 3 Scanning electron microscopy images showing the microstructure and apparent porosity of struts in as-received CFFs. The white arrows highlight the hollow strut centres triangular in shape, while the blue arrows highlight large pores that seem randomly distributed. (Color figure online)

of the solid in which the filters were made of. The relative density was calculated by dividing the average foam density with the average material density, and the strut thickness was based on measurements obtained by using a digital microscope. The standard deviations for the different values presented in Table 2 shows that there is some variation in the foam density between the filter samples, but within acceptable limits as the standard deviation is 6.4% of the average value. The standard deviation for the strut thickness is, on the other hand, very large and can be described by a variation in strut size. Furthermore, the average relative density of the filter samples is relatively low given that it for a solid sample would have been 1.

Compression Testing of Filter Samples

Representative load–displacement curves measured during the compression testing of the filter samples (i) at room temperature, (ii) heated with a holding time of 10 min, (iii) submerged in molten aluminium, as well as for (iv) a reference with aluminium only, are presented in Fig. 4. As can be seen from the figure, the curves at room temperature and operating temperature partly bear a resemblance to the two first regions linear elasticity and collapse as proposed by Ashby [3]. There is a sharp linear increase initially that correlates well to the bending of the struts, but there are also several drops in the applied load indicating single struts breaking without an overall failure of the foam, as other researchers have reported earlier [6–9], and thus the region is not elastic. The slope of the linear region of both curves is about 7 kN/mm at an $R^2 > 0.9$, indicating similar behaviour between the two conditions. Foam overall failure and collapse, without a plateau as proposed by Ashby [3], clearly occurs at the curve peak as there is a major drop in the applied load of approximately 95% under both conditions. Thus, the maximum value of the load measured represents the foam's compression strength. It can also be seen from Fig. 4 that a difference in the peak load exists between the samples at room temperature and those at operating temperature, which can be explained by natural variations as only one curve of each is presented. As the slope and shape of both curves are similar, there are no indications that heating filters for 10 min have any impact on their compressive behaviour.

Table 2 Different density properties of the cut filter samples. All values are given as an average, as well as with standard deviations were applicable

Foam density (ρ_{foam}) [g/cm^3]	Material density (ρ_{solid}) [g/cm^3]	Relative density (ρ_{foam} / ρ_{solid})	Strut thickness [µm]
0.40 ± 0.03	2.15 ± 0.02	0.19	291 ± 73

The curve seen in Fig. 4 that represents the filter sample submerged in aluminium is similar in shape to the previous curves, but with an experimental scatter that is both more pronounced and more frequent. The latter could be explained by an increased disturbance at the load cell and thereby increased resistance due to the medium being different than air. The initial linear region of the filter sample submerged in aluminium, is however less steep with a slope of ~1.5 kN/mm at an $R^2 > 0.9$. When comparing the curves obtained for the filter samples at room temperature and at operating temperature, with slopes of ~7 kN/mm, the filter submerged in aluminium exhibit a far less brittle behaviour. Thus, it appears that submerging the filters in aluminium leads to a softening of the ceramic structure.

The peak seen in Fig. 4 on the curve representing the filter sample submerged in aluminium is evident with a subsequent load drop of approximately 80%. This can be correlated to overall foam failure also when compared with results previously reported in literature [6], which set the

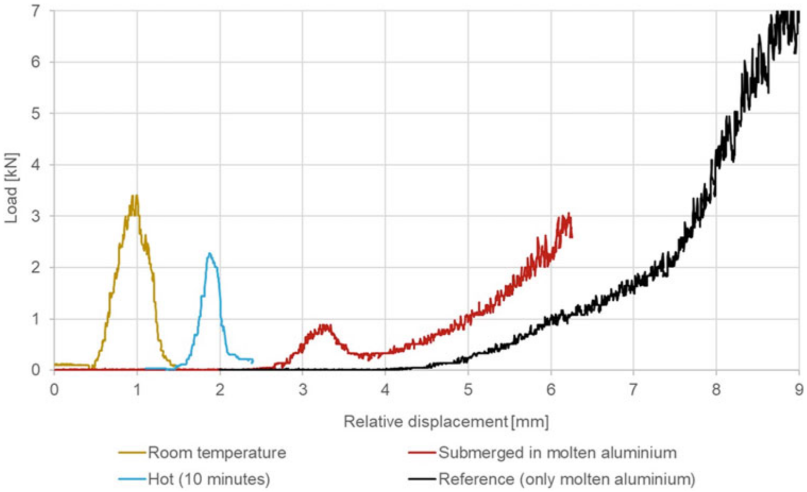

Fig. 4 Representative load–displacement curves for the compression testing of a filter sample (i) at room temperature, (ii) heated with a holding time of 10 minuttes, (iii) submerged in aluminium, and for (iv) a reference with aluminium only (no filter sample). Note the relative displacement on the x-axis, meaning different starting points for different curves, but identical scale. For the two trials in aluminium, there were several mm of displacement prior to an increase in load values

failure criterion to a force loss from the peak value at 70%. The reduction in load drop compared to room temperature can be explained by the molten aluminium starting to solidify, visible by comparing the curve for a filter submerged in aluminium with the reference curve compressing molten aluminium only. As can be seen for the former, there is a sharp increase in the load after foam failure, and the slope of the curve further increases with the relative displacement. The curve of the reference trial with only molten aluminium (no filter sample) can be seen to have a similar shape from the moment of which the solidification starts (after ~80seconds, i.e. 2.6 mm, of displacement at 0 MPa). It can also be seen that there is a change in the slope of the curve where it is linear, which is consistent with the onset of dendrite coherency, followed by a more steep rise where the solidifying aluminium starts to develop a dendritic network that further resists compression [19].

Average compression strength together with the standard deviations for all the tested filter samples (i) at room temperature, (ii) at operating temperature with different holding times, and (iii) submerged in molten aluminium, is presented in Fig. 5. As can be seen from the figure, there are differences between the filter samples tested at room temperature and those tested at 730 °C, but the differences are within the standard deviation. However, a more detailed analysis of the variance based on a null hypothesis that there is no difference between the room temperature values and the operating temperature values, gave a *P*-value of 0.04. Thus, the null hypothesis had to be rejected, which indicates that there is a detrimental effect of the operating temperature at holding times of 1 and 2 h, but not for a holding time of 10 min. This is partly in accordance with a previous study by Goretta et al. [11] who performed testing on a similar material at room temperature and at 800 °C. The study found no difference in compression strength between room temperature and 30 min at 800 °C and described a decrease in compression strength above 1200 °C due to glass softening. It could, however, be that a longer holding time at 800 °C, i.e. 1 and 2 h instead of 30 min, served the same purpose as increasing the temperature further. For the filter samples submerged in molten aluminium, there was a major decrease in the compression strength from in the range of 1.37–1.63 MPa–0.43 MPa, representing a decrease of ~68–73%. Thus, the contact with aluminium has an additional detrimental effect at a higher temperature which can be explained by the corrosive nature of aluminium as it leads to a reaction that weakens the ceramic structure [20]. Another possible explanation is the experimental procedure itself, where the aluminium that the filters were submerged in had to be solidified after priming before being remelted prior to compression testing. Solidification shrinkage might have introduced cracks that could have led to a reduction in the filter's tolerance for compression. This is, however, not the only explanation as the observed decrease in strength was substantial. The decrease can also not be explained by the existing variation in density, as the difference in average relative density between the tests at room temperature and those performed submerged in molten aluminium at operating temperatures was only 1%.

It should be noted that there is a clear variation in the standard deviations observable in Fig. 5, where testing of filter samples at room temperature had a significant standard deviation while testing of filter samples submerged in molten aluminium had a lower standard deviation. A possible explanation is even in this case the softening of the Al_2O_3 glassy phase, as described to occur at higher temperatures by Goretta et al. [11], which at 800 °C might have somewhat

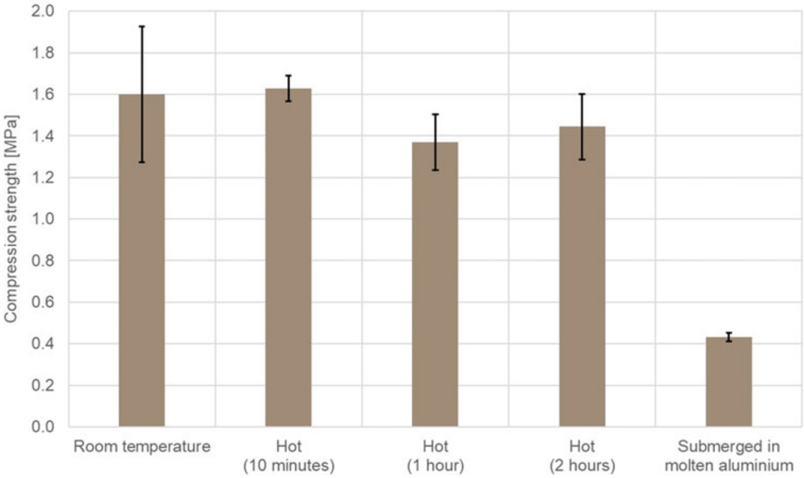

Fig. 5 Average compression strength with accompanying standard deviations from testing of filter samples (i) at room temperature, (ii) at operating temperature (i.e. holding temperature of 800 °C and testing temperature of 730 °C) after heating at different holding times (10 min, 1 h and 2 h), and (iii) submerged in molten aluminium

reduced the number of flaws in the microstructure of the ceramic foam, thus also reducing the standard deviation. In other words, with the presented average compression strengths and standard deviations in Fig. 5, there are clear indications that the developed experimental procedure for testing of CFFs at operating temperature and submerged in molten aluminium show good reproducibility with realistic values.

Conclusions

In an attempt to predict the compression strength of CFFs when exposed to actual casthouse conditions, efforts were made to develop an experimental procedure for compression testing of ceramic foams at operating temperature and submerged in molten aluminium.

The resulting load–displacement curves, compression strengths, and standard deviations from the developed procedures show reasonable and realistic values with good reproducibility in comparison with testing at room temperature and with previously reported studies.

A significant decrease in compression strength was observed for CFF samples submerged in aluminium, likely due to a reaction occurring between aluminium and the CFFs, weakening their structure. A less brittle behaviour and thus a softening of the ceramic structure was also observed for the exposed filter samples compared to the unexposed samples.

Despite the fact that the results reported in the present study are preliminary (more extensive testing is presently being performed), it is believed that filter suppliers should question the relevance of the strength values measured on room tempered filters and therefore develop procedures to measure the actual strength of their filters at operating temperatures while being submerged in molten metal.

Acknowledgements The authors would like to thank the Research Council of Norway (NFR project nr: 284090) and the German Research Foundation (DFG) for supporting these investigations as part of the Collaborative Research Centre 920 “Multi-Functional Filters for Metal Melt Filtration—A Contribution towards Zero Defect Materials” (Project-ID 169148856) subprojects A02. Furthermore, the authors would also like to acknowledge the support of Norsk Hydro ASA and the Department of Materials Science and Engineering at the Norwegian University of Science and Technology. Special thanks are given to Dr. Claudia Voigt for valuable discussions, and Kristoffer Smedal Olsen and Sara Linnea Larsson Grayston for working on this topic in their bachelor’s thesis. Appreciation is also sent to Pyrotek Sivex for supplying the CFFs.

References

1. K. Schwartzwalder, H. Somers, A. V. Somers, Method of Making Porous Ceramic Articles, US 3,090,094, 1963.
2. R. Fritzsch, M.W. Kennedy, J.A. Bakken, R.E. Aune, Electromagnetic Priming of Ceramic Foam Filters (CFF) for Liquid Aluminum Filtration, Light Met. (2013) 973–979. https://doi.org/10.1002/9781118663189.ch165.
3. M.F. Ashby, Mechanical Properties of Cellular Solids., Metall. Trans. A, Phys. Metall. Mater. Sci. 14 A (1983) 1755–1769. https://doi.org/10.1007/BF02645546.
4. S. Meille, M. Lombardi, J. Chevalier, L. Montanaro, Mechanical Properties of Porous Ceramics in Compression: On the Transition Between Elastic, Brittle, and Cellular Behavior, J. Eur. Ceram. Soc. 32 (2012) 3959–3967. https://doi.org/10.1016/j.jeurceramsoc.2012.05.006.
5. C.Q. Dam, R. Brezny, D.J. Green, Compressive Behavior and Deformation-Mode Map of an Open Cell Alumina, J. Mater. Res. 5 (1990) 163–171. https://doi.org/10.1557/JMR.1990.0163.

6. C. Voigt, J. Storm, M. Abendroth, C.G. Aneziris, M. Kuna, J. Hubálková, The Influence of the Measurement Parameters on the Crushing Strength of Reticulated Ceramic Foams, J. Mater. Res. 28 (2013) 2288–2299.
7. F.A.C. Oliveira, S. Dias, M.F. Vaz, J.C. Fernandes, Behaviour of Open-Cell Cordierite Foams under Compression, J. Eur. Ceram. Soc. 26 (2006) 179–186. https://doi.org/10.1016/j.jeurceramsoc.2004.10.008.
8. R. Brezny, D.J. Green, Uniaxial Strength Behavior of Brittle Cellular Materials, J. Am. Ceram. Soc. 76 (1993) 2185–2192. https://doi.org/10.1111/j.1151-2916.1993.tb07753.x.
9. J. Hubálková, C. Voigt, A. Schmidt, K. Moritz, C.G. Aneziris, Comparative Phenomenological Study of Fracture Behavior of Ceramic and Glass Foams under Compressive Stress Using In Situ X-Ray Microtomography, Adv. Eng. Mater. 19 (2017) 1–9. https://doi.org/10.1002/adem.201700286.
10. L.J. Gibson, M.F. Ashby, Cellular Solids: Structure and Properties, 2nd ed., Cambridge University Press, Cambridge, UK, 1997.
11. K.C. Goretta, R. Brezny, C.Q. Dam, D.J. Green, A.R. De Arellano-Lopéz, A. Dominguez-Rodriguez, High Temperature Mechanical Behavior of Porous Open-Cell Al2O3, Mater. Sci. Eng. A. 124 (1990) 151–158. https://doi.org/10.1016/0921-5093(90)90145-S.
12. W. Acchar, F.B.M. Souza, E.G. Ramalho, W.L. Torquato, Mechanical Characterization of Cellular Ceramics, Mater. Sci. Eng. A. 513–514 (2009) 340–343. https://doi.org/10.1016/j.msea.2009.02.012.
13. R. Brezny, D.J. Green, Fracture Behavior of Open-Cell Ceramics, J. Am. Ceram. Soc. 72 (1989) 1145–1152.
14. R. Brezny, D.J. Green, C.Q. Dam, Evaluation of Strut Strength in Open-Cell Ceramics, J. Am. Ceram. Soc. 72 (1989) 885–889. https://doi.org/10.1111/j.1151-2916.1989.tb06239.x.
15. R. Brezny, D.J. Green, The Effect of Cell Size on the Mechanical Behavior of Cellular Materials, Acta Metall. Mater. 38 (1990) 2517–2526. https://doi.org/10.1016/0956-7151(90)90263-G.
16. G. Heness, N. Booth, B. Ben-Nissan, Does Size Matter? - The Effect of Volume on the Compressive Strength of Open Cell Brittle Ceramics, Adv. Mater. Res. 41–42 (2008) 221–226. https://doi.org/10.4028/www.scientific.net/amr.41-42.221.
17. M.W. Kennedy, S. Akhtar, J.A. Bakken, R.E. Aune, Electromagnetically Modified Filtration of Aluminum Melts Part I: Electromagnetic Theory and 30 PPI Ceramic Foam Filter Experimental Results, Metall. Mater. Trans. B. (2013) 1–15. https://doi.org/10.1007/s11663-013-9798-8.
18. M.W. Kennedy, S. Akhtar, R. Fritzsch, J.A. Bakken, R.E. Aune, Apparatus and Method for Priming a Molten Metal Filter, US9605332B2, 2013.
19. G. Chai, L. Baeckerud, L. Arnberg, Study of Dendrite Coherency in Al-Si Alloys During Equiaxed Dendritic Solidification, Zeitschrift Fuer Met. 86 (1995) 54–59.
20. A. Bergin, C. Voigt, R. Fritzsch, S. Akhtar, L. Arnberg, C.G. Aneziris, R.E. Aune, Experimental Study on the Chemical Stability of Phosphate Bonded Al2O3-based Ceramic Foam Filters (CFFs), Submitt. to Metall. Mater. Trans. B. October (2020).

Paper 4

Investigation of Mechanical and Thermo-Mechanical Strength of Ceramic Foam Filters (CFFs)

Are Bergin[1 2], Claudia Voigt[3], Robert Fritzsch[1], Shahid Akhtar[4], Lars Arnberg[1], Christos G. Aneziris[3] and Ragnhild E. Aune[1]

[1]Dept. of Materials Science and Engineering, Norwegian University of Science and Technology (NTNU), Alfred Getz vei 2, 7034 Trondheim, NORWAY

[2]Hydro Aluminium AS, Commercial Technology, Romsdalsvegen 1, 6600 Sunndalsøra, NORWAY

[3]Institute of Ceramics, Refractories and Composite Materials, Technische Universität Bergakademie Freiberg, Agricolastrasse 17, 09599 Freiberg, GERMANY

[4]Hydro Aluminium AS, Karmøy Primary Production, 4265 Håvik, NORWAY

Communicating author: Are Bergin (are.bergin@hydro.com / are.bergin@ntnu.no)

Abstract

During aluminium production, the molten metal will always contain varying amounts of impurities, *e.g.*, non-metallic inclusions, and for high-quality products removing such inclusions is essential. This can be achieved by filtration using ceramic foam filters (CFFs). However, these filters are highly brittle materials subjected to strong mechanical and thermo-mechanical stresses during transport and operation, which occasionally leads to failure of the filter material. In the present study, the compression strength of five different Al_2O_3-based CFFs was measured at room temperature and elevated temperature (compressed at 730 °C), as well as while submerged in molten aluminium with varying melt compositions (pure aluminium and an aluminium-magnesium alloy). The compression strengths at room temperature were established to be in the range of 1.19 – 2.09 MPa depending on the filter type tested. In the case of the CFFs compressed at elevated temperature, a reduction in compression strength in the range of 9.2 – 58.6 % was established to exist depending on filter type and heating duration, except in three of the filter/duration-combinations tested. Compression of CFF samples submerged in molten aluminium led to an even further reduction in compression strength in the range of 42.6 – 69.4 % depending on filter type and duration of exposure. With an exposure time of only 5 minutes, no difference in compression strength was observed between the two aluminium melts.

Keywords: Mechanical properties (C), Thermal properties (C), Strength (C), Chemical properties (C).

This manuscript is not included and has been published in Ceramics International 2022
https://doi.org/10.1016/j.ceramint.2022.10.320 published under a CC BY lisence

Paper 5

Performance of Regular and Modified Ceramic Foam Filters (CFFs) during Aluminium Melt Filtration in a Pilot-Scale Setup

Are Bergin, Claudia Voigt, Robert Fritzsch, Shahid Akhtar,
Lars Arnberg, Christos G. Aneziris, and Ragnhild E. Aune

Abstract

Liquid metal filtration through a ceramic medium has proven to be an efficient way to secure the removal of inclusions and bifilms from molten aluminium. With an increasing focus on recycling of metal values throughout the metallurgical industry, improvements in filter performance and efficiency is currently sought-after but hard to achieve. In the present study, a series of pilot-scale filtration trials have been performed using 30 ppi Ceramic Foam Filters (CFFs) with different surface chemistry and roughness. The trials were carried out with a commercial 6xxx aluminium alloy both with and without additions of grain refiners (AlTi5B1). The filter performance was evaluated by using the change in metal level over the filter to indicate the pressure drop, as well as by analysing LiMCA results. Moreover, microstructural analysis by LOM and SEM/EDX were carried out on spent filters, and current filtration theory used to explain the observed results.

Keywords

Ceramic Foam Filters (CFFs) • Filtration efficiency • Grain refiner • LiMCA

Introduction

Melt cleanliness is an important issue during aluminium production, as non-metallic inclusions lead to a decrease of the mechanical properties and problems during processing of the aluminium, for instance in the case of rolling and surface treatment. Achieving good melt cleanliness is a challenge, and due to the increase of the recycling rate, the purification has and will continue to rise. There are several methods existing for the removal of inclusions, whereby filtration with ceramic foam filters (CFFs) have proven to be a simple and cost-efficient method. However, the performance of ceramic foam filters is not satisfying and improvements in the removal efficiency is desirable.

The mechanisms of inclusion removal using ceramic foam filters have mainly been divided into two modes: deep bed and cake filtration [1]. The two modes are differentiated by where the inclusions are captured, whereby for deep bed filtration this would occur through the whole filter thickness, while for cake filtration inclusions would deposit in the area of the filter entrance and form a filter cake. The formation of a filter cake depends on the size and number of inclusions present and the size of the filter pores, whereby large inclusions and bifilms eventually would cover the filter inlet. Thus, cake filtration is often described to occur with time in opposite to deep bed filtration which always occurs (unless the filter is clogged). Cake filtration is further associated with an increase in removal efficiency as well as pressure drop in contrast to deep bed filtration without cake filtration [1].

One possibility for determining the number of inclusions in an aluminium melt, and thus the removal efficiency, is with the use of a liquid metal cleanliness analyser (LiMCA) [2]. The removal efficiency can be calculated by Eq. (1):

$$\text{Removal efficiency} = \frac{\text{N20}_{\text{Inlet}} - \text{N20}_{\text{Outlet}}}{\text{N20}_{\text{Inlet}}} \cdot 100\% \qquad (1)$$

A. Bergin (✉) · R. Fritzsch · L. Arnberg · R. E. Aune
Depatment of Materials Science and Engineering, Norwegian University of Science and Technology (NTNU), Alfred Getz vei 2, 7034 Trondheim, Norway
e-mail: are.bergin@ntnu.no; are.bergin@hydro.com

A. Bergin
Hydro Aluminium AS, Commercial Technology, Romsdalsvegen 1, 6600 Sunndalsøra, Norway

C. Voigt · C. G. Aneziris
Institute of Ceramics, Refractories and Composite Materials, Technische Universität Bergakademie Freiberg, Agricolastrasse 17, 09599 Freiberg, Germany

S. Akhtar
Hydro Aluminium AS, Karmøy Primary Production, 4265 Håvik, Norway

D. Eskin (ed.), *Light Metals 2022*, The Minerals, Metals & Materials Series,
https://doi.org/10.1007/978-3-030-92529-1_84

where $N20_{Inlet}$ and $N20_{outlet}$ corresponds to the number of inclusions > 20 µm (in thousand inclusions per kilogram melt) before and after the filter, respectively. In general, the performance of ceramic foam filters varies even for filters within the same pore size given in ppi (pores per inch), and for 30 ppi, the removal efficiency has been reported to be in range of 20–90% [3]. The reason for this, is that the removal efficiency is believed to be highly affected by many parameters such as the filter thickness and properties, as well as melt flow rate, melt inclusion level, and inclusion properties [4]. One of the rarely studied parameters is the filter surface chemistry, which will be investigated in the present study. In the continuous casting of aluminium, almost exclusively ceramic foam filters made of alumina are used whereby the alumina is typically phosphate-bonded or phosphate-free. Other tested surface chemistries of filters during continuous casting are silicon carbide (SiC) [5], spinel ($MgAl_2O_4$) [6], mullite ($3Al_2O_3{\cdot}2SiO_2$) [6], and rutile (TiO_2) [6]. According to Syvertsen et al. [5], filtration trials at SAPA Heat Transfer (Finspång, Sweden) showed higher removal efficiencies for the SiC filter compared to the Al_2O_3 filter. Voigt et al. [6] measured for Al_2O_3 and $MgAl_2O_4$ comparable filtration behaviour with removal efficiencies of >95% for inclusions >60 µm. For inclusions <60 µm, the $3Al_2O_3{\cdot}2SiO_2$ filter showed the best removal efficiencies.

The effect of the surface roughness in continuous aluminium casting have also been investigated by Voigt et al. [7, 8]. Alumina filters (of 30 ppi) with varying surface roughness were investigated in a pilot-scale setup at Hydro Aluminium in Bonn, Germany, whereby the rough filters exhibited an improved filtration performance compared to the smoother filters. Carbon-bonded alumina filters (Al_2O_3–C) were investigated by Voigt et al. [8] for mould casting using sand moulds. According to the PoDFA analysis (Porous Disk Filtration Analysis) performed, the Al_2O_3–C filters possessed an improved filtration in comparison with Al_2O_3 reference filters.

The addition of grain refiners into the aluminium melt, prior to the filtration step, has been described to be detrimental to the removal efficiency in many studies [3, 9–11]. This is especially the case when the melt inclusion content is high, while for a clean melt, it has been reported to be insignificant [3, 10]. The detrimental effect of the grain refiner (i.e. the boride particles—TiB_2) has been explained by the destruction or prevention of “bridges” being formed, which are improving the filtration [3, 10, 12].

The objective of the present study has been to investigate the filtration performance of ceramic foam filters with different surface chemistry and roughness, using a pilot-scale setup to replicate industrial conditions. The effect of grain refiner addition on the filter performance was also investigated.

Experimental Procedures and Materials

Six different ceramic foam filter types with 30 ppi were tested in this present study. The filters were symmetric trapeziums with the dimensions ~178 × 178 mm^2 at the inlet/largest side and ~150 × 150 mm^2 at the outlet/smallest side. The thickness varied between 47 and 50 mm. Two of the filters were commercially available, while the non-commercial filters were prepared by the replica technique and a combined dip–spin coating procedure described elsewhere by Voigt et al. [7, 8, 13, 14]. An overview of the different filter types, as well as their nomenclature, can be seen in Table 1.

The study was performed at the Hydro Aluminium R&D facility in Sunndal, Norway, which consists of casting channels arranged in a loop. The aluminium melt was pumped in the loop with the help of a mechanical metal pump as illustrated in Fig. 1. The furnace was filled with approximately 8 tons of melt, consisting of non-fluxed electrolysis metal and alloying elements to produce a 6082 alloy. A new melt was prepared each day, where two consecutive trials were performed with the same melt (there was a ~2-hour delay between trials due to removal of spent filters and heating of new, which likely lead to oxidation of an unknown amount of magnesium between trials). In total, four different melts were prepared and seven filtration trials were performed.

The level of non-metallic inclusion has an influence on the removal efficiency. To reach a comparable level of non-metallic inclusions before the filter, 4 kg of compacted aluminium saw chips were added every 10 min during each trial at position 5, see Fig. 1. An extra addition of 67 kg chips was done towards the end of Trial 7 (Al_2O_3–Carbon), to clearly demonstrate the effect of chips addition on the cleanliness of the melt. To investigate the influence of grain refiner on the filtration, some of the filtration trials were extended. After around 40 min of filtration and LiMCA measurements without grain refiner, AlTi5B1 (Aleastur, Spain) was continuously added (at a pace corresponding to 1 kg/t aluminium given a melt flow rate of 10ton/h) during the following 40 min to measure the removal efficiency with grain refiner. The details of the melts and their additions are summarized in Table 1.

Due to limitations in the producible filter size, a solid ceramic filter adapter was applied in the filter box as can be seen in Fig. 1. Four CFFs of the same type and size were placed together in each corner of the filter box, with the adapter as a cross in between. The challenge of priming, *i.e.* achieving aluminium melt flow through the filters, increases with the use of four filters as compared to one. The Drain-Free Filtration (DFF®) system was used, which enables priming through under-pressure and has been

Table 1 Parameters of the different trials with details about melts and melt additions

Trial	Filter	Filter information	Melt	Addition chips	Addition grain refiner
1	Comm-filter A	Commercial filter of brand A, phosphate free, thickness: 50 mm	Melt 1	4 kg every 10 min	n/a
2	Rough-Al_2O_3 A	Al_2O_3 skeleton coated with Al_2O_3-grains (d_{50} = 33 µm), thickness: 47 mm		4 kg every 10 min	~1 kg AlTi5B1/ton Al
3	Ref-Al_2O_3	Pure Al_2O_3 filter, thickness: 47 mm, used as a reference	Melt 2	4 kg every 10 min	n/a
4	Comm-filter B	Commercial filter of brand B, phosphate free, thickness: 50 mm		4 kg every 10 min	~1 kg AlTi5B1/ton Al
5	Comm-filter A	Commercial filter of brand A, phosphate free, thickness: 50 mm	Melt 3	4 kg every 10 min	n/a
6	Rough-Al_2O_3 B	Al_2O_3 skeleton coated with Al_2O_3-grains (d_{50} = 70 µm), thickness: 47 mm		4 kg every 10 min	~1 kg AlTi5B1/ton Al
7	Al_2O_3–carbon	Al_2O_3 skeleton with a coating of carbon bonded Al_2O_3, thickness: 47 mm	Melt 4	4 kg every 10 min + 67 kg after 34 min	n/a

described elsewhere [9, 15, 16]. The DFF® filter box is equipped with inspection windows making it possible to observe the priming, and although only one of the four filters was visible, the priming was considered successful based on where the melt from the four corners made contact (also, the weight of the spent filters with the solidified aluminium was similar for all four filters within each trial). The average melt temperature at priming was 743 ± 4 °C, and the average filter temperature as measured with a K-type thermocouple in contact with one of the filters right before priming (the thermocouple was removed before the melt entered) was 521 ± 32 °C.

The metal cleanliness was continuously measured with two liquid metal cleanliness analyzers (LiMCA II (ABB Ldt., Canada)), as well as by retrieving porous disc filtration apparatus (PoDFA) samples (the PoDFA results will however not be presented here, but partly in another TMS'22 paper [17]). The sampling positions can be seen in Fig. 1. Two average CFF removal efficiencies were calculated based on the LiMCA N20 values from each trial. Both were based on the average of the calculated removal efficiencies at every LiMCA measuring point, but over different time spans. The "average removal efficiency of stable region" was based on the time span where the LiMCA N20 counts both before and after the CFF were stable, i.e. where the counts were constant within a reasonable scatter. This stable region varied between trials but was typically from around 20 min filtration time until trial end for the short 40 min trials, and around 30–60 min filtration time for the longer trials. The "total removal efficiency" on the other hand was based on the complete trial duration for the 40 min trials, and from the start of the trial until the filtration was affected by the grain refiner additions for the longer trials.

The melt flow rate was taken into consideration so that the measured melt volumes both before and after the filter were approximately the same. This means that for the calculation of the removal efficiency between two measuring points, a delay of approximately 4 min was used between the before- and after-count, i.e. between LiMCA at positions 1 and 2. The metal level in the launder before and after the filter box was measured continuously using lasers. The melt flow rate was calculated by submerging a refractory insert dam with a small opening of a known size into the launder, and measuring the pressure drop over the dam using lasers. This is a method that has previously been experimentally verified at the Hydro R&D facility, and was performed at the end of each trial, where the average melt flow rate was calculated to be 7.1 ± 0.55 ton/h.

All spent filters, with the aluminium solidified within, were cut in two parts for inspection and a piece of 25 × 30 mm^2 (for some trials, the whole filter thickness of ~50 mm) was cut from the same place of one filter per trial for microstructural analysis. After cutting, the samples were embedded in epoxy and polished. Analysis was performed with an Axio Vert.A1 (Zeiss, Germany) light optical microscope (LOM) connected to the ZEN core software (Zeiss) and an Ultra 55 LE scanning electron microscope (SEM) (Zeiss, Germany) equipped with an XFlash 4010 energy-dispersive X-ray microanalysis (EDS) detector (Bruker AXS, Germany).

Results and Discussion

The melt chemistry was measured by spark optical emission spectroscopy (SOES) using an ARL 4460 (Thermo Fischer Scientific, USA). Measurements were secured from two disc

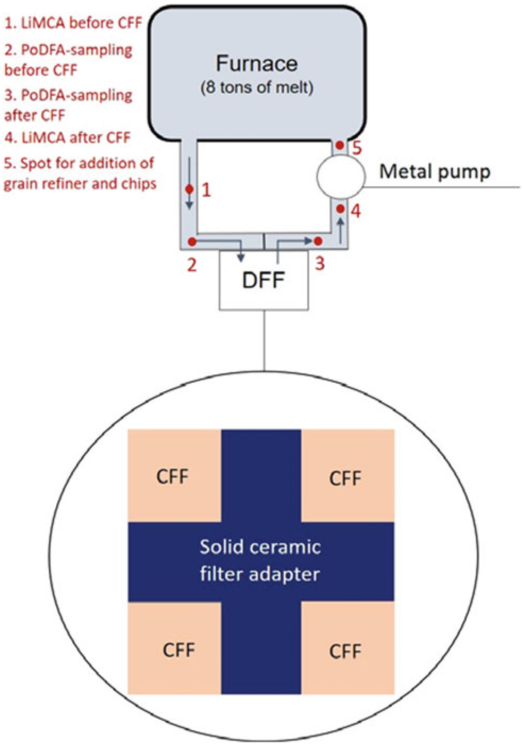

Fig. 1 Illustration of the experimental setup with a furnace filled with 8 tons of aluminium metal, loop, positions of sampling and additions, filter adapter, and metal pump

samples at the start of the first trial, each day. The average alloy concentrations of the main elements from these two measurements are presented in Table 2.

The filters were examined after the filtration trials with LOM, SEM, and EDS whereby a relative clean aluminium melt was observed, with a limited number of detected non-metallic inclusion. The inclusions found consisted mainly of inclusions agglomerated together (clusters) and connected to bifilms of different lengths, see Figs. 2, 3, and 4. According to EDS, the inclusions and bifilms consisted mainly of aluminium, magnesium, and oxygen, which indicated according to other studies [18, 19] the presence of MgO, small spinel particles ($MgAl_2O_4$), and aluminium–magnesium films. Some inclusions show amounts of Si, see Fig. 2, which can be traced to the alloying elements of the aluminium melt. It is important to note that an exact determination of the chemical composition of inclusions is difficult due to the activated volume during EDS measurements, as well as the small size and unknown depth of the inclusions. In Fig. 3, a repeatedly observed intermetallic phase and pores surrounded by bifilms are shown. The pores are possibly formed by entrained air introduced by folded bifilms, or inclusions being removed during sample cutting or polishing. Other inclusions that were commonly observed and identified by comparison with previous studies, were aluminium oxide films [18–21] and large spinels ($MgAl_2O_4$) [19, 21, 22], as well as a few TiB_2 grain refiner particles (bright particles in SEM) [22]. The relatively small number of inclusions and bifilms observed in the spent filters, as well as the distance between them, indicates relatively clean melts.

There was no cake formation observed on any of the filters, and the distribution of clusters and bifilms appeared to be uniform through the whole thickness of the filters. This indicates that deep bed filtration was the dominant mode similarly to what other authors have reported, e.g. by Syvertsen et al. [23] through pilot-scale testing of 65 ppi CFFs (however, cake mode reported for 80 ppi), and by Damoah and Zhang [18] through lab-scale testing of 30 ppi CFFs. However, there were no clear interactions observed between the filters and the clusters/bifilms. In this context it is important to note that these are 2D analyses of 3D structures, and thus there could be interactions in the z-direction. An example of deep bed filtration and an interesting observation can be seen in Fig. 4, which is a micrograph from the very bottom of a filter (Comm-filter A). Two large clusters/bifilms of ~200 µm in diameter are very close to the bottom of the filter and have almost passed the filter. It is possible that metal drainage from the filter post-trial have played a role here (despite the observation is from an area of very little metal drainage), but still the clusters/bifilms must have passed through the whole filter thickness.

The pressure drop measured with lasers positioned before and after the DFF®-box, were low and similar between the 7 different trials. The increase over the whole trial duration were in the range of ~0–4 mm for all trials. This supports the previous observations indicating deep bed filtration as the dominating mode and a relatively clean melt.

Table 2 The average chemical composition [wt%] and standard deviations of the four used melts. The values were measured by SOES prior to the start of the first trial of the day. Only for elements with wt% >0.1

	Si	Fe	Mn	Mg	Al
Melt 1	1.04 ± 0.00	0.22 ± 0.00	0.65 ± 0.00	0.88 ± 0.00	97.21 ± 0.00
Melt 2	1.07 ± 0.00	0.20 ± 0.00	0.65 ± 0.01	0.90 ± 0.00	97.17 ± 0.00
Melt 3	0.97 ± 0.01	0.22 ± 0.00	0.65 ± 0.00	0.93 ± 0.00	97.23 ± 0.01
Melt 4	1.10 ± 0.01	0.19 ± 0.00	0.65 ± 0.00	0.94 ± 0.00	97.08 ± 0.02

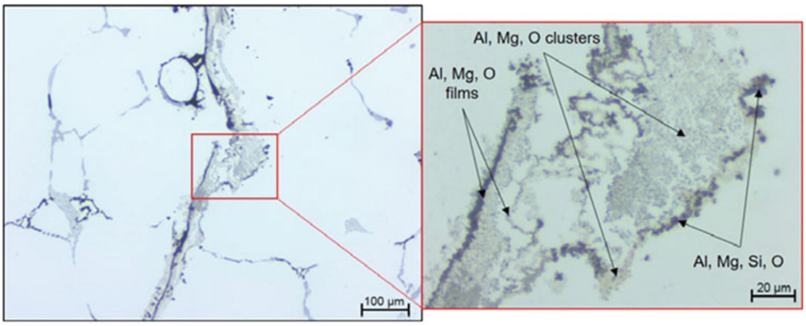

Fig. 2 Inclusion clusters and bifilms, as well as the presence of Si, observed using LOM with an objective lens of ×10 (left) and ×50 (right)

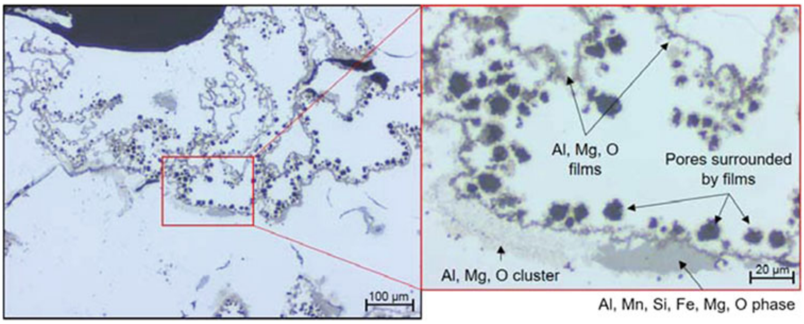

Fig. 3 Inclusion clusters, an intermetallic phase, as well as pores surrounded by bifilms observed using LOM with an objective lens of ×10 (left) and ×50 (right)

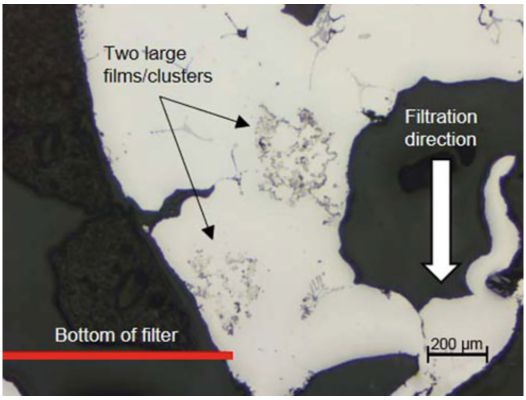

Fig. 4 LOM image (objective lens of ×5) showing two large clusters/bifilms positioned at the very bottom of a filter (Comm-filter A, Trial 1)

Figures 5 and 6 shows the LiMCA N20 values before and after the filter, with the calculated removal efficiencies, for all the trials. The LiMCA counts corresponds to the amount of detected inclusions in thousand inclusions per kilogram of aluminium melt, and N20 means that inclusions between 20 and 320 µm are included. For all trials and through the whole duration of each trial, one can see that the N20 values before the filter are higher than after the filter, demonstrating the cleaning effect of the filters. Furthermore, it is noticeable that the N20 values before the filter decrease significantly at the beginning of each trial, which is an often described behaviour [7, 24, 25] and is caused among other things by the settling of inclusions. The calculated removal efficiencies (Eq. (1)) are relatively stable apart from some outliers, where some are likely caused by PoDFA sampling. Another possible explanation for the N20 outliers is described by Engh [2] with the re-entrainment of inclusions, i.e. inclusions that have been captured by the filter and released into the melt again. It is described as a phenomenon that in general is unlikely to occur, as there is a net reduction in Gibbs energy for an inclusion being restrained at the melt–filter interface. However, it would still be possible as both inclusions and filter have rough surfaces at a microscopic scale so that the actual contact area is significantly lower than it may seem. It should be noted that Trial 2 (Rough-Al_2O_3 A) possessed a larger variation of the removal efficiency as compared to the other trials, starting after 20 min. As this is a rougher filter, the actual contact area as described by Engh [2] would likely be even lower compared to the other filters. However, a rougher filter would also increase the filter interaction area, which might balance the reduction in inclusion–filter contact area. Also, as there were no clear interactions observed between the filters and the clusters/bifilms in any of the trials, it is not believed that this re-entrainment is the explanation behind the many outliers observed in Trial 2 (Rough-Al_2O_3 A).

Despite the application of filters with different properties, the filtration behaviours with regard to the measured N20 values were comparable between the different tested filters. The majority of the removal efficiencies were within the range of 80–100%, indicating good filter performances.

The graphs on the right of Fig. 5 (b, d, f) show the trials with long durations and additions of grain refiner starting after about 40 min filtration time. It is visible that ~10 min after the addition, the N20 values before the filter starts to increase without reaching a stable N20 level. This is interesting, as the grain refiner particles have a particle size distribution in the range of 0.06–7 μm [26], which is far below the detection limit of N20 (measures only sizes >20 μm). It is further visible that the N20 count after the filter increases as well, with a time delay compared to the N20 values before the filter, which causes the calculated removal efficiencies to decrease significantly. This observed decrease in removal efficiency with additions of grain refiner is in accordance with observations made previously by other authors [3, 9–11]. The mechanism causing the decrease in removal efficiency, is in literature often explained by grain refiner particles either breaking "bridges" of oxides and other inclusions, or prevents their formation [3, 10, 12]. The LOM and SEM analyses of the spent filters in the present study showed no bridges in neither of the samples, i.e. not in filters with grain refiner additions nor in filters

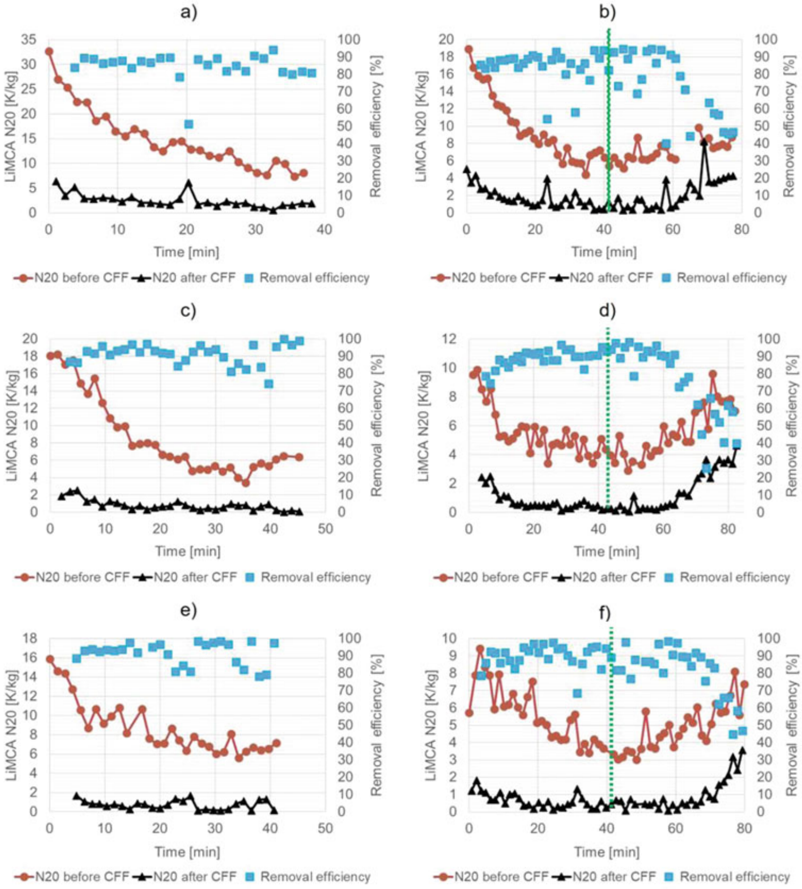

Fig. 5 LiMCA N20 values before and after the filter with calculated removal efficiencies for **a** Trial 1, Melt 1, Comm-filter A; **b** Trial 2, Melt 1, Rough-Al_2O_3 A; **c** Trial 3, Melt 2, Ref-Al_2O_3; **d** Trial 4, Melt 2, Comm-filter B; **e** Trial 5, Melt 3, Comm-filter A; **f** Trial 6, Melt 3, Rough-Al_2O_3 B. (The vertical dotted line in diagrams **b**, **d**, and **f** represents the start of grain refiner addition)

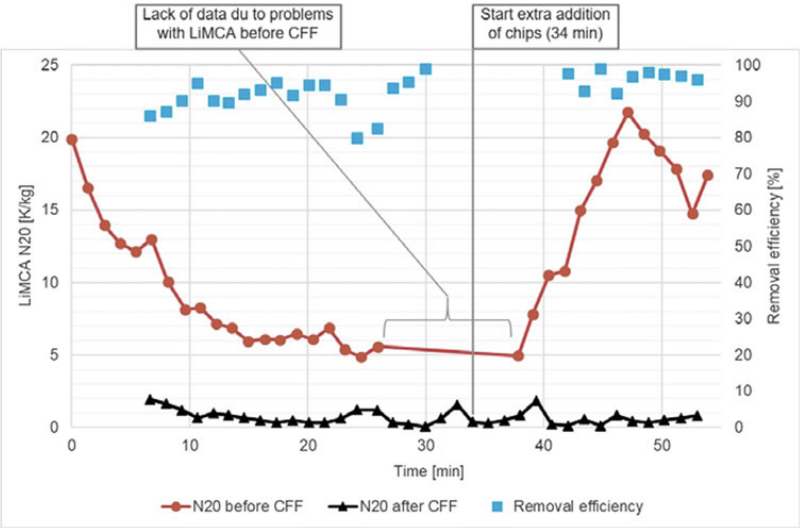

Fig. 6 LiMCA N20 graph showing the inclusion count before and after the CFF, with the calculated removal efficiency for Trial 7 (Melt 4 and Al_2O_3–Carbon). Large amounts (67 kg) of chips were added towards the end of the trial

without grain refiner addition. Furthermore, the detrimental effect of grain refiner additions was observed to be significant in clean melts, which contradicts the studies mentioning a negative effect only for aluminium melts with a high inclusion level [3, 10].

The addition of an extra amount of chips (67 kg) was conducted in Trial 7 (Al_2O_3–Carbon) and is presented in Fig. 6. The additional amounts of chips affected the N20 values before the filter, while a stable low N20 level was measured after the filter. As a result, the removal efficiency proved to be stable with a slight increase. Thus, the decrease in removal efficiency observed when adding grain refiner is not due to a melt heavy in particles, but an effect of the grain refiner.

The average and total removal efficiencies calculated according to the description in Experimental Procedures and Materials-chapter, as well as the maxima and minima of the removal efficiencies, are presented in Table 3. The average and total removal efficiencies are important industrial characteristic values giving indications on the cleaning effect and capacity of a filter during a whole cast.

The average removal efficiencies of a stable region were calculated to be in the range of 83.6–91.7%, and the total removal efficiency in the range of 84.6–92.9%. The

Table 3 Overview of minima, maxima, and average removal calculated with the N20 values before grain refiner additions

	Melt 1	Melt 2	Melt 3	Melt 4
Trial	1	3	5	7
Filter	Comm-filter A	Ref-Al_2O_3	Comm-filter A	Al_2O_3–carbon
Figure	5a	5c	5e	6
Average removal efficiency of stable region [%]	83.6 ± 5.3	90.5 ± 7.1	89.7 ± 7.9	91.7 ± 5.7
Total removal efficiency [%]	84.6 ± 7.7	91.2 ± 5.7	91.3 ± 6.5	92.9 ± 4.7
MIN removal efficiency [%]	51.3	74.1	78.0	79.9
MAX removal efficiency [%]	94.2	100.0	98.5	99.0
Trial	2	4	6	–
Filter	Rough-Al_2O_3 A	Comm-filter B	Rough-Al_2O_3 B	–
Figure	5b	5d	5f	–
Average removal efficiency of stable region [%]	83.6 ± 13.4	91.2 ± 3.9	88.5 ± 6.8	–
Total removal efficiency before grain refiner-addition [%]	84.6 ± 11.1	89.9 ± 5.1	89.0 ± 6.6	–
MIN removal efficiency [%]	40.1	74.6	68.5	–
MAX removal efficiency [%]	94.6	98.3	98.4	–

differences in the removal efficiencies are within the standard deviations, which reveal that the differences are not significant. The calculated removal efficiencies are the upper region of what is expected for 30 ppi filters [3], but they do not show the same improvement in filtration performance as previously reported for rough [7] and carbon bonded filters [8]. However, it should be pointed out that this is an effect of the current experimental parameters, and that further testing would be necessary to obtain further clarification. For instance, it is possible that using 30 ppi filters instead of a finer filter overshadows any effect of the surface roughness or surface chemistry. Furthermore, the filter performances are a result of the inclusion amount and types, melt flow rate, and the use of a filter adapter. It is also possible that the precision in the measurements were not precise enough to capture any differences between the filters.

Conclusions

Ceramic foam filters of 30 ppi from commercial origin, as well as lab-scale production with coatings creating a carbon-bonded alumina surface and a higher surface roughness, were tested in a pilot-scale filtration setup using 8 tons of a 6082 alloy with and without additions of grain refiner. Based on the trials performed, it was concluded that the different ceramic foam filters exhibited similar filtration behaviour. The filter performance of all the filters were good, with total removal efficiencies (averaged over the whole cast prior to grain refiner additions) in the range of 84.6–92.9%. Additions of grain refiner lead to a significant decrease in the filter removal efficiency, even though no “bridges” of oxides/carbides were observed in either of the tests with or without additions of grain refiner. In all cases, deep bed filtration was observed to be the dominant removal mode.

Acknowledgements The authors thank the Research Council of Norway (NFR project nr: 284090), and the German Research Foundation (DFG) for supporting these investigations as part of the Collaborative Research Centre 920 “Multi-Functional Filters for Metal Melt Filtration—A Contribution towards Zero Defect Materials” (Project-ID 169148856) subproject A02. Furthermore, the authors acknowledge the support of Norsk Hydro ASA, all the helpful personnel at the Hydro R&D facility in Sunndal and the Department of Materials Science and Engineering at the Norwegian University of Science and Technology.

References

1. Abel Engh T (1992) Principles of Metal Refining. Oxford University Press Inc., New York
2. ABB (2021) Mobile Liquid Aluminium Cleanliness Analyzer LiMCA III. https://new.abb.com/products/measurement-products/analytical/metallurgical-analyzers/limca-iii. Accessed 23 Aug 2021
3. Keegan N, Ray SF (2003) An Evaluation of Industrial Filtration Systems. Alum Int Today 15(2):21–23
4. Chesonis DC (2017) A Holistic Approach to Molten Metal Cleanliness. Light Metals 2017, 1411–1418
5. Syvertsen M, Kvithyld A, Bao S, Nordmark A, Johansson A (2014) Parallel Laboratory and Industrial Scale Aluminium Filtration Tests with Al2O3 and SiC Based CFF Filters. Light Metals 2014, 1041–1046
6. Voigt C, Jäckel E, Taina F, Zienert T, Salomon A, Wolf G, Aneziris CG, Le Brun P (2017) Filtration Efficiency of Functionalized Ceramic Foam Filters for Aluminum Melt Filtration. Metall Mater Trans B 48:497–505. https://doi.org/10.1007/s11663-016-0869-5
7. Voigt C, Dietrich B, Badowski M, Gorshunova M, Wolf G, Aneziris CG (2019) Impact of the Filter Roughness on the Filtration Efficiency for Aluminum Melt Filtration. Light Metals 2019, 1063–1069
8. Voigt C, Hubálková J, Zienert T, Fankhänel B, Stelter M, Charitos A, Aneziris CG (2020) Aluminum Melt Filtration with Carbon Bonded Alumina Filters. Materials (Basel) 13:1–13
9. Tundal U, Steen I, Strømsvåg Å, Haugen T, Fagerlie JO, Håkonsen A (2019) Drain Free Filtration (DFF) - A New CFF Technology. Light Metals 2019, 1097–1104
10. Towsey N, Schneider W, Krug H-P, Hardman A, Keegan N (2001) The Influence of Grain Refiners on the Efficiency of Ceramic Foam Filters. Light Metals 2001, 291–295
11. Voigt C, Fankhänel B, Dietrich B, Storti E, Badowski M, Gorshunova M, Wolf G, Stelter M, Aneziris CG (2020) Influence of Ceramic Foam Filters with Al2O3 Nanocoating on the Aluminum Filtration Behavior Tested With and Without Grain Refiner. Metall Mater Trans B 51:2371–2380
12. Ray S, Milligan B, Keegan N (2005) Measurement of Filtration Performance, Filtration Theory and Practical Applications of Ceramic Foam Filters. Alum. Cast House Technol.
13. Voigt C, Jäckel E, Aneziris CG, Hubálková J (2013) Investigations of Reticulated Porous Alumina Foam Ceramics Based on Different Coating Techniques with the Aid of µCT and Statistical Characteristics. Ceram Int 39:2415–2422
14. Voigt C, Zienert T, Schubert P, Aneziris CG, Hubálková J (2014) Reticulated Porous Foam Ceramics with Different Surface Chemistries. J Am Ceram Soc 97:2046–2053
15. Tundal U, Steen IK, Haugen T, Fagerlie JO (2016) Apparatus and Method for the Removal of Unwanted Inclusions from Metal Melts. WO 2016/126165 A1.
16. Bao S, Syvertsen M, Syvertsen F, Gihleengen BE, Tundal U, Pettersen T (2019) Laboratory Scale Study of Reverse Priming in Aluminium Filtration. Light Metals 2019, 1105–1111

17. Fritzsch R, Schanche TL, Zedel H, Bergin A, Akhtar S, Arnberg L, Aune RE (2022) Aluminum Melt Cleanliness Analysis based on Direct Comparison of Computationally Segmented PoDFA Samples and LiMCA Results. Light Metals 2022. Pp. XX–XX
18. Damoah LNW, Zhang L (2010) Removal of Inclusions from Aluminum through Filtration. Metall Mater Trans B 41:886–907
19. Birol Y (2010) Survey of Inclusions in Twin Roll Casting of Wrought Aluminium Alloys. Int J Cast Met Res 23:250–255
20. Enright P, Hughes I, Pickering J, Simard A, Proulx J (2003) Characterisation of Molten Metal Quality Using the Pressure Filtration Technique. In: Trans. Am. Foundry Soc. pp 1–11
21. Jaradeh MM, Carlberg T (2011) Method Developed for Quantitative Analysis of Inclusions in Solidified Aluminum Ingots. Metall Mater Trans B 42:121–132
22. Samuel AM, Doty HW, Valtierra S, Samuel FH (2018) Inclusion Measurements in Al–Si Foundry Alloys Using Qualiflash and Prefil Filtration Techniques. Int J Met 12:625–642
23. Syvertsen M, Johansen I, Kvithyld A, Bao S, Eriksen U, Gihleengen BE, Akhtar S, Bergin A, Johansson A (2020) Evaluation of CFF and BPF in Pilot Scale Filtration Tests. Light Metals 2020, 963–971
24. Bao S, Syvertsen M, Nordmark A, Kvithyld A, Engh T, Tangstad M (2013) Plant Scale Investigation of Liquid Aluminium Filtration by Al_2O_3 and SiC Ceramic Foam Filters. Light Metals 2013: 981–986
25. Syvertsen M, Bao S (2015) Performance Evaluation of Two Different Industrial Foam Filters with LiMCA II Data. Metall Mater Trans B 46:1058–1065
26. Khrustalyov AP, Kozulin AA, Zhukov IA, Khmeleva MG, Vorozhtsov AB, Eskin D, Chankitmunkong S, Platov VV., Vasilyev SV. (2019) Influence of Titanium Diboride Particle Size on Structure and Mechanical Properties of An Al-Mg Alloy. Metals (Basel). https://doi.org/10.3390/met9101030

ISBN 978-82-326-5934-0 (printed ver.)
ISBN 978-82-326-6022-3 (electronic ver.)
ISSN 1503-8181 (printed ver.)
ISSN 2703-8084 (online ver.)

NTNU
Norwegian University of
Science and Technology